Australian National University

LIGHT-MATTER INTERACTIONS IN TWO-DIMENSIONAL NANOMATERIAL PHOSPHORENE

By

Shuang Zhang

A thesis submitted for the degree of

Doctor of Philosophy

of The Australian National University

24th of August 2018

Declaration

I hereby declare that this thesis is based on work between July 2013 and August 2018 in the School of Engineering at the Australian National University, Canberra, Australia.

This thesis contains no material that has been previously accepted for the award of any other degree in any university, and contains no material previously published or written by another person, except where acknowledged and referenced in the customary manner.

_____ (Signed)

Shuang Zhang

August 2018

Dedication

To my family and my husband for their unconditional love and support

Acknowledgements

During my PhD study period, many people gave me support and I would like to give them my sincere gratitude at this moment. Firstly, I want to thank my supervisor Professor Qinghua Qin. Professor Qin is a perfect supervisor who is always there for students when we need him. He helped me a lot with my PhD application, supervised my research, and provided regular meetings and encouragement. Without his continuous support, I could not have finished my PhD. No words can express my appreciation to him.

I also want to express my gratitude to my supervisory panel. I thank Associate Professor Yuerui Lu who helped me a lot regarding experiments, data analysis and writing papers. I thank Dr. Adrian Lowe and Professor Roderick Boswell. They spared no effort in helping me when I needed their experimental equipment, giving me training and discussing experimental protocols.

Besides, I thank Dr. Yi Xiao for her generous help in research and life during the whole PhD study period, which was so important for me on this journey. Thanks to Dr. Fan Wang who helped me with micro-Raman/PL system debugging and MATLAB codes of the PL spectra correction, enabling us to analyse data more accurately and efficiently. Thanks to Dr Li Li and Dr Fouad Karouta for FIB/FEB and ANFF training and induction. Thanks to Professor Barry Luther-Davies for help with Raman/PL system enquiry. Thanks to Professor Vincent Craig and Associate Professor Jodie Bradby for AFM and nanoindentation training and help.

Additionally, I thank all my colleagues in the Biomaterials group, in particular Jin Tao, Haiyang Zhou, Cheuk Yu Lee, Bobin Xing and Song Chen. They give me generous support and advice in my research and daily life. It is a great honour for me to be their

colleague. I also express great gratitude to members of the NEMS group, in particular Jiong Yang, Jiajie Pei, Ye Win Myint, Yi Zhu, Ankur Sharma and Utkarshaa Varshney. I greatly appreciate their cooperation and help with experiments and data analysis. I also express great appreciation to Jiong Yang for his help in equipment training, as well as collaboration in experiments, data analysis and paper writing.

Furthermore, I thank my friends for their encouragement and support. Friends are like my family members who help me calm down when I get achievements and give me courage when I feel down. Much thanks to my best friends Shirley, Peng Liu, Li Liao, Haiyang Zhou, Xinwei Yang, Yuxing He, Yangyang Wu with whom I shared happiness and sorrow, from whom I learned to be more optimistic and enthusiastic. Besides, I also thank my friends in University House, in particular Julia Yang, Lisa Kao, Kaiyun Tsai, Fui Swen Kuh, QianYan Yap, Hongda Hao, Yan Zhang, Yi Zhou, Jing Cui and Xin Yu for their company and support.

Finally, I am grateful for the ANU PhD Scholarship and Tuition Fee Exemption Sponsorship scholarship, and to the ANU College of Engineering and Computer Science, ANU Research School of Physics and Engineering, ANFF ACT Node and EME facility.

Last but not the least, I give my sincere thanks to my family. I thank my parents, my husband's parents and my brother very much for their continuing support, encouragement and love. I thank my husband, Yanming Pei, with whom I am on the way to our dreams. He gives me countless support and inspiration, enabling me to overcome obstacles and difficulties and to remain full of hope.

Supervisory Panel

Prof. Qinghua Qin, The Australian National University, Primary Supervisor and Chair

Dr. Yuerui Lu, The Australian National University, Associate Supervisor

Dr. Adrian Lowe, The Australian National University, Associate Supervisor

Prof. Roderick Boswell, The Australian National University, Associate Supervisor

Abstract

Phosphorene is a new member of the family of two-dimensional (2D) materials. Compared with other 2D materials, phosphorene exhibits a layer-dependent direct bandgap in the range of mid-infrared to near-infrared wavelengths, which can bridge the gap between relatively large bandgap transition metal dichalcogenide semiconductors and gapless graphene. The predicable direct bandgap in few-layer phosphorene will facilitate the delivery of high-performance optoelectronic devices. Besides, the high surface-volume ratio in few-layer phosphorene enables strong light-matter interactions, making phosphorene very promising for applications in different optical components. In this work, the inelastic and elastic light-matter interactions in few-layer phosphorene were investigated.

For the study of inelastic light-matter interactions in phosphorene, photoluminescence (PL) and Raman effects were investigated to explore photon-electron and photon-phonon energy transfers respectively. Strong and highly layer-dependent PL was observed in few-layer phosphorene (2-5 layers). The results confirmed the theoretical prediction (by other researchers) that few-layer phosphorene had a direct and layer-sensitive bandgap. The work also demonstrated by Raman scattering that few-layer phosphorene was more sensitive to temperature modulation than graphene and MoS_2, which could be due to the superior mechanical flexibility of phosphorene originating from its unique puckered crystal structure. The anisotropic Raman response in few-layer phosphorene enabled the use of a pure optics method to quickly determine crystalline orientation without a tunnelling electron microscope or a scanning tunnelling microscope. The results obtained provided much-needed experimental information about the band structures and exciton

nature in few-layer phosphorene, paving the way for various optoelectronic and electronic applications.

Further study in terms of inelastic light-matter interaction was undertaken regarding PL emission from excitons and trions in few-layer phosphorene. Electrostatic modulation was applied to tune the density of trions. Thereby, a trion binding energy of 162 meV was found in few-layer phosphorene at room temperature. Such a large binding energy had previously only been observed in truly 1D materials such as carbon nanotubes, whose optoelectronic applications had been severely hindered by their intrinsically small optical cross-sections. Phosphorene offers an elegant way to overcome this hurdle by enabling quasi-1D excitonic and trionic behaviours in a large 2D area, allowing optoelectronic integration. Moreover, the quasi-1D nature of excitonic and trionic dynamics in phosphorene was validated experimentally and theoretically. The implications of the extraordinarily large trion binding energy in a higher-than-one-dimensional material are far-reaching.

In addition to inelastic light-matter interactions, elastic light-matter interactions in few-layer phosphorene were also studied by optical path length (OPL) and micro-lens. The giant OPL achieved in few-layer phosphorene was more than 20 times the physical thickness achieved in this few-layer phosphorene. Based on the layer-dependent OPL information, the number of layers could be more quickly and accurately identified compared with the conventional method for identifying number of layers. Black-phosphorus-based micro-lens optical properties were also studied to obtain information about elastic light-matter interactions in black phosphorus and its oxides.

CONTENTS

List of Tables

List of Figures

Acronyms

2D	Two-dimensional
AFM	Atomic force microscopy
CCD	Charge-coupled device
DFT	Density functional theory
EDX	Energy-dispersive X-ray spectroscopy
FIB	Focused ion beam
LD	Linear dichroism
MOS	Metal-oxide-semiconductor
OPL	Optical path length
PL	Photoluminescence
PSI	Phase-shifting interferometry
SEM	Scanning electron microscope
SOM	Scanning optical microscopy
STM	Scanning tunnelling microscope
TEM	Transmission electron microscopy
TMD	Transition metal dichalcogenide
TRPL	Time-resolved photoluminescence
VASP	Vienna ab initio simulation package

List of Notations

E Energy of a free electron

p Momentum

E_c Bottom of the conduction band energy

E_v Top of the valence band energy

E_g Width of the forbidden gap energy

m_n Effective mass

$F(E)$ Fermi-Dirac distribution (describes probability of an electron occupying an energy state E)

k Boltzmann constant

T Absolute temperature

E_F Energy of Fermi level

ω Mode frequency

ω_0 Mode frequency at zero K

χ First-order temperature coefficient

η_{PL} Luminescence quantum efficiency

I_{PL} PL intensity

k_{rad} Rates of radiative recombination within the conduction and valence bands

k_{defect} Rates of defect trapping within the conduction and valence bands

k_{relax} Rate of electron relaxation within the conduction and valence bands

n Hole doping density

C	Back-gate capacitance
V_g	Applied back-gate voltage
m_0	Mass of the free electron
$E_g(0)$	Ground-state transition energy at 0 K
S	Dimensionless coupling constant
ħω	average phonon energy
θ_1	Polarization angle of the incident light
θ_2	Polarization angle of the emission
E_E	binding energy of excitons
E_T	Binding energy of trions
D_E	Effective dimension of excitons
D_T	Effective dimension of trions
R_y^*	Effective Rydberg unit of energy
μ	Reduced mass
ε	Dielectric constant
D	Effective dimension
$a_r(x,y)$	Wavefront amplitude
$a_t(x,y)$	Wavefront amplitude
$\phi_r(x,y)$	Wavefront phase
$\phi_t(x,y)$	Wavefront phase
$\delta(t)$	Relative phase shift

λ Wavelength of the light source

ϕ_{BP} Measured phase shifts of the reflected light from the phosphorene flake

ϕ_{SiO_2} Measured phase shifts of the reflected light from the SiO_2 substrate

r_{ij} Reflection coefficients when the light travels from medium *i* to medium *j*

t_{ij} Transmission from medium *i* to medium *j*

n_i, n_j (*i*,*j* =1,2,3) Refractive index of medium *i*,*j*

k_0 Wave vector of incident light in air

$2k_0nd$ Round-trip propagation phase

n Refractive index

Chapter 1 Introduction

1.1 Research background

1.1.1 Two-dimensional nanomaterials and properties

Two-dimensional (2D) nanomaterials have a thickness range from one atomic to tens of nanometres, and 2D materials include multilayer, heterostructure and layer thin films [1]. Unlike conventional 2D metallic foils and thin films [2, 3], the term '2D materials' here implies that the thickness of the materials has orders of magnitude smaller than the wavelength of light involved [1].

Compared to conventional 3D semiconductors, 2D semiconductors exhibit many exceptional properties [1]: (1) many 2D materials interact strongly with light, even though they are very thin [4]; (2) 2D materials have novel optical and electronic properties that are distinctly different from those of their bulk forms [5-8], resulting from quantum confinement in the direction perpendicular to the 2D plane; (3) it is easy to integrate 2D materials with photonic structures such as waveguides [9-12] and cavities [13-17], owing to the naturally passivated surfaces in 2D materials. Moreover, it is possible to construct vertical heterostructures [18] by using different 2D materials without the conventional "lattice mismatch" issue, since layers with different lattice constants in heterostructures are only weakly bonded by van der Waals force, as in layered bulk materials; (4) 2D materials can cover a very wide range of the electromagnetic spectrum because of their diverse electronic properties, which enable them to be widely used in the area of optical and optoelectrics devices [1].

1.1.2 Conventional 2D semiconductor materials

Two-dimensional (2D) layered materials, including semi-metallic graphene [5, 6, 19-23],

semiconducting TMDs [8, 24-26] and insulating hexagonal boron nitride (hBN) [27, 28], have been heavily investigated in the past decade.

Graphene exhibits high mobility, optical transparency, flexibility and environmental stability, and is widely used in optical applications and optoelectronic devices. However, graphene has zero bandgap, which limits its application in the light-emitting area.

Compared with the gapless graphene, the most recently investigated TMD semiconductor MoS_2 has an energy gap in the range of 1.3 eV (bulk) to 1.8 eV (monolayer). MoS_2, an indirect bandgap material in its bulk form, becomes a direct bandgap semiconductor when thinned to a monolayer, enabling significantly enhanced photoluminescence (PL) in monolayer MoS_2 [7, 8, 29, 30].

Layered TMD semiconductors, such as MoS_2, $MoSe_2$ and WS_2, have attracted considerable attention owing to their exceptional properties, which include tightly bound excitons and trions and resulting large exciton and trion binding energies at elevated temperature [31, 32], strong Coulomb interactions arising from low dimensionality and reduced dielectric screening [33, 34], strong inelastic and elastic interactions with light [4, 35-37], a layer-dependent bandgap and indirect to direct bandgap transition with the number of layers reduced to one [8, 38-40], and so on.

1.1.3 Black phosphorus and phosphorene

Black phosphorus is an allotrope of the element phosphorus, like the other two allotropes (red phosphorus and white phosphorus). Black phosphorus has a higher density of 2.69 g/cm^3 compared to 1.83 g/cm^3 for white phosphorus and 2.05-2.34 g/cm^3 for red phosphorus [41]. Unlike red phosphorus and white phosphorus, black phosphorus cannot catch fire in air or be ignited by fire, and can sustain up to 400 ℃ in air without spontaneous ignition [42].

Black phosphorus was first synthesized in 1914 by Percy Williams Bridgman, during an attempt to force white phosphorus to change into red phosphorus by the application of high hydrostatic pressure, at a temperature below that at which the transformation runs with appreciable velocity at atmospheric pressure [42]. The white phosphorus (purest commercial stick phosphorus) was melted, solidified and then placed immediately under kerosene in a high-pressure cylinder. Pressure up to around 0.6GPa was applied to the phosphorus at room temperature; the cylinder's temperature was raised to 200℃ and its pressure was then raised to 1.2GPa~1.3GPa. It took about 5-30 minutes under this condition for the transition to occur from white phosphorus to black phosphorus. Finally, a small volume of black phosphorus transformed from white phosphorus was discovered after cooling the cylinder and relieving the pressure. Subsequently, black phosphorus was fabricated via a mercury or bismuth-flux method [43-45]. Silicon or germanium doped black phosphorus could also be achieved via the bismuth-flux method [46, 47].

In 1981, large single crystals of black phosphorus were successfully obtained from red phosphorus at high temperature under high pressure (3.8 GPa) by using a wedge-type cubic high-temperature (270℃) apparatus [48].

It was not until recently that black phosphorus was reported to be obtained under lower pressure [41]. Stefan Lange et al. [49] prepared black phosphorus by using a mineralizer (SnI_4) as promotor at non-toxic conditions in evacuated silica ampules. The raw materials (red phosphorus, gold, tin, and tin iodide) were heated to 600℃ and gradually cooled to room temperature, causing a reaction which usually took 5-10 days to complete [49, 50]. This process was further simplified by Köpf by using Sn/SnI_4 as the only mineralization additive [51].

Monolayer or few-layer black phosphorus is termed as phosphorene. Black phosphorus has a puckered structure, the crystal structure of few-layer phosphorene is shown in

Figure 1.1. The interlayer space between two neighbouring layers in black phosphorus is around 0.53nm [52]. The unit cell contains four atoms. Each phosphorus atom connects three neighbouring atoms at 2.18Å. As shown in Figure 1.1, phosphorene has a puckered anisotropic structure, which is different from graphene and TMD semiconductors. The anisotropic nature enables it to have anisotropic atomic vibration (to be shown in Chapter 3) and allows excitons to be confined in a quasi-1D space (as presented in Chapter 4).

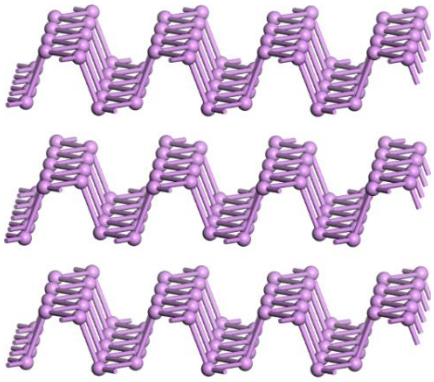

Figure 1.1 **Schematic plot of phosphorene layer structure**

Phosphorene has become a new class of 2D layered material, with a predicted layer-dependent bandgap ranging from 0.3 eV (bulk) to 1.5 eV (monolayer) [53-58]. In particular, few-layer phosphorene with narrow bandgaps ranging from mid-infrared to near-infrared wavelengths can fill the space between gapless graphene and comparably large gap TMD semiconductors [58-60]. Besides, the predicted nature of the direct bandgap in few-layer phosphorene should also be more applicable for high-performance optoelectronic devices compared with the indirect bandgap behaviour in most few-layer TMD semiconductors. However, until May 2014 there was very little experimental data to confirm the theoretical predictions for few-layer phosphorene.

1.1.4 Light-matter interactions

Owing to the significantly increased surface-volume ratio in thin-layer 2D materials, their light-matter interactions become remarkably strong [61]. There are two types of interaction between light and matter [62]: inelastic and elastic. An inelastic interaction involves energy transfer. Elastic interaction does not involve energy transfer and is responsible for controlling the propagation of light.

Inelastic light-matter interactions involve in energy transfer between photons-electrons or photons-phonons, leading to the PL or Raman effects, respectively [61]. Optical devices such as transistors, LEDs and solar cells are based on their inelastic interactions. In the process of inelastic light-matter interaction, the electronic band structure of a semiconductor material plays a key role. Therefore, band structure investigation and modulation are of great importance in the design of optical devices. In 2D materials, the band structures are more sensitive to the external environment due to the significantly increased surface to volume ratio compared with the sensitivity in their bulk form; therefore the materials can be more easily controlled by the corresponding techniques [63-65] (e.g., van der Waals interactions, temperature, electric field, etc.). In this thesis, band structure and band structure modulation are studied and discussed in Chapters 3 and 4.

Elastic light-matter interactions do not involve energy transfer. Optical components such as lenses, gratings, waveguides and optical meta-materials [66] depend on elastic light-matter interactions to achieve sophisticated control of light [61]. Strong elastic interactions rely on significant changes in the amplitude and phase of light accumulated over a long optical path. In few-layer 2D materials such as monolayer graphene, the interaction is normally very small [67]. It is quite challenging to control the propagation of light using a 2D material in the visible and near-infrared regions where most interesting

optoelectronic properties exist. Surprisingly, the strength of the elastic interaction increases dramatically with the increase in the refractive index. Such favourable scaling makes high-index 2D TMD semiconductors [26, 68] particularly attractive for the application of elastic light-matter interactions. In this thesis, elastic light-matter interactions are discussed in Chapter 5.

1.1.5 Literature review summary

Bulk black phosphorus was first fabricated around a century ago [42]. During the past century, the synthesis, physical properties and application of bulk black phosphorus was extensively studied [41]. These studies were focused on the bulk form, but the exfoliated, two-dimensional form was also predicted to endow black phosphorus with new life and properties [69]. In 2014, Li et al. [60] experimentally fabricated a field-effect transistor based on thin-layer black phosphorus only a few nanometres in thickness, bringing black phosphorus back into the spotlight and arousing a renaissance of interest in this material [41, 53, 59].

Light-matter interactions are the fundamental mechanisms of various optical devices and optoelectronic devices. 2D materials have strong inelastic and elastic interactions with light, due to band nesting that is enhanced by the presence of van Hove singularities in the band structure in these materials [4, 70, 71]. The strong light-matter interactions in 2D materials have attracted considerable research attention.

For inelastic light-matter interactions, Raman effect and PL phenomenon are common methods used to characterize photon-phonon and photon-electrons energy transfer respectively. The Raman effect is affected by the crystal lattice structures of the material and can be used to characterize the quality or status of the crystal, whereas the PL phenomenon is highly dependent on the bandgap of a semiconductor, which is the basis for the development of novel optical devices [61]. It is vital, therefore, to investigate the

electronic band structure and its modulations in a semiconductor material, another area which has attracted great attention. He et al. explored exciton and trion states of monolayer MoS_2 and reported that exciton and trion dynamics can be tuned up to two orders of magnitude by an electric field at room temperature [32, 72], due to the nature of the direct bandgap. In contrast, the excitons and trions in bi-layer MoS_2 cannot be tuned by an electric field at room temperature because of the indirect bandgap [73], but they can be tuned via the co-modulation of electric field and low temperature [39]. Similar studies were also conducted on $MoSe_2$ [74] in order to understand its band structure. In addition to investigations of the PL emission of the excitons and trions, much work has also focused on PL emission from biexcitons [61] and localized exciton (defects) [75-78] since they also have a marked influence on the optical properties of 2D materials. These studies have not only helped to increase understanding of inelastic light-matter interactions, but also have provided opportunities to develop novel optical devices. The new 2D material phosphorene was predicted to have a direct bandgap which would also enable the development of high-performance light-emitting devices, compared with the indirect bandgap behaviour in most few-layer TMD semiconductors. However, until 2014 very little experimental data was available to confirm the theoretical prediction of few-layer phosphorene. Therefore, the study of inelastic light-matter interactions in few-layer phosphorene is of great importance.

For characterization of elastic light-matter interactions, phase shift is an effective method which measures the light propagation in the material. Using a phase shift interferometer, Venkatachalam et al. measured the phase shift of thin-layer graphene and obtained information about optical thickness down to monolayer level [79]. This method was also used to measure the optical thickness of WS_2, WSe_2 and MoS_2. Very high OPL values [80] were observed from these three 2D materials. The OPL in these materials implied that they could control the phase front efficiently even in atomically thin structures [61].

Given such excellent property in controlling phase front, ultrathin micro-lenses were fabricated based on different materials such as MoS_2 [80], organic materials CHQ [81], graphene oxide [82], etc. In the present project, the OPL of phosphorene was studied to gain information about the elastic light-matter interactions in phosphorene. Then, based on the light-propagation property of phosphorene, micro-lenses were fabricated.

1.2 Black phosphorus light-matter interaction research targets

1.2.1 Main research targets

This work involved elastic and inelastic light-matter interactions in phosphorene. The research targets were as follows:

1) For inelastic light-matter interactions, the bandgap structure of materials plays a key role in inelastic light-matter interactions and the predicted direct bandgap nature of few-layer phosphorene enables high-performance optoelectronic devices to be created, compared with the indirect bandgap behaviour in most few-layer TMD semiconductors. However, very little experimental data was reported to confirm the theoretical predictions for few-layer phosphorene until 2014. Therefore, investigation of the nature of the bandgap in phosphorene was the first target.
2) The band structure was very sensitive and could be controlled by certain external techniques (e.g., temperature, electric field, surface defects etc.), due to the large surface-volume ratio in phosphorene. For this target, four aspects were involved: study in few-layer phosphorene of its anisotropic nature, layer-dependent bandgap energy, excitons-trions transformation dynamics and trion binding energy.
3) The photon-phonon energy transfer (inelastic interactions) provides information about crystal lattice structures and can be used to characterize the quality or status of the crystal, the thermal conductivity, etc. For this target, three main aspects were involved: first, Raman effects of few-layer phosphorene were investigated to obtain

crystal lattice information; secondly, temperature-dependent Raman measurements were conducted to study the thermal properties of few-layer phosphorene; thirdly, polarization-dependent Raman effects were explored to obtain information about the anisotropic nature of few-layer phosphorene.

4) Additionally, elastic light-matter interactions were also studied. In terms of inelastic research, there were two main studies: optical path length (OPL) and phosphorene-based devices.

1.2.2 The technical path of research targets

In this work, few-layer phosphorene was fabricated via the method of mechanical exfoliation from bulk black phosphorus single crystals (from Smart-elements) using GEL film (Gel-Pak), and then transferred onto Si/SiO_2 (275nm thermal SiO_2) substrate. Optical microscope and atomic force microscopy (AFM) measurements were applied to identify phosphorene flakes and to obtain physical thickness information respectively, in order to obtain information about the number of layers of the black phosphorus flakes.

For the study of inelastic light-matter interactions in phosphorene, PL and Raman effects were investigated to explore the energy transfer of photon-electrons and photon-phonon respectively. For the study of external technique-affected band structure, low-temperature stage, polarizer and back-gate voltage were added to the Raman/PL system for band structure modulation. Further study in terms of inelastic light-matter interaction focused on multi-body interactions in few-layer phosphorene, in which electron states were modulated by back-gate voltage.

For the study of elastic light-matter interaction in phosphorene, phase-shifting interferometry (PSI) was applied to obtain information about OPL. For the thin-layer-based micro-lens, a focused ion beam (FIB) was used for micro-lens milling and scanning optical microscopy (SOM) was applied for optical focal length measurement.

1.2.3 Technical problems and solutions in this work

During the experimental processes, the degradation of few-layer phosphorene samples (reacting with oxygen and water) became a major concern. It was very difficult to achieve satisfactorily stable experimental results from these degraded samples. To solve this problem, the mechanism of this degradation was studied, and some solutions were proposed for different stages of this work.

First, the black phosphorus crystal was wrapped in aluminium foil and kept in a vacuum chamber at around 1000 Pa to effectively decrease the contact with light and oxygen.

Secondly, the few-layer black phosphorous fabrication time was minimized by identifying the number of layers roughly via colour contrast in the optical microscope and then the few-layer black phosphorous samples were drily transferred to substrate.

Thirdly, for the first time, PSI was applied to measure the optical path length of phosphorene. Based on the measurements of physical thickness and related OPL from tens of few-layer phosphorene samples, the linear relationship between OPL and number of layers of the phosphorene was determined. For the physical thickness of monolayer phosphorene was below 1nm (via AFM), while its OPL was around 20nm (instrumental error from PSI is around 2nm), which made it highly accurate in obtaining information about the number of layers. Moreover, measurement by PSI took only around 5 minutes. Further, PSI was used to investigate the surface topography based on analysing the digitized interference data obtained during a well-controlled phase shift introduced by a Mirau interferometer [83]. Therefore, the number of phosphorene layers was quickly and accurately measured, effectively decreasing the degradation.

Fourthly, the sample was quickly put into a microscope-compatible chamber with a slow flow of nitrogen protective gas, to slow the reaction of phosphorene with moisture and other possible reactants from the environment. The sample exposure time in air for optical

microscope imaging was minimized to be less than around 15 minutes. All PL, Raman and polarization measurements were conducted with a T64000 micro-Raman system equipped with both CCD and InGaAs detectors. For low-temperature Raman measurements, a Linkam THMS 600 liquid nitrogen low-temperature stage was added to the micro-Raman system. During the measurements, the laser power was kept as low as ~20 μ w.

Fifthly, for the study of the dynamics of excitons and trions transformation, back-gate voltage was applied to inject more holes/electrons into the system. In addition, for the fabrication of a few-layer phosphorene metal-oxide-semiconductor (MOS) device, Au electrodes were pre-patterned and graphene flakes were transferred onto the MOS device to quickly bridge the few-layer phosphorene samples and electrodes. The conventional method for bridging samples and electrodes is by patterning another electrode via a FIB, which is very accurate and simple. However, the conventional method is not suitable for a phosphorene MOS device since few-layer phosphorene can degrade in the process of FIB (normally, use of the FIB equipment must be booked in advance and take at least one hour). While by bridging a phosphorene sample and electrode with graphene, the MOS device was fabricated within only 30 minutes, and then the MOS device was loaded in a Linkam THMS 600 liquid nitrogen low-temperature stage for further gate-dependence measurements.

1.3 Organization of the thesis

The thesis consists of six chapters: In Chapter 1, the research background is described. In Chapter 2, experimental methods are described, and the theories used in the work are reviewed. In Chapter 3, few-layer phosphorene characterization, PL phenomenon and Raman shift information are presented. In Chapter 4, exciton and trion dynamics are described and extraordinary quasi-one-dimensional trions are analysed. Exciton and trion

dynamics of 1L $MoS_{2x}Se_{2(1-x)}$ (x=0.45) are also studied for comparison. In Chapter 5, the OPL of thin-layer phosphorene is investigated, few-layer phosphorene-based micro-lens and properties are presented and explained. In Chapter 6, the conclusion of this thesis is presented, and possible future work is suggested.

Chapter 2 Experiments and theory

This chapter describes the experimental methods and some fundamental theory employed in this work.

The first part of this chapter details the experimental methods used in the work. Figure 2.1 shows the content for "light-matter interactions in phosphorene" and the main characterization methods. These characterization methods are introduced in Chapter 2.1.

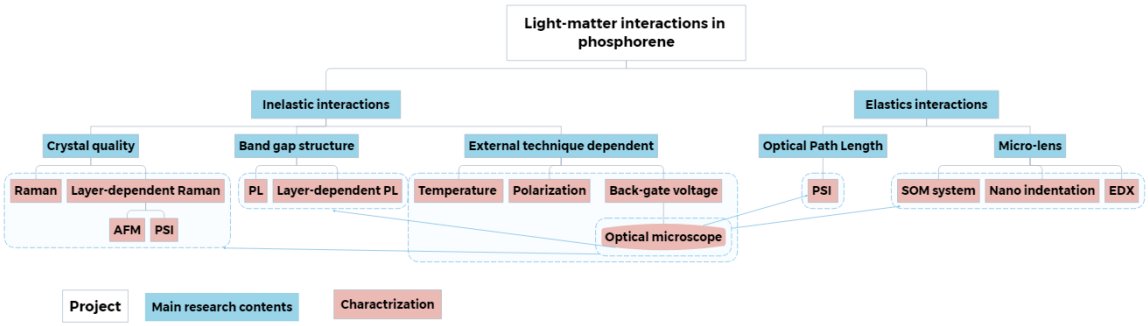

Figure 2.1 **Contents for "light-matter interactions in phosphorene" and relevant characterization methods**

The second part of the chapter presents the fundamental theory used in the experiments, analysis and calculation, which are shown in Sections 2.2, 2.3 and 2.4.

2.1 Experimental procedure

2.1.1 Fabrication of few-layer black phosphorus

Bulk black phosphorus single crystal was purchased from Smart-elements. GEL film (Gel-Pak) was used for mechanical exfoliation of thin-layer phosphorene, providing a much higher yield than that from scotch tape only. The thin-layer phosphorene was then drily transferred onto a SiO_2/Si substrate (275 nm thermal SiO_2).

2.1.2 Optical microscopy

Few-layer phosphorene flakes were quickly identified by optical contrast under an optical microscope. The optical microscope detector used green channel (495-530nm) of a colour camera. The atomic layer material could even be visualized via optical microscope because the material exhibited large contrast value [84-86] when it was prepared on top of silicon wafers with a certain thickness of SiO_2.

2.1.3 Phase-shifting interferometry (PSI) measurements

PSI was used to measure the OPL of phosphorene, yielding information about the elastic light-matter interactions in phosphorene. The number of layers of the phosphorene could be quickly and accurately measured via PSI, effectively eliminating any degradation problem.

PSI was used to investigate the surface topography by analysing the digitized interference data obtained during a well-controlled phase shift introduced by the Mirau interferometer [83]. The PSI system (Vecco NT9100) used in the experiments operated with a green LED source centred near 535 nm by a 10 nm band-pass filter [79]

2.1.4 Raman/PL measurements

The sample was quickly put into a microscope-compatible chamber with a slow flow of nitrogen protection gas, to slow the reaction of phosphorene with moisture and other possible reactants from the environment. The sample exposure time in air for optical microscope imaging was minimized to be less than around 15 minutes.

All PL, Raman and polarization measurements were conducted using a T64000 micro-Raman system equipped with both CCD and InGaAs detectors.

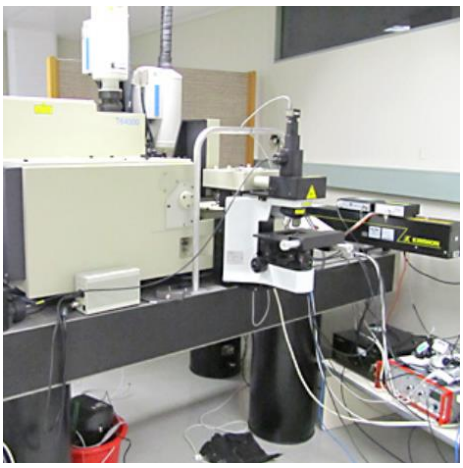

Figure 2. 2 **Micro-raman/micro-photoluminescence system**

2.1.5 Atomic force microscopy (AFM)

AFM was used to obtain physical thickness information about phosphorene flakes. Normally, physical thickness measurement by AFM would take around 20 minutes.

After the PL or Raman characterizations, quick AFM scanning was conducted to confirm the number of layers of the phosphorene flake, performed in the ambient atmosphere at room temperature using a Bruker MultiMode III AFM tapping mode.

Figure 2. 3 **Bruker Multimode VIII**

2.1.6 Polarization measurement

For polarization-dependent Raman measurements, an angle-variable polaroid was inserted into the optical path of the micro-Raman system. The polaroid was shifted 6 degrees repeatedly 30 times to obtain a full period of polarization results. To avoid laser-induced sample damage during polarization-dependent measurements, all Raman and PL spectra were recorded at low power levels P of ~100 μW. Raman measurements used short integration times of ~10 s and PL used longer integration times of ~60 s. The nitrogen chamber and low-power laser effectively protected the sample.

2.1.7 Low-temperature measurement

For low-temperature Raman/PL measurements, a Linkam THMS 600 liquid N_2 low-temperature stage was added onto the micro-Raman/PL system. This low-temperature stage was related to a compatible chamber. The sample was loaded in the chamber with a slow flow of nitrogen protection gas, to slow the reaction of phosphorene with moisture and other possible reactants from the environment.

2.1.8 Gate-dependence measurement

Phosphorene flakes were fabricated by the mechanical exfoliation method and then drily transferred [87] onto a SiO_2/Si substrate (275 nm thermal oxide on n^+-doped silicon)，near a pre-patterned gold electrode. The gold electrodes were patterned by conventional photolithography, metal deposition and lift-off processes. Another thick graphite flake was similarly transferred to electrically bridge the phosphorene flake and the gold electrode, forming a MOS device. During the measurements, the gold electrode was grounded, and the n^+-doped Si substrate functioned as a back gate, providing uniform electrostatic doping in the phosphorene.

All PL and polarization measurements were conducted using a T64000 micro-Raman system equipped with a charge-coupled device (CCD) and InGaAs detectors, along with a 532nm Nd:YAG laser as the excitation source. For all measurements, the sample was placed into a microscope-compatible chamber with a slow flow of protective nitrogen gas to prevent degradation of the sample. To avoid laser-induced sample damage during gate-dependence measurements, all PL spectra were recorded at low power levels: P ~20 μW. For the PL measurements, an integration time of 30 s was used. The electrical bias was applied using a Keithley 4200 semiconductor analyser.

2.1.9 Focused ion/electron beam (FIB/FEB)

The micro-lens was fabricated via a FEI Helios 600 NanoLab Focused Ion Beam (dual-beam) and a scanning electron microscope (SEM) system. The SEM in this system enabled high resolution for nanoscale imaging owing to the small diffraction limit of an electron wave. During the micro-lens fabrication process, a gallium ion source was applied with a pre-calibrated dosage, an optimized voltage of 30kV and a beam current of 9.7pA. After the ion milling process it was possible instantly to check the patterns by a high-resolution SEM. This system could reach a resolution below 20nm in the lateral direction in ion milling and atomic resolution in the vertical direction.

2.1.10 Micro-lens characterization methods

The micro-lens was characterized by a far-field scanning optical microscopy (SOM) system that was built on the base of the micro-Raman/PL system. For the SOM system, a green laser at 532nm was applied and focused on the focal plane of an Olympus 50X object lens (NA=0.25, depth of focus 10μm). The micro-lens was moved along the z axis at a step of 10μm by a piezo-electrical driven stage. A camera was used to record the laser intensity distribution when the phosphorene-based micro-lens was moved at different z

values. After the measurements, a three-dimensional laser light distribution dataset was built.

For power-dependent micro-lens measurement, a neutral-density filter was applied to tune the insert laser power continuously; for gate-dependence measurement, a Keithley 4200 semiconductor analyser was used. Nanoindentation was also used to characterize the mechanical properties of the micro-lens. As well, energy-dispersive X-ray spectroscopy (EDX) and SEM measurements were conducted to characterize the chemical composition and distribution of the micro-lens.

2.1.11 Nanoindentation measurement

The mechanical properties of the phosphorene-based micro-lens was characterized by a TriboIndenter TI 900 Low-Load nanoindentation system. That instrument consists mainly of three components: a hemispherical head indenter, an optical microscope and an X-Y stage which can move the specimen between microscope and hemispherical head indenter. The whole device was located on an anti-vibration table to exclude transmissions from building vibrations.

At the beginning of measurements, indentation positions were individually selected by a remote video-controlled microscope, and the X-Y coordinates of these positions were then stored in a computer. Under the control of the computer, the specimen was transferred to the indenter position. After that, accurate calibration of the distance between microscope and indenter was conducted to ensure precise motion of pre-programmed positions of the indenter.

During measurements, a small load from 0μN to 100μN was applied to the indenter (4 indentations) and then unloading from 100μN to 0μN was applied. Similarly, the load-strain depth and unloading-strain depth of 500μN (7 indentations) and 1000μN (2 indentations) were also characterized respectively. After the measurements, the reduced

modulus was determined by fitting the load-displacement curve and applying it to dynamic mechanical analysis.

2.2 Physical theory

Theoretical and numerical approaches [88-98] are powerful for analysing engineering problems such as material performance and function identification. In this section, the foundations of physical theories about Raman spectra, photoluminescence, bandgap energy and Fermi distribution are discussed.

2.2.1 Raman spectra[99]

Although most of light travelling through a medium is either transmitted or absorbed following the standard laws of reflection and refraction, a very tiny fraction of light is scattered in all directions by inhomogeneities within the medium [99]. There are several types of inhomogeneity: static scattering, dynamic scattering and other types. Defects such as dislocations in crystals are static scatters which scatter light elastically (i.e., without frequency change). Fluctuations in the density of the medium associated with vibration are examples of dynamic scatters. Other scatter mechanism types in semiconductors are fluctuations in charge or spin density. Inelastic scattering of light by molecular vibrations was first reported by Raman [100], who was awarded Nobel prize in 1930 for his discovery of Raman scattering. Now Raman spectroscopy has become a spectroscopic technique used to observe vibrational, rotational, and other low-frequency modes in a system [101].

The normal modes of atomic vibration are quantized into phonons. Since the phonon frequency is equal to the difference between the incident photon frequency and the scattering photon frequency, the difference is referred to as Raman frequency (or Raman

shift) [99]. A Raman spectrum is often plotted as the intensity of scattering light versus Raman frequency.

2.2.2 Photoluminescence[99]

For a sample to emit radiation, it must be energized by external means such as external current, heat or photons. If excitation of a sample is by absorption of photons of the energy higher than bandgap energy, the resulting process, in which photons with lower energy than the exciting photons are radiated, is known as photoluminescence [99].

In the absorption process of photoluminescence, energy is transferred from external photons to materials, and electrons and holes would be created in the conduction band and valence band, respectively. Then the excitations undergo energy and momentum change towards the minimum of the conduction band. Finally, the excitations and holes recombine with the emission of photons. PL provides information about the light emission.

2.2.3 Band structure [102]

(1) Bandgap energy

At absolute zero temperature, electrons occupy the lowest energy states, so that all states in the lower band (the valence band) will be full, while the states in the upper band (the conduction band) will be empty. The bottom of the conduction band is called E_c and the top of the valence band is called E_v. As shown on the left of Figure 2.4, the bandgap energy E_g is the width of the forbidden gap energy, which is between the bottom of conduction band and the top of the valence band (E_c-E_v). Physically, the bandgap energy E_g is the energy required to break a bond in a semiconductor to free an electron to the conduction band and leave a hole in the valence band [102].

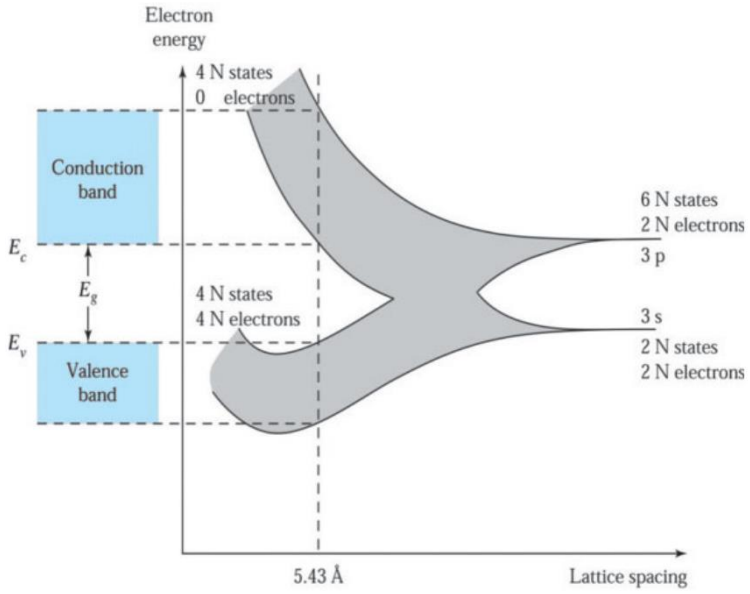

Figure 2.4 **Formation of energy bands as a diamond lattice crystal is formed by bringing isolated silicon atoms together** [102].

(2) Energy-momentum relationship

The energy E of a free electron is given by

$$E = \frac{p^2}{2m_0} \tag{2.1}$$

where p is the momentum and m_0 is the free-electron mass. This equation is valid when an electron in a conduction band is similar to a free electron in being relatively free to move about in a semiconductor crystal. However, since there is periodic potential of nuclei, Equation 2.1 is not valid. However, if we replace m_0 by an effective mass m_n (the subscript n here implies negative charge on an electron), that is

$$E = \frac{p^2}{2m_n} \tag{2.2}$$

and the effective mass m_n depends on the properties of the semiconductor material. A similar expression can be written for holes (with effective mass m_p referring to a positive

m_n charge on a hole). Note that the electron's energy is measured upward whereas the hole's energy is measured downward.

The actual semiconductor energy-momentum relationships (also called the energy-band diagram) are very complex. Since the periodicity of most lattices is different in various directions, the E-p diagram (Figure 2.5) also differs in different directions. If E_c is located at p=0, it means that the effective mass of electrons in different directions is the same; if E_c occurs at p≠0, it means that the electrons' behaviour in every direction is not the same in this material.

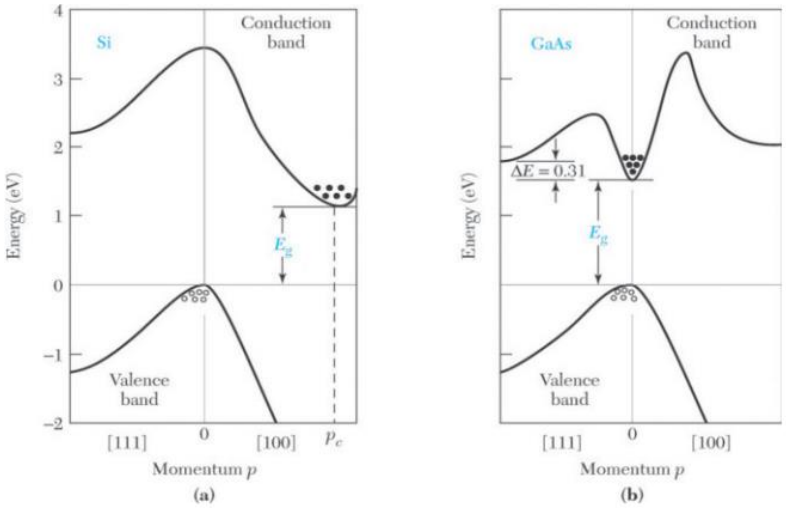

Figure 2.5 **Energy band structures of (a) Si and (b) GaAs.** Circles (o) indicate holes in the valence band and dots (.) indicate electrons in the conduction band[102]

Take silicon and gallium arsenide as examples (Figure 2.5). For silicon, the maximum in valence occurs at p=0 while the minimum in the conduction band occurs at p=p_c. Therefore, when an electron transits from the top of the valence band to the bottom of conduction band, not only energy ($\geqslant E_g$) but also a momentum change ($\geqslant p_c$) is needed. Silicon is called an indirect semiconductor since a momentum change is required for electron transition.

For gallium arsenide, the maximum of the valence band and the minimum of the conduction band occur at the same momentum (p=0), so no momentum change is required when an electron makes a transition. Therefore, gallium arsenide is called a direct semiconductor because it does not need a momentum change for electron transition.

The difference between an indirect semiconductor and a direct semiconductor is very important for light-emitting diodes and lasers, since these devices require a direct semiconductor to generate photons with high efficiency. In this work, few-layer phosphorene and monolayer $MoS_{2x}Se_{2(1-x)}$ (x=0.45) have direct bandgaps, whereas silicon has an indirect bandgap (see Chapters 3 and 4).

(3) Conduction in conductor, semiconductor and insulator

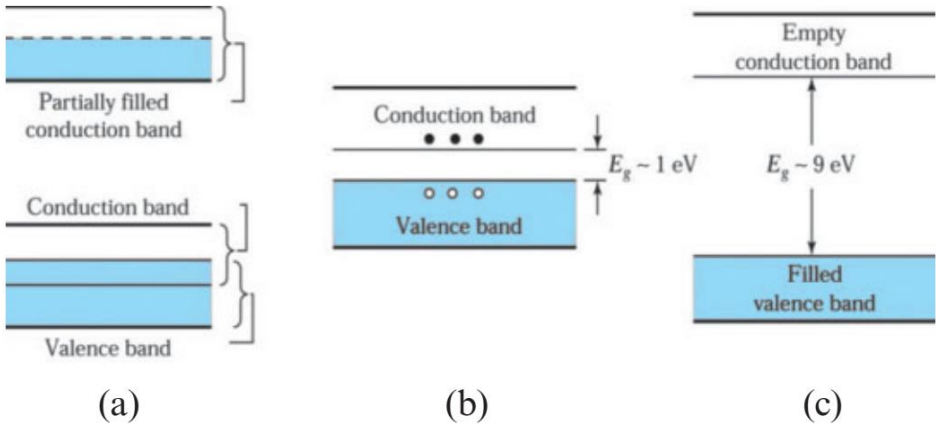

Figure 2.6 **Schematic energy band representations** of **(a)** a conductor with two possibilities (either the partially filled conduction band shown at the upper portion or the overlapping bands shown at the lower portion), **(b)** a semiconductor, and **(c)** an insulator [102].

The variation in the energy band diagrams for metals, semiconductors and insulators can be seen in Figure 2.6. From the diagram, it is very clear that there is no bandgap in metals. Consequently, the uppermost electrons or electrons at the top of the valence band can easily move to the upper level when kinetic energy is provided (e.g., from an applied electric field). Therefore, current conduction can readily occur for metals. For insulators,

all energy levels in the valence band are occupied by electrons and all energy levels in conduction bands are empty. Thermal energy (at room temperature, kT is 0.026eV, and this is much smaller than the insulator bandgap energy) or energy from an electric field is insufficient to raise the uppermost electrons to the conduction band. Therefore, an insulator cannot conduct current.

Consider a material with an energy gap of around 1ev, called a semiconductor. At T=0K, all electrons are in the valence band and no electrons are in the conduction band, indicating that semiconductors are poor conductors at low temperature. At room temperature and under normal atmosphere, the thermal energy kT is a good fraction of E_g (E_g is 1.12 eV for silicon and 1.42 eV for GaAs). Therefore, an appreciable number of electrons are thermally excited from the valence band to the conduction band. Since there are many empty states in the conduction band, a small applied potential can easily move electrons, leading to a moderate current.

2.2.4 Fermi level

Fermi level is the energy at which the probability of occupying an energy state is exactly one-half. The probability of an electron occupying an energy state E can be described by the Fermi-Dirac distribution (also called the Fermi distribution) function as:

$$F(E) = \frac{1}{1+e^{(E-E_F)/KT}}, \tag{2.3}$$

where k is a Boltzmann constant, T is the absolute temperature and E_F is the energy of the Fermi level.

2.3 Exciton states

2.3.1 Exciton and trion

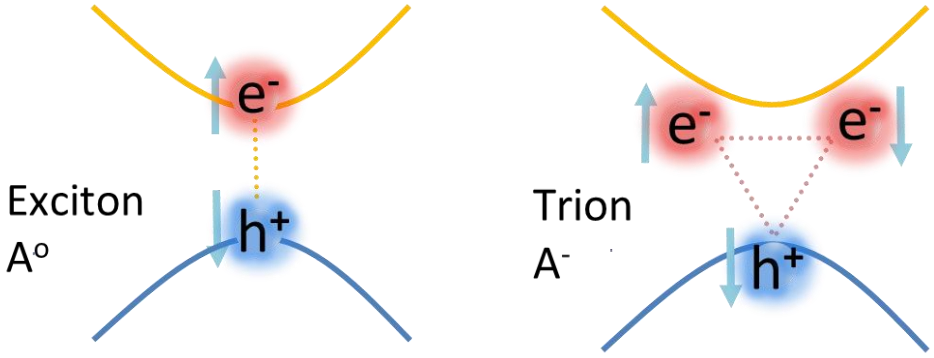

Figure 2.7 **Schematic diagram of neutral exciton and negative trion**

As is shown in Figure 2.7, a neutral exciton is a bound quasi-particle state between one electron and one hole through a Coulomb interaction, like a neutral hydrogen atom. A trion is a charged exciton composed of two electrons and one hole (or two holes and one electron), analogous to H^- (or H_2^+) [103].

2.3.2 Trion binding energy

The schematic diagram of an energy bandgap is presented in Figure 2.8. Trion binding energy (E_{b_trion}) is the energy required to break the trion bindings and form excitons. Therefore, trion binding energy is the energy difference between exciton band energy and trion energy. In contrast to the exciton, a trion has an extra charge with nonzero spin, which can be used for spin manipulation. More importantly, the density of trions can be electrically tuned by the gate voltage, enabling remarkable optoelectronic applications. For these purposes, a large trion binding energy is critical to overcome room-temperature thermal fluctuations as well as to widen the spectral tuning range.

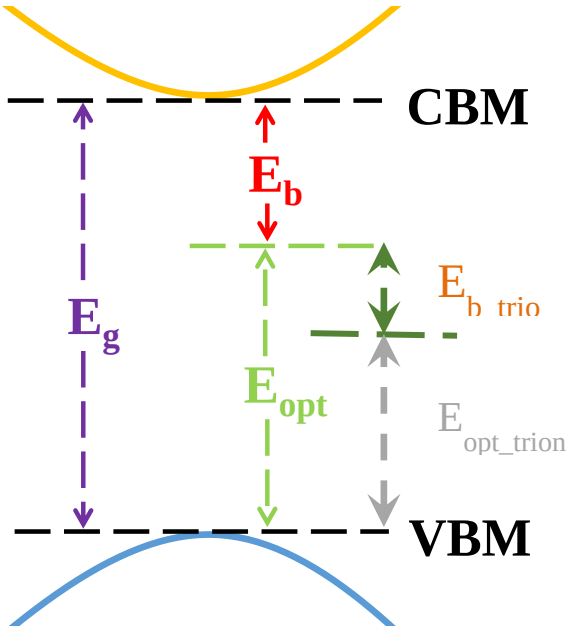

Figure 2.8 **Schematic diagram of energy bandgap**

Chapter 3 Inelastic light-matter interactions

In this chapter, Raman effects and the PL phenomenon are discussed in investigation of inelastic light-matter interactions in few-layer phosphorene.

Few-layer phosphorene was measured using Raman and investigated the photon-phonon energy transfer and crystal vibration, and temperature-dependent Raman effects were studied to obtain information about the thermal properties of phosphorene. Polarization-dependent Raman measurements were conducted to study the strong anisotropic nature of few-layer phosphorene, allowing for rapid determination of its crystalline orientation by Raman microscopy, without the need for complex high-resolution imaging systems such as STM or TEM.

For the PL research, layer-dependent PL was studied to explore the bandgap energy of phosphorene, and layer-dependent bandgap energy was also simulated as a comparison. Internal luminescence quantum efficiency was also studied to investigate the layer-dependent band structure.

3.1 Raman spectra in few-layer phosphorene

3.1.1 Raman spectra

The optical properties of few-layer phosphorene were investigated by micro-Raman spectroscopy. All the Raman measurements were carried out in a confocal microscopy setup with a 532nm solid state green laser for excitation and a spatial resolution of sub-1 μm. All the Raman spectra were measured using the CCD detector. To prevent the few-layer phosphorene reacting with moisture or other possible reactants from the environment, the samples were placed in a microscope-compatible chamber with a slow flow of nitrogen gas.

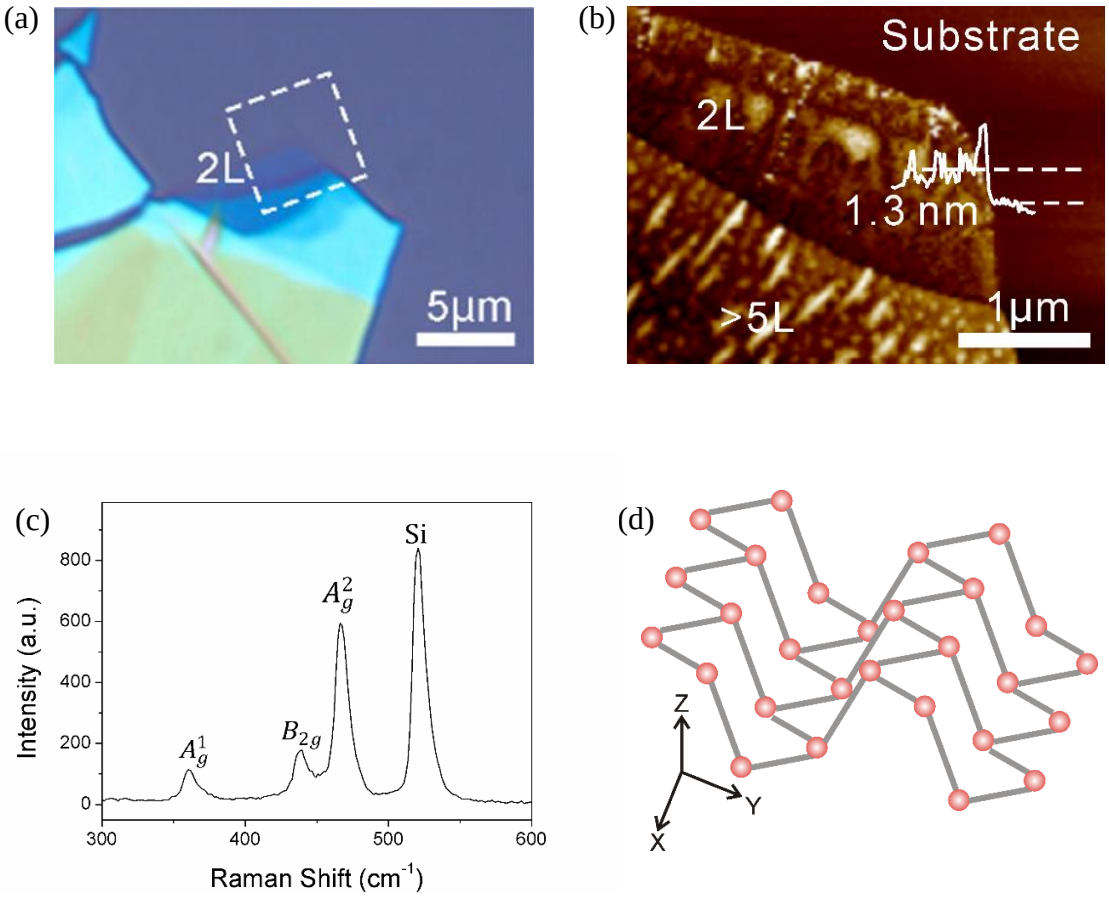

Figure 3.1 **Images and characterization of exfoliated phosphorene. (a)** Optical microscope image of 2L phosphorene, taken by Leica microscope. **(b)** AFM image of 2L phosphorene, with region indicated in the dashed line box in (a). **(c)** Raman spectrum of 2L phosphorene. **(d)** Schematic plot of phosphorene layer structure.

The measured Raman peaks (Figure 3.1), at 359 cm^{-1}, 437 cm^{-1} and 466 cm^{-1}, were attributed to the A_g^1, B_{2g} and A_g^2 phonon modes in the crystalline few-layer phosphorene flakes, which matched well with observations in bulk black phosphorus [104].

3.1.2 Polarization-dependent Raman spectra

Compared with other 2D materials, phosphorene shows strong anisotropic properties [53, 105], allowing various unique applications in optoelectronics. Normally, TEM is used to analyse the crystalline orientation of crystals. But the high-energy electrons in TEM were

likely to introduce multiple defects in phosphorene which could expedite the reaction of phosphorene with moisture and other possible reactants from the environment [106]. Thus, it was important to develop optical means to characterize the crystalline properties. It has been recently shown that second-harmonic generation could be used to determine the crystalline orientation of MoS_2 [107]. Here, an even simpler optical means of determining the crystalline orientation of phosphorene was developed. This process was critically important as it caused minimal damage to phosphorene and significantly shortened the time of characterization, allowing more accurate analysis of the intrinsic phosphorene properties. The simpler optical means was based on the anisotropic nature in phosphorene.

Linearly polarized Raman measurements were performed to quickly determine the crystalline orientation of a phosphorene flake (15L) (Figure 3.2). The normally incident laser was in the z direction. The polarization angle θ is relative to the zero-degree reference, which could be arbitrarily selected at the beginning. As evident in Figure 3.2a, the Raman intensities of B_{2g} and A_g^2 modes are significantly dependent on the polarization angle. The angle-dependent intensities of B_{2g} and A_g^2 modes both show an angle period of 180^o and are out-of-phase (Figure 3.2b). The Raman intensity of A_g^1 is less sensitive to the polarization angle (Figure 3.2b).

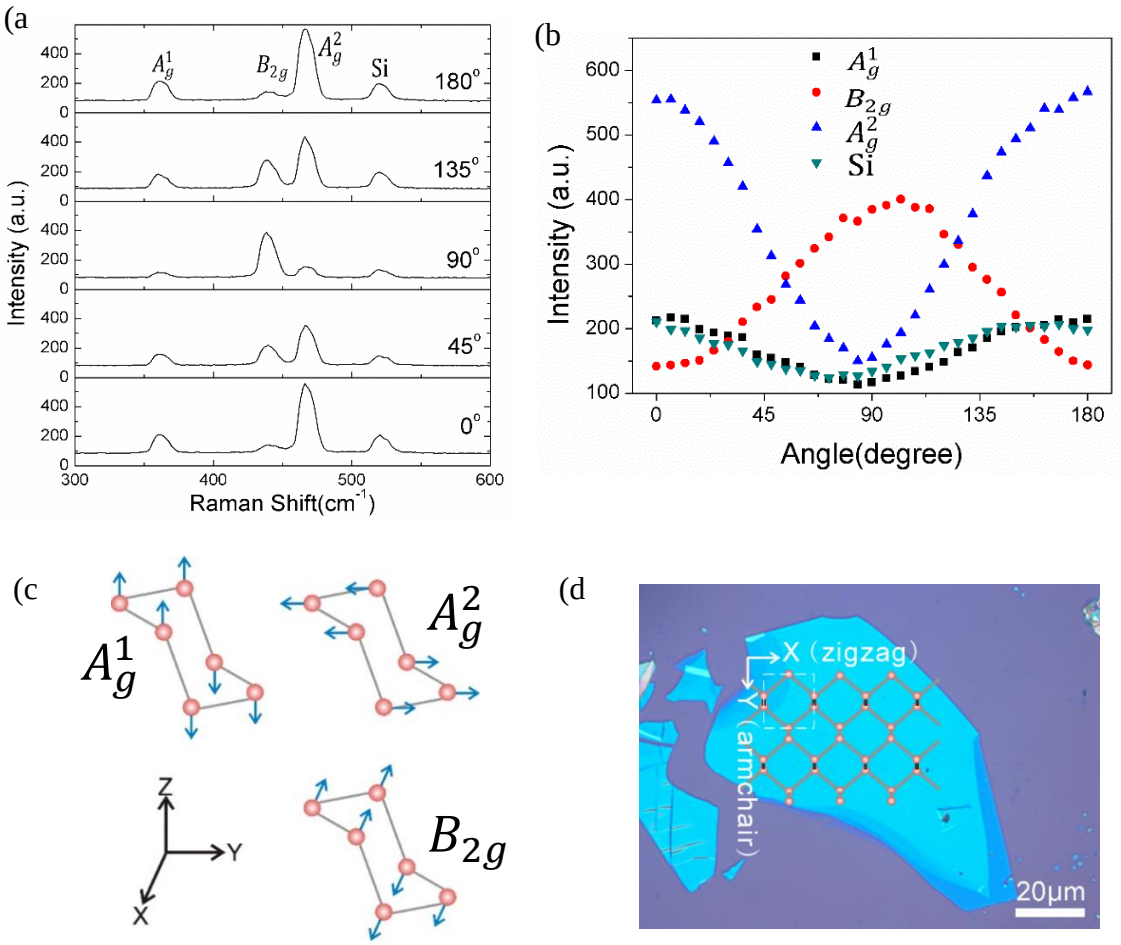

Figure 3.2 **Phosphorene crystalline orientation determination by polarization of Raman spectra. (a)** Raman spectra of 15L phosphorene under different polarization angles. **(b)** Polarization dependence of A_g^1, B_{2g}, A_g^2 modes in 15L phosphorene and the Raman peaks in silicon. **(c)** Schematic plot showing the vibration directions of A_g^1, B_{2g} and A_g^2 Raman modes. **(d)** Crystalline orientation of a 15L phosphorene flake, determined by angle-dependent Raman measurement.

The measurement results could be perfectly explained by the vibration directions of these three Raman modes in crystalline black phosphorus [104]. Figure 3.2c shows a schematic of the vibration direction of the phosphorus atoms in the different Raman modes [104]. In B_{2g}, A_g^2 and A_g^1 vibrational modes, the phosphorus atoms oscillate along the x (zigzag),

y (armchair) and z (out-of-plane) directions, respectively. When the laser polarization is parallel to the x direction (y direction), the intensity of the B_{2g} mode reaches the maximum (minimum) value; meanwhile, the intensity of the A_g^2 mode reaches the minimum (maximum) value. Our measurement result (Figure 3.2b) matched this theoretical prediction well. Based on this polarization-dependent Raman measurement, the crystalline orientation of the 15L phosphorene flake was quickly determined, as indicated in Figure 3.2d. This technique provided fast and precise determination of the crystalline orientation, without the need of complicated and high-resolution imaging systems such as STM or TEM.

Here, only the incident laser polarization and the oscillation direction of the atom vibration were considered. To more accurately interpret the polarization dependence of A_g^1, A_g^2 and B_{2g} Raman modes, more factors might need to be considered, such as polarization of the scattering light. Considering this, the polarization dependence of A_g^1 is probably intrinsic.

3.1.3 Temperature-dependent Raman spectra

Raman spectroscopy is another powerful tool which can be used to characterize the structural and electronic properties of few-layer phosphorene [108, 109]. In particular, temperature-dependent Raman study of few-layer phosphorene is important to further understand the fine structure and properties of that material, such as atomic bonds, thermal expansion and thermal conductivity.

The temperature dependence of the Raman spectra, measured at temperatures ranging from 20 °C to -160 °C in 5L phosphorene, is shown in Figure 3.3. The decreasing temperature leads to the blue shift of the Raman phonon modes A_g^1, B_{2g} and A_g^2. The measured temperature dependence of the Raman mode frequency shift in few-layer

phosphorene can be characterized by the linear equation $\omega = \omega_0 + \chi T$, where ω_0 is the mode frequency at zero K and χ is the first-order temperature coefficient. The measured χ values for modes A_g^1, B_{2g} and A_g^2 in 5L phosphorene are -0.023 $cm^{-1}/^oC$, -0.018 $cm^{-1}/^oC$ and -0.023 $cm^{-1}/^oC$, respectively (Figure 3.3b).

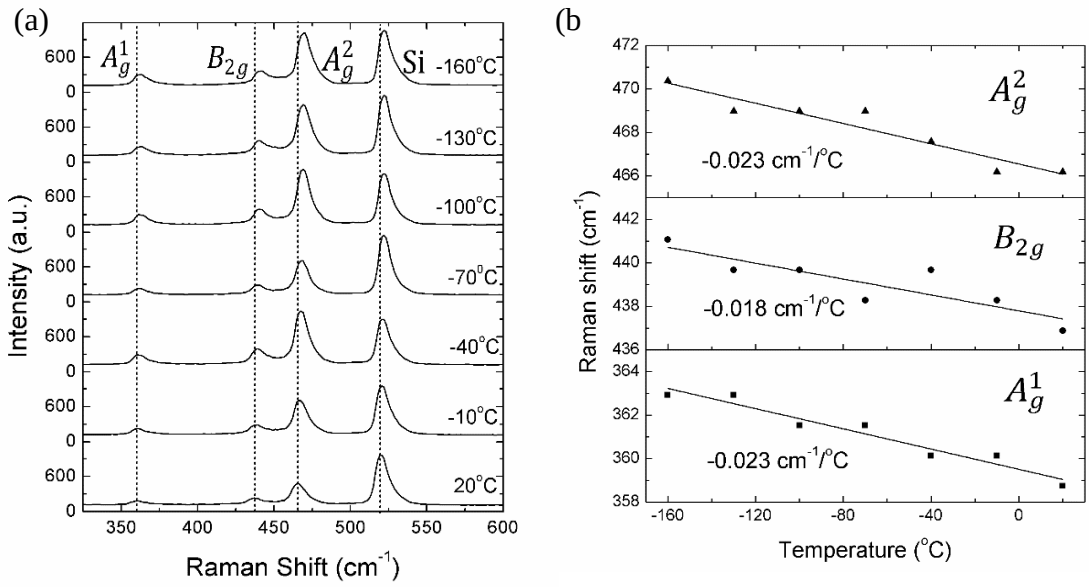

Figure 3.3 **Low-temperature Raman spectra of 5L phosphorene. (a)** Raman spectra of 5L phosphorene at temperatures ranging from 20°C to -160°C. **(b)** Temperature dependence of A_g^1, B_{2g} and A_g^2 Raman peak positions.

The change in the Raman shift with temperature is determined by the anharmonic terms in the lattice potential energy, which is related to the anharmonic potential constants, the phonon occupation number, and the thermal expansion of the crystal [110]. These measured χ values in 5L phosphorene were all greater in absolute value than those from both bi-layer graphene (-0.0154 $cm^{-1}/^oC$ for G peak) [108] and few-layer MoS_2 (-0.0123 $cm^{-1}/^oC$ and -0.0132 cm^{-1}/oC for A_{1g} and E_{2g}^1 modes respectively) [109]. This finding indicated that the phonon frequencies in few-layer phosphorene were more sensitive to

temperature modulation than those in graphene and MoS_2, which could be due to the superior mechanical flexibility of phosphorene originating from its unique puckered crystal structure [111].

3.2 Photoluminescence in few-layer phosphorene

3.2.1 Photoluminescence in few-layer phosphorene

The nature of the predicted direct bandgap in few-layer phosphorene would make it very promising for application in high-performance optoelectronic devices, compared to the indirect bandgap behaviour of most few-layer TMD semiconductors.

During the experimental processes, extraordinarily strong and highly layer-dependent photoluminescence (PL) in few-layer phosphorene was observed, confirming the predicted direct and layer-dependent bandgap nature of few-layer phosphorene.

The measured PL spectra (Figure 3.4a) in few-layer phosphorene were highly dependent on the number of layer (2 to 5 layers). Strong PL peaks at 961 nm, 1268 nm, 1413 nm and 1558 nm were observed in 2, 3, 4 and 5-layered phosphorene, respectively, which corresponded to energy peaks of 1.29 eV, 0.98eV, 0.88 eV and 0.80 eV, respectively. More PL measurement data from various few-layer (2-5 layer) phosphorene samples are shown in Table 3.1. Quite consistent PL centre wavelength and peak energy were observed from samples with the same number of layers.

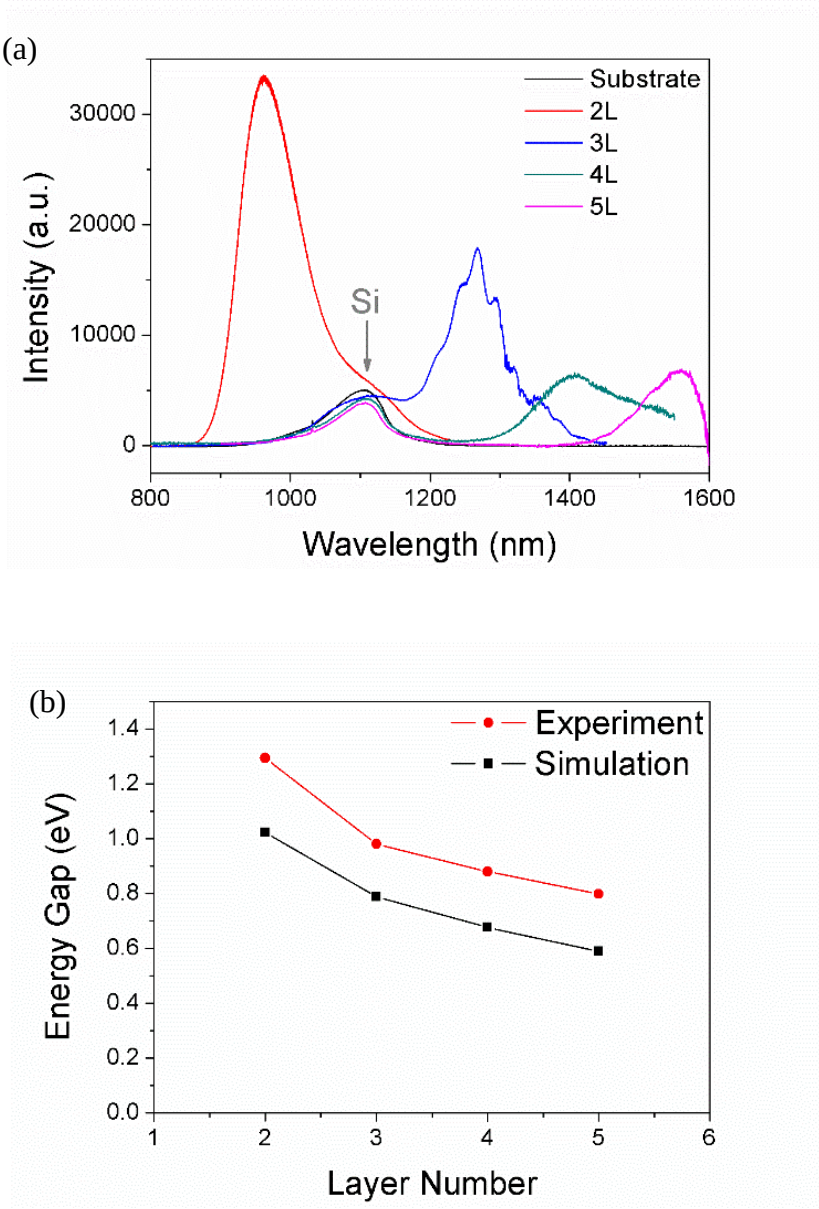

Figure 3.4 **PL spectra of thin-layer phosphorene. (a)** PL spectra of 2L, 3L, 4L and 5L phosphorene. Note: the tiny oscillation on the PL curve of the 3L phosphorene is due to the limitation error of the InGaAs detector. **(b)** Energy gap of 2L, 3L, 4L and 5L phosphorene from experimental PL spectra and theoretical simulation.

The measured PL peaks in Figure 3.4 are probably attributable to the nature of the excitons which represent the lower bounds of the fundamental bandgap values in few-layer phosphorene. The energy position of the measured PL peak increases rapidly as the

number of layers decreases. This finding indirectly confirms the theoretical calculation results that the bandgap of few-layer phosphorene increases rapidly as the number of layers decreases (Figure 3.4b), due to the quantum confinement effect.

Table 3.1 PL measurement data from various few-layer phosphorene samples.

Samples	No. **of layers**	**PL centre wavelength (nm)**	**Peak energy (eV)**
Sample 1	2L	961	1.29
Sample 2	2L	965	1.29
Sample 3	3L	1268	0.98
Sample 4	3L	1264	0.98
Sample 5	4L	1413	0.88
Sample 6	4L	1441	0.86
Sample 7	5L	1558	0.80
Sample 8	5L	1555	0.80
Sample 9	5L	1557	0.80

3.2.2 Internal luminescence quantum efficiency

Few-layer phosphorene has only several atoms in thicknesses, but the PL intensities from 2-5 layered phosphorene were all stronger than that from the thick (hundreds of microns) Si substrate (Figure 3.4a). This difference arises from the direct bandgap nature of few-layer phosphorene (Figure 3.5) and the indirect bandgap in silicon. Compared with the

indirect bandgap behaviour in few-layer MoS_2 [8], the universal direct bandgap nature of few-layer phosphorene bestows great advantages for various optoelectronic applications.

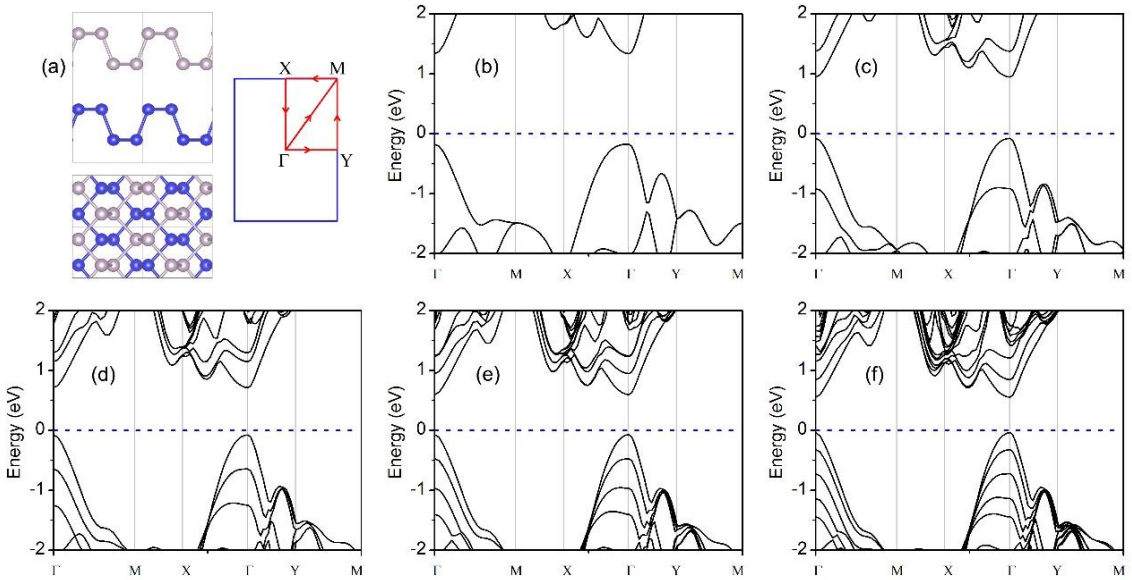

Figure 3.5 **Simulated band structures for phosphorene (1-5 layers) based on density function theory (DFT) calculation. (a)** Schematic plot showing the lattice structure of phosphorene. **(b)-(f)** shows the band structures for 1L to 5L phosphorene calculated using HSE06.

The band structures for 1-5 L phosphorene (Figure 3.5) were calculated using DFT calculations with the implementation of the Vienna ab initio simulation package (VASP) [112, 113]. Hybrid functionals (HSE06) [114] were adopted, together with the projector augmented wave method. A vacuum space of at least 20 Å was kept avoiding mirror interactions. The HSE06 approach is well known to involve an inaccurate description of the dispersion force and thus provides a poor estimation of the interlayer distance. Here all the structures were relaxed by using the optimized Becke88 van der Waals (optB88-vdW) functional [113]. The first Brillouin zone was sampled with 10×8×1 Monkhorst-

Pack k-meshes for the structure relaxation, and a kinetic energy cut off of 500 eV was adopted. The lattice constant was relaxed until the change of total energy was less than 0.01 meV and all the forces on each atom were less than 0.01 eV/Å, which was sufficient to obtain relaxed structures.

Surprisingly, the PL peak intensity increased dramatically when the number of layers decreased, despite the reduced amount of material (Figure 3.6). As in the method used with MoS_2 [8], the luminescence quantum efficiency η_{PL} in few-layer phosphorene could be evaluated by comparing the PL intensity I_{PL} that was normalized by the number of layers. This normalized PL peak intensity (Figure 3.6) indirectly reflected the intrinsic luminescence quantum efficiency η_{PL} [8]. This indicated that the intrinsic luminescence quantum efficiency was highly dependent on the number of layers in few-layer phosphorene. As shown in Figure 3.6, the intrinsic luminescence quantum efficiency in 2L phosphorene was more than one order of magnitude higher than that in 5L phosphorene.

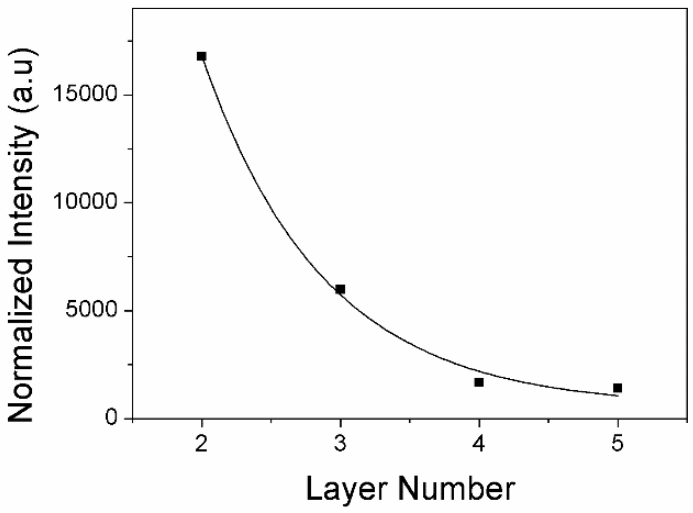

Figure 3.6 **Layer-dependence of PL peak intensity that is normalized by the number of layers.**

The strong PL in few-layer phosphorene arose from direct electronic transitions with a high radiative recombination rate. The internal luminescence quantum efficiency from such direct electronic transitions in few-layer phosphorene could be approximated by $\eta_{PL} \approx k_{rad}/(k_{rad} + k_{defect} + k_{relax})$, where k_{rad}, k_{defect} and k_{relax} are, respectively, rates of radiative recombination, defect trapping and electron relaxation within the conduction and valence bands, similar to that in MoS_2 [8]. Both k_{rad} and k_{relax} were highly related to the density of states and the band structures [115].

This strong layer-dependent internal quantum efficiency could be understood from the layer-dependent band structures in few-layer phosphorene (Figure 3.5). As the number of layers increased from monolayer to five-layer, increasing numbers of band valleys and band maxima showed up within both conduction and valence bands, respectively. Those emerging valleys (maxima) in the conduction (valence) band significantly changed the density of distribution of states for electrons (holes). In particular, the states provided by those valleys or maxima at the off-Γ points highly enhanced the relaxation rates within the conduction or valence bands, leading to lower internal quantum efficiency in 5L phosphorene compared to that in 2L. The experimental data indicated the rich PL physics in few-layer phosphorene.

During all the Raman and PL measurements, the samples were placed in a microscope-compatible chamber with a slow flow of nitrogen gas, to prevent the few-layer phosphorene from reacting with moisture or other possible reactants from the environment. As shown in Figure 3.7, the microscope images and PL performance revealed that the nitrogen chamber protection method worked well to prevent degradation of the phosphorene.

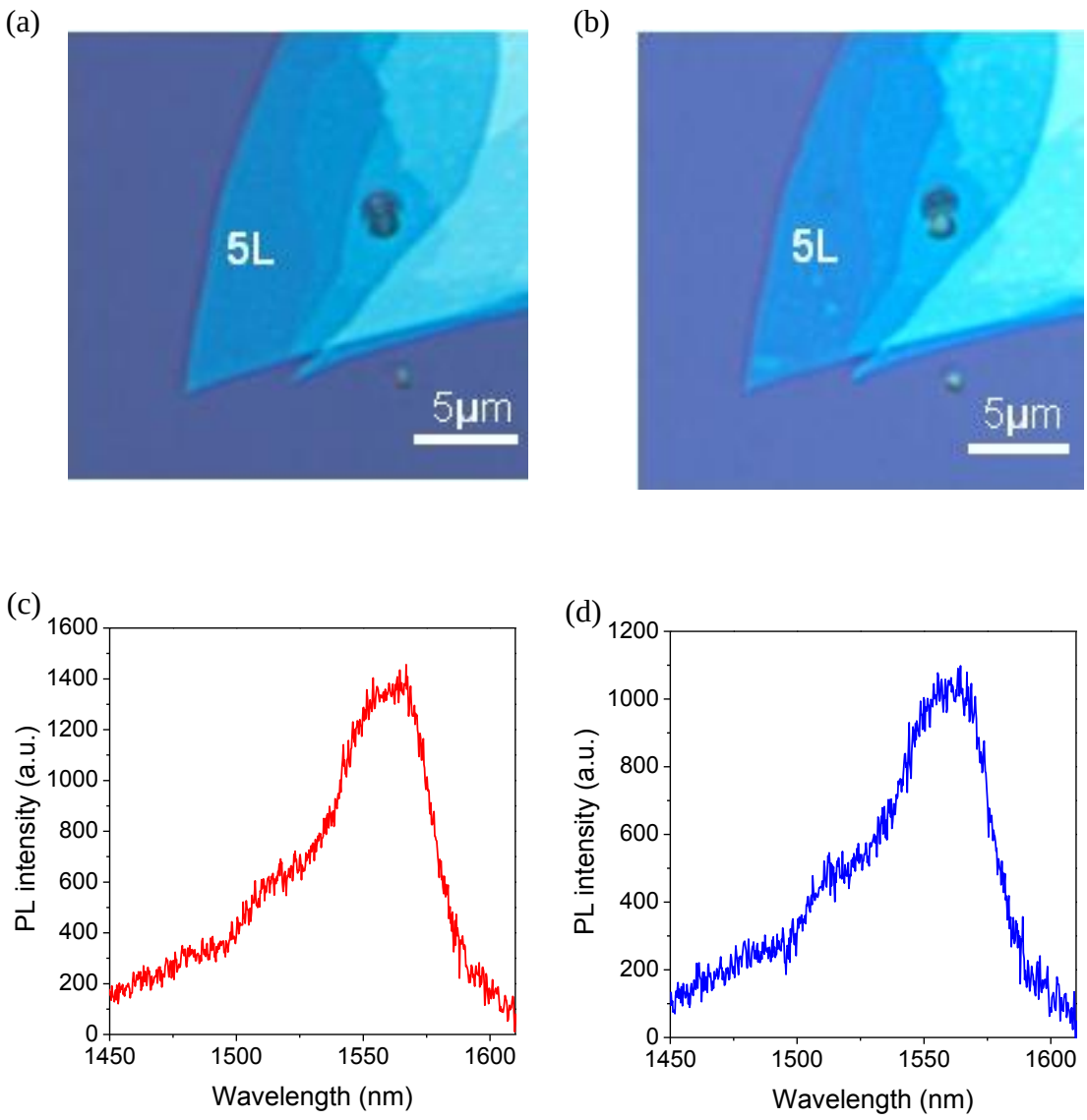

Figure 3.7 **Phosphorene performance before and after nitrogen chamber protection. (a)-(b)** Optical microscope images of a 5L phosphorene in nitrogen chamber protection when it was just loaded in (a) and after 16 hours (b). **(c)-(d)** Measured PL spectra of the 5L phosphorene in nitrogen chamber protection when it was just loaded in (c) and after 16 hours (d).

3.3 Summary

In conclusion, the measured Raman peaks at 359 cm^{-1}, 437 cm^{-1} and 466 cm^{-1} were attributed to the A_g^1, B_{2g} and A_g^2 phonon modes in the crystalline few-layer phosphorene

flakes, which matched the observations in bulk black phosphorus well. The temperature-dependent Raman measurements demonstrated that few-layer phosphorene was more sensitive to temperature modulation than graphene and MoS_2, which could be due to the superior mechanical flexibility of phosphorene originating from its unique puckered crystal structure. Also, the highly angle-dependent Raman spectra from a phosphorene flake facilitated rapid determination of the crystalline orientation of the flake without TEM or STM.

In the PL study, the strong and layer-sensitive PL in 2-5 layered phosphorene was observed. The energy gaps, determined from the PL spectra, were highly dependent on the number of layers, which matched the theoretical simulation well. This PL measurement provided very useful information for study of the exciton nature and the electronic structures in few-layer phosphorene.

Chapter 4 Extraordinarily bound quasi-one-dimensional trions

Chapter 3 described the PL phenomenon in few-layer phosphorene which provides information about photon-electron energy transfer (inelastic light-matter interactions). The PL peaks in Chapter 3 were attributed to excitons, representing lower bounds on the fundamental bandgap values in few-layer phosphorene. A neutral exciton is a bound quasi-particle state between one electron and one hole through a Coulomb interaction, similar to a neutral hydrogen atom.

In this chapter, the transformation dynamics of excitons and trions are studied. Trions, having a many-body bound state, are formed through the interplay between exciton and carrier. The density of trions can be modulated by controlling the carrier doping level using methods such as electrostatic modulation [32], and chemical doping [116]. In this project, electrostatic modulation was applied to tune the trion density.

Like the PL attributed to excitons, the PL from trions also involves inelastic light-matter interactions and yields information about photon-electrons energy transfer. A trion is a charged exciton composed of two electrons and one hole (or two holes and one electron), analogous to H^- (or H_2^+) [103]. Trions have been of considerable interest in the fundamental studies of many-body interactions, such as carrier multiplication and Wigner crystallization [117].

In contrast to the exciton, a trion has an extra charge with nonzero spin, which can be used for spin manipulation [118]. More importantly, the density of trions can be electrically tuned by the gate voltage, facilitating remarkable optoelectronic applications [103, 117-120]. For those purposes, a large trion binding energy is critical in order to

overcome room-temperature thermal fluctuations as well as to widen the spectral tuning range.

4.1 Exciton and trion dynamics in 3L phosphorene

4.1.1 Gate-dependence of exciton and trion in 3L phosphorene MOS device

The new type of 2D material described in this thesis, few-layer phosphorene, is unstable and does not survive well in many standard nanofabrication processes [87, 121]. To overcome this instability challenge, special fabrication and characterization techniques were designed. Mechanical exfoliation was used to drily transfer [87] a phosphorene flake onto a SiO_2/Si substrate (275 nm thermal oxide on n^+-doped silicon). The phosphorene was placed near a gold electrode that had been pre-patterned on the substrate. Another thick graphite flake was similarly transferred to electrically bridge the phosphorene flake and the gold electrode, forming a MOS device (Figure 4.1). These two steps could avoid the possible sample cracks if the thin phosphorene flake was transferred directly onto the unflat edge of the gold electrode. This fabrication procedure kept the phosphorene free from chemical contamination by minimizing the post-processes after the transfer. In the measurement, the gold electrode was grounded, and the n^+-doped Si substrate functioned as a back gate, providing uniform electrostatic doping in the phosphorene (Figure 4.1a).

Another unique challenge in working with unstable phosphorene is the identification of the number of layers. AFM is typically unreliable for the identification of very-few-layer phosphorene (one or two layers) because of its slow scanning speed and the potential contact contamination. In the present project, PSI was used to quickly and precisely identify the number of layers of the phosphorene by measuring the OPL (Figure 4.1c, d). After the PSI measurement, the sample was placed into a microscope-compatible chamber for photoluminescence (PL) measurements, with a slow flow of nitrogen gas

used to prevent degradation of the sample [121]. The number of layers was further confirmed by the measured PL spectra [122].

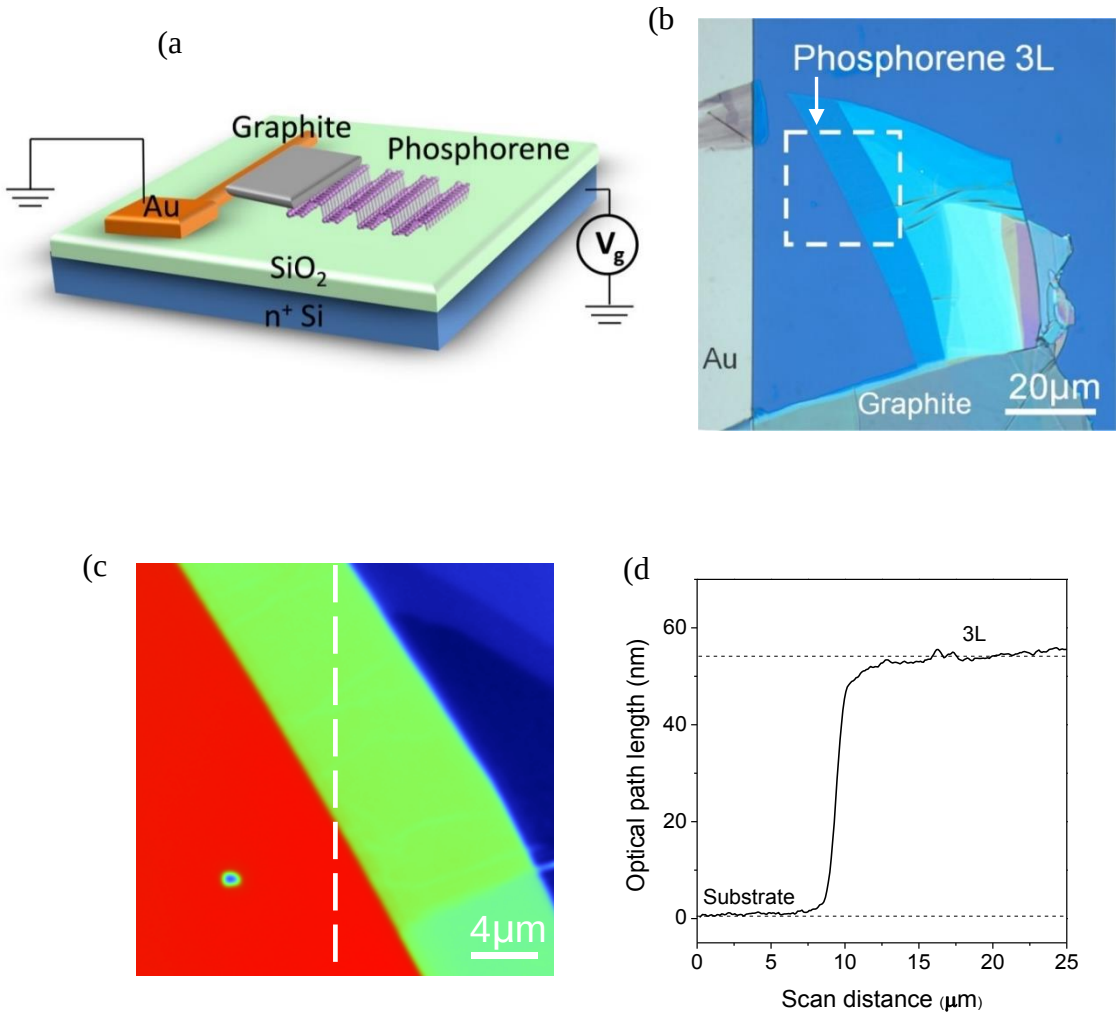

Figure 4.1 **Phosphorene characteristics and devices. (a)** Schematic plot of a phosphorene MOS device. **(b)** Optical microscope image of the MOS device with trilayer phosphorene (labelled "3L"). **(c)** PSI image of the region inside the box indicated by the dashed line in (b). (**d)** PSI-measured OPL values versus position for 3L phosphorene along the dashed line in (c).

The reversible electrostatic tunability of the exciton charging effects from positive (A^+) to neutral (A°) in a 3L phosphorene MOS device is demonstrated in Figure 4.2, using gate-dependent PL measurements. The measured PL spectra exhibit two clear peaks with central wavelengths at ~1100 and ~1320 nm, whose intensities are highly dependent on the back-gate voltage. The higher energy peak (~1100 nm) is attributed to the exciton emission, and the lower energy peak (~1320 nm) is due to the trion emission [103]. To show the evolution of the exciton and trion, a gate voltage V_g was applied to pump extra charges into the phosphorene. Lorentzian curves were used to fit the measured PL spectra to extract the exciton and trion spectral components, as indicated by the red and blue curves in Figure 4.2a, respectively. The Si/SiO_2 substrate also has a PL peak at ~1100 nm that is independent of the gate voltages (Figure 4.2). The emission intensity from the substrate is far weaker than that from phosphorene, and it can easily be separated from the measured voltage-dependent PL spectra (Figure 4.2).

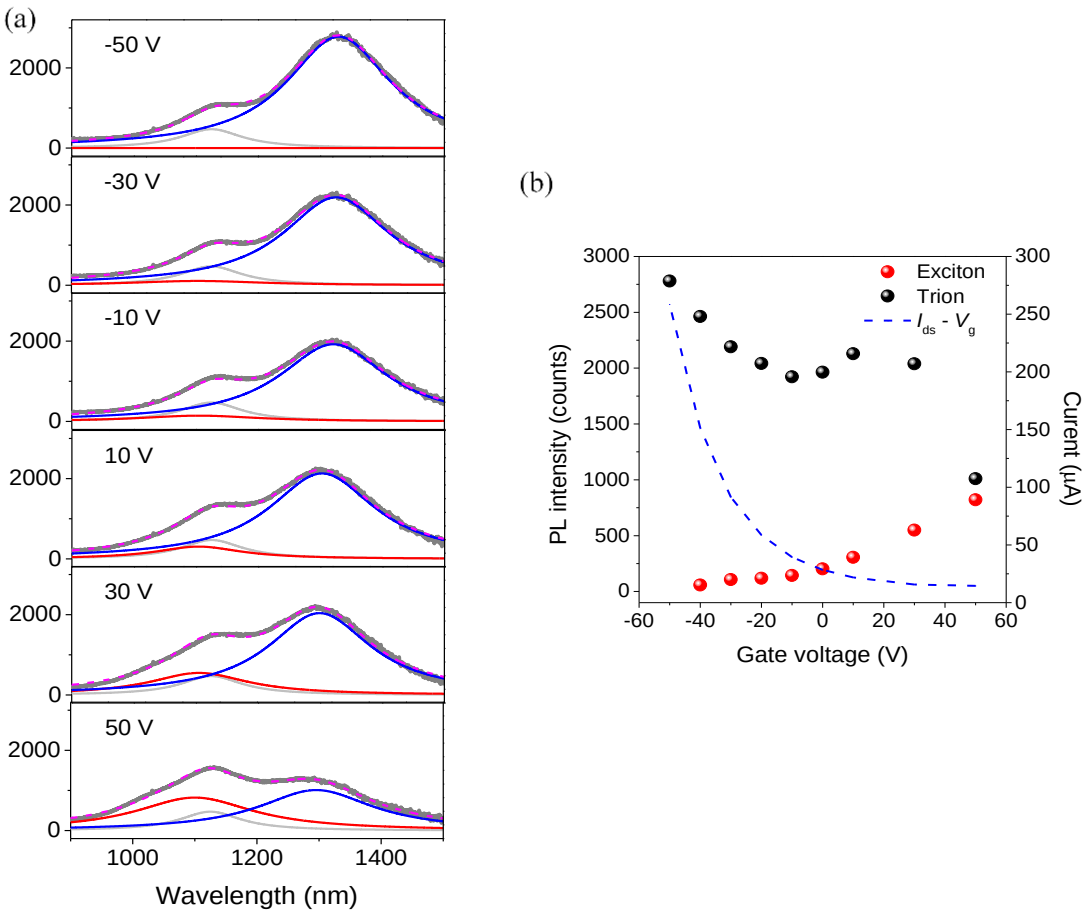

Figure 4.2 **Gate-dependence of the exciton and trion in a 3L phosphorene MOS device. (a)** Measured PL spectra (solid dark grey lines) under various back-gate voltages. PL spectra are fitted to Lorentzians (solid red lines are the exciton components, solid blue lines are the trion components, solid light grey lines are the Si components, and dashed pink lines are the cumulative results for the fitting). **(b)** PL intensity of exciton and trion as a function of gate voltage; drain-source current as a function of gate dependence**.**

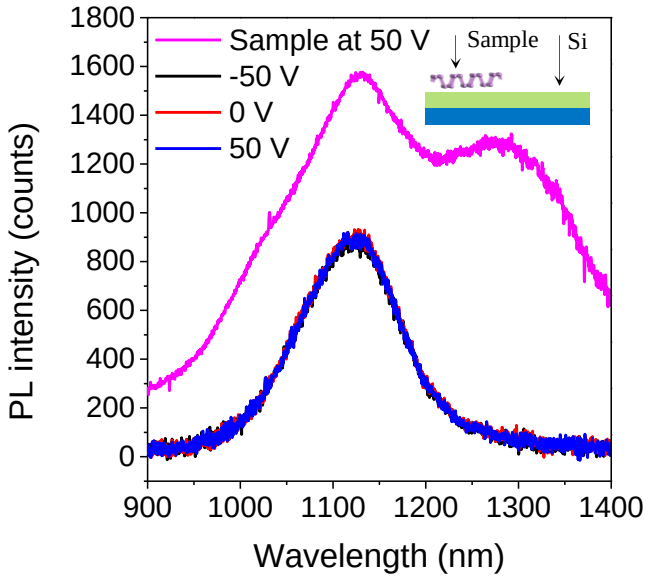

Figure 4.3 **PL from the SiO_2/Si substrate used for the MOS device under different back-gate voltages**. PL spectrum of the 3L phosphorene MOS at gate voltage of 50 V (shown in Figure 4.2) is also plotted here for comparison. Insert: Schematic of the measurement positions. The PL measurement conditions are kept the same for the phosphorene sample and the SiO_2/Si substrate.

At a voltage bias of -50 V, positive charges are pumped into the phosphorene, and almost all excitons become charged trions. As a result, the PL emission from neutral excitons A° at a wavelength of ~1100 nm is absent (Figure 4.2a). In contrast, the PL emission from positive trions A^+ at ~1300 nm is extremely strong. As the positive charges are gradually depleted by changing the voltage from -50 to 50 V, the PL emission from the neutral excitons becomes increasingly prominent at ~1100 nm, which is correlates with the I_{ds}-V_g dependence, while the PL emission of the positive trions simultaneously becomes progressively weaker (Figure 4.2a, b). From the measured field-effect transistor (Figure 4.4) I_{ds}−V_g characteristics (Figure 4.2b), it is clear that the emergence of the charged

exciton peak correlates with the onset of electrostatic doping, which is similar to the modulation of trions in monolayer MoS_2 [32].

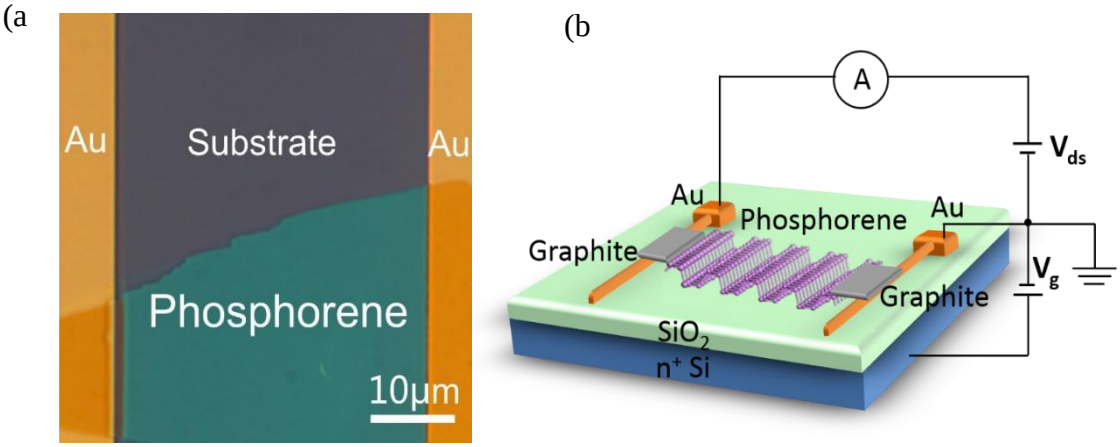

Figure 4.4 **Optical microscope image (a) and schematic (b) of device structure of a few-layer phosphorene field effect transistor**

That transfer of spectral weight is directly caused by the depletion of positive charges, i.e., A^+ - h → A°, where h represents a hole. In principle, negative trions can also be expected when V_g is large enough to introduce sufficient electron doping to offset the intrinsic hole doping in the phosphorene layer, which can be realised by replacing the thick oxide layer with thin high-*k* dielectric materials.

Besides electrostatic doping, substrate-induced doping can also be used to modify the spectral weight between neutral excitons and trions in the PL spectra from 2D semiconductors [78]. For instance, the trion emission dominates in 1L MoS_2 on the SiO_2 substrate, while the neutral exciton emission dominates in 1L MoS_2 on the gold substrate,

since 1L MoS_2 has initial n-type doping and the gold substrate can reduce the doping level via charge transfer between the gold−MoS_2 interface [123].

4.1.2 Photoluminescence in 3L phosphorene on gold substrate

Although the tunability of excitons and trions through electrical gate was obvious in Figure 4.2, the broad bandwidth of the exciton at ~1100 nm made it difficult to completely and precisely separate the exciton from the bound ground silicon peak, which was also located at roughly 1100 nm. In order to determine the accurate exciton peak position for 3L phosphorene, the same technique was used to transfer a phosphorene flake onto a SiO_2/Si substrate with a ~100nm gold layer on the top to remove the influence from the silicon. As shown in Figure 4.5a, the unambiguous 3L phosphorene exciton peak is observed at ~1080nm but the peak from silicon is absent. However, the trion peak from the ~1300nm is also absent due to the quenching effect of the contact between the gold and the 3L phosphorene.

When the 3L phosphorene is in contact with the gold, because of the mismatching of the Fermi levels, electrons from the 3L phosphorene flow onto the surface of the gold, leading to a bend in the band structure and forming a Schottky barrier (Figure 4.5b) [124, 125]. Thus, during the PL measurements, the excited holes will be pushed onto the surface of the gold by the potential difference of the Schottky barrier and then annihilated by the electrons in the gold, resulting in a temporary increase of the electrons/holes ratio in the 3L phosphorene. Along with the quenching effect, the 3L phosphorene presents an intrinsic status instead of a p-type doped status, causing the absence of the trion peak at ~1300nm.

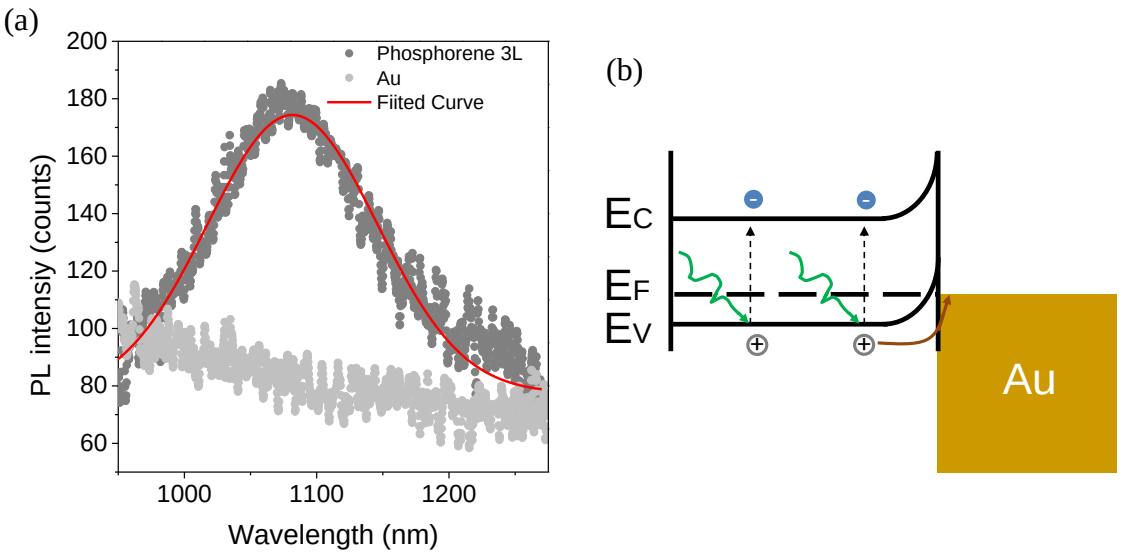

Figure 4.5 **3L phosphorene on gold. (a)** Spectra of 3L phosphorene on gold and the background **(b)** Schematic plot of quenching effect of 3L phosphorene on gold.

In Figure 4.3, the PL spectra measured from the SiO_2/Si substrate at the back-gate voltages of -50, 0 and 50 V are almost identical, originating from the voltage independent Si PL at ~1100 nm; whereas the PL peak intensity at ~1100 nm originating from the 3L phosphorene MOS device under the back-gate voltage if 50 V is even higher than that from the substrate. On this basis, it is likely that the ~1100 nm PL peak on the 3L phosphorene derives from both the phosphorene and the Si substrate. The emission intensity from the substrate is much weaker than that from the phosphorene and can be easily separated from the measured voltage-dependent PL spectra (Figure 4.5a).

4.1.3 Power dependence of trion emission

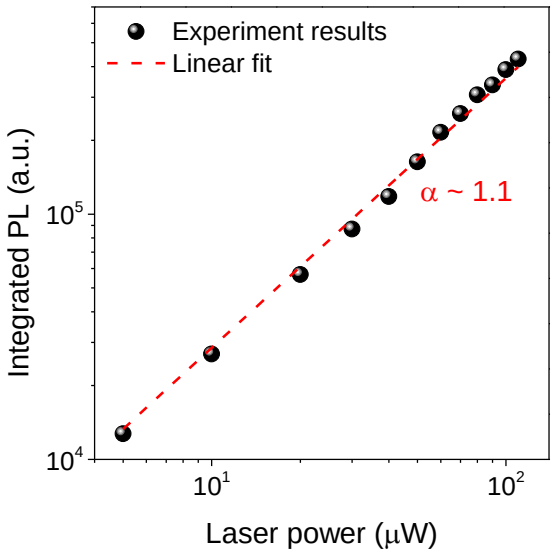

Figure 4.6 **The experimental results and linear fit for integrated PL versus laser power under double logarithmic scale.** The slope of the linearly fitted line is 1.1.

In the experiments, doping dependence of the low-energy emission peak at ~1300 nm was opposite to that of the high-energy emission peak, which agreed well with the unique behaviour of the trions [32]. To further confirm the trion assignment for the low-energy PL emission at ~1300 nm, excitation-power-dependent PL measurements were undertaken (Figure 4.6). As shown by Yu et al. [126] and Heinz et al. [127], the integrated PL intensities of the localized excitons, trions/excitons, and biexcitons grew sublinearly, linearly and quadratically, respectively, with their excitation powers [123, 128]. From the present measurements, the integrated PL of the low-energy peak at ~1300 nm from the 3L phosphorene sample grew linearly with the excitation power (α = 1.1,Figure 4.6), indicating that the peak at ~1300 nm indeed derived from the trions and not from biexcitons or localized excitons, whereas the high-energy PL peak (~1100 nm) was determined to be derived from excitons.

4.1.4 Trion binding energy in 3L phosphorene

As shown in Figure 4.7, the peak energy difference between excitons and trions decreased from 188 to 170 meV when the gate voltage increased from −50 to +50 V. The central wavelengths of the emission peaks from A^0 and A^+ were slightly dependent on the back-gate voltages (Figure 4.7 and Figure 4.8), which could be due to the change in Fermi level at different biases [32, 126].

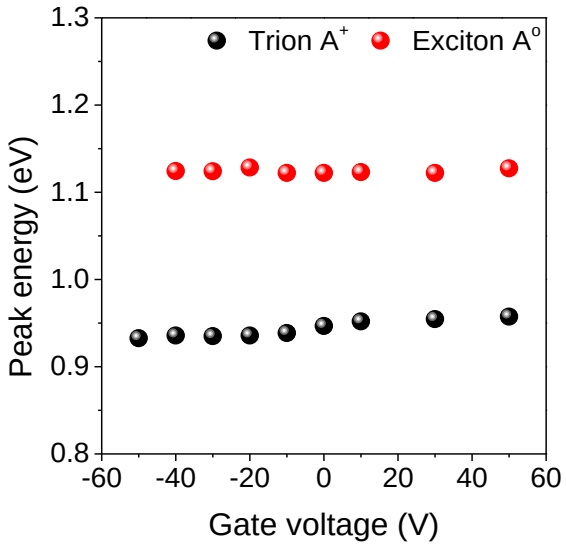

Figure 4.7 **Peak energy of exciton and trion as a function of gate voltage.**

On the basis of the measured I-V curve (Figure 4.2b), charge neutrality was achieved at a gate bias of ~60 V, corresponding to E_F = 0, which was consistent with a previous report [59]. The gate voltage was then converted to the induced hole doping density using the equation:

$$ne = CV_g \tag{4.1}$$

where the back-gate capacitance $C = 1.2 \times 10^{-8} Fcm^{-2}$. Next, the hole doping density was further converted to the Fermi energy through relation [58]:

$$E_F = \frac{\hbar^2 \pi n}{2 m_h e^2} \tag{4.2}$$

using the hole effective mass $m_h = \sqrt{m_x^* m_y^*} = 0.41 m_0$

where m_0 is the mass of the free electron.

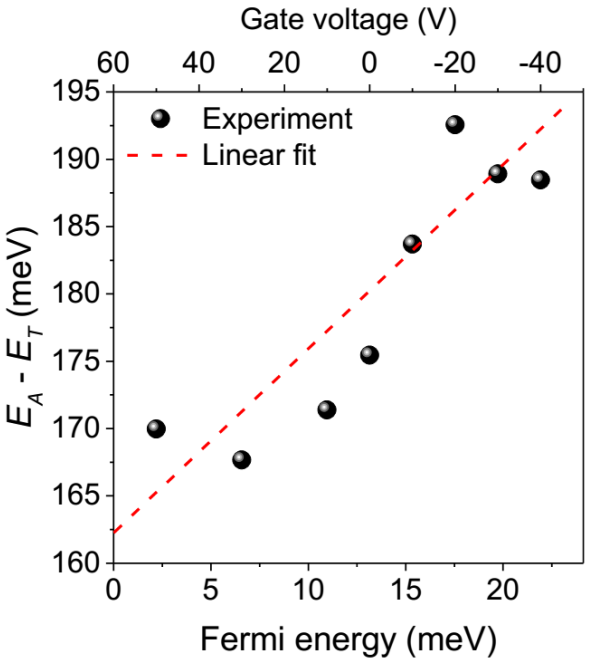

Figure 4.8 **The difference in the exciton and trion energies, ($E_A - E_T$), as a function of Fermi energy E_F.** The dashed red line, a linear fit to the E_F-dependence, has an intercept of 162 meV, which determines the trion binding energy.

The peak energy difference between A^0 and A^+ exhibited a large value of ~162 meV at zero Fermi level (Figure 4.8), which was the trion binding energy [129, 130]. Remarkably, such a large binding energy has not been observed in any other higher-than-one-dimensional material. It is comparable to that observed in 1D semiconductors [128, 130] and is approximately one order of magnitude larger than that from TMD 2D semiconductors [60, 121]. Positive trions with a large binding energy have been observed in multiple 3L phosphorene MOS devices (Figure 4.9).

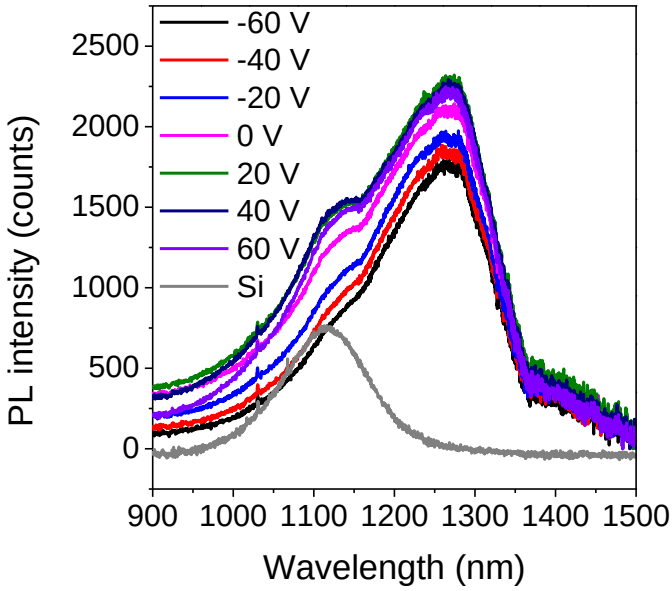

Figure 4.9 **Gate-dependence of the exciton and trion in another 3L phosphorene MOS device.** The Si PL spectrum measured from the substrate of this device is also shown for comparison. Note that the Si PL peak intensity here is slightly different from the one that shown in Figure 4.3, due to a slight difference in the laser excitation power used in these two measurements.

4.2 Exciton and trion dynamics in 1L $MoS_{2x}Se_{2(1-x)}$ (x=0.45)

The 3L phosphorene exhibited a large trion binding energy of ~162 meV at zero Fermi level. Such a large binding energy, comparable to that from 1D semiconductors [128, 130], has not been observed in any other higher-than-one-dimensional material.

For comparison, gate-dependence measurement was conducted on 1L $MoS_{2x}Se_{2(1-x)}$ (x=0.45) and trion binding energy was also calculated. After the monolayer $MoS_{2x}Se_{2(1-x)}$ (x=0.45) sample preparation and characterization, temperature and electrical co-modulation was applied on the MOS device to investigate exciton and trion dynamics.

All the PL measurements were conducted by a T64000 micro-Raman/PL system equipped with both a charge-coupled device and InGaAs detectors, along with a 532 nm Nd:YAG laser as the excitation source.

$MoS_{2x}Se_{2\,(1-x)}$ has become a special member of the 2D TMD family and has attracted considerable research interest. Most studies [131-135] have focused on experimentally growing $MoS_{2x}Se_{2(1-x)}$ and theoretically analysing its composition-dependent properties. It was found that $MoS_{2x}Se_{2(1-x)}$ had a unique continuous optical bandgap [135] between monolayer MoS_2 (1.87eV) and $MoSe_2$ (1.55eV) with the change of S/Se ratio. The ability to continuously tune a bandgap permits flexibility in fabricating high-performance novel optoelectronic devices [135]. However, study of the exciton and trion dynamics in monolayer $MoS_{2x}Se_{2(1-x)}$ is still lacking, but is important for the exploration of new excitonic devices based on monolayer $MoS_{2x}Se_{2(1-x)}$.

4.2.1 Gate-dependence of exciton and trion in 1L MoSSe

Figure 4.10a displays the calculated band diagram of monolayer (1L) $MoS_{2x}Se_{2(1-x)}$ and the metal-oxide-semiconductor (MOS) structure. The band structure of monolayer $MoS_{2x}Se_{2(1-x)}$ (x=0.45) was calculated (Figure 4.10a) using first-principle calculations based on density functional theory (DFT). The band structure diagram indicated that monolayer $MoS_{2x}Se_{2(1-x)}$ (x=0.45) had a direct bandgap at K point and the bandgap was about 2.6 eV, which matched previous experimental results [131-135] well.

In the experimental procedures, the monolayer $MoS_{2x}Se_{2(1-x)}$ (x=0.45) was prepared and measured via the same methods as these used for phosphorene. Monolayer $MoS_{2x}Se_{2(1-x)}$ (x=0.45) was prepared by mechanical exfoliation techniques from the bulk crystal purchased from the company named HQ Graphene. Then a monolayer $MoS_{2x}Se_{2(1-x)}$ (x=0.45) flake was drily transferred [87] onto the SiO_2/Si (275 nm thermal oxide on n^+-

doped silicon) substrate and placed near a gold electrode which had been pre-patterned on the substrate.

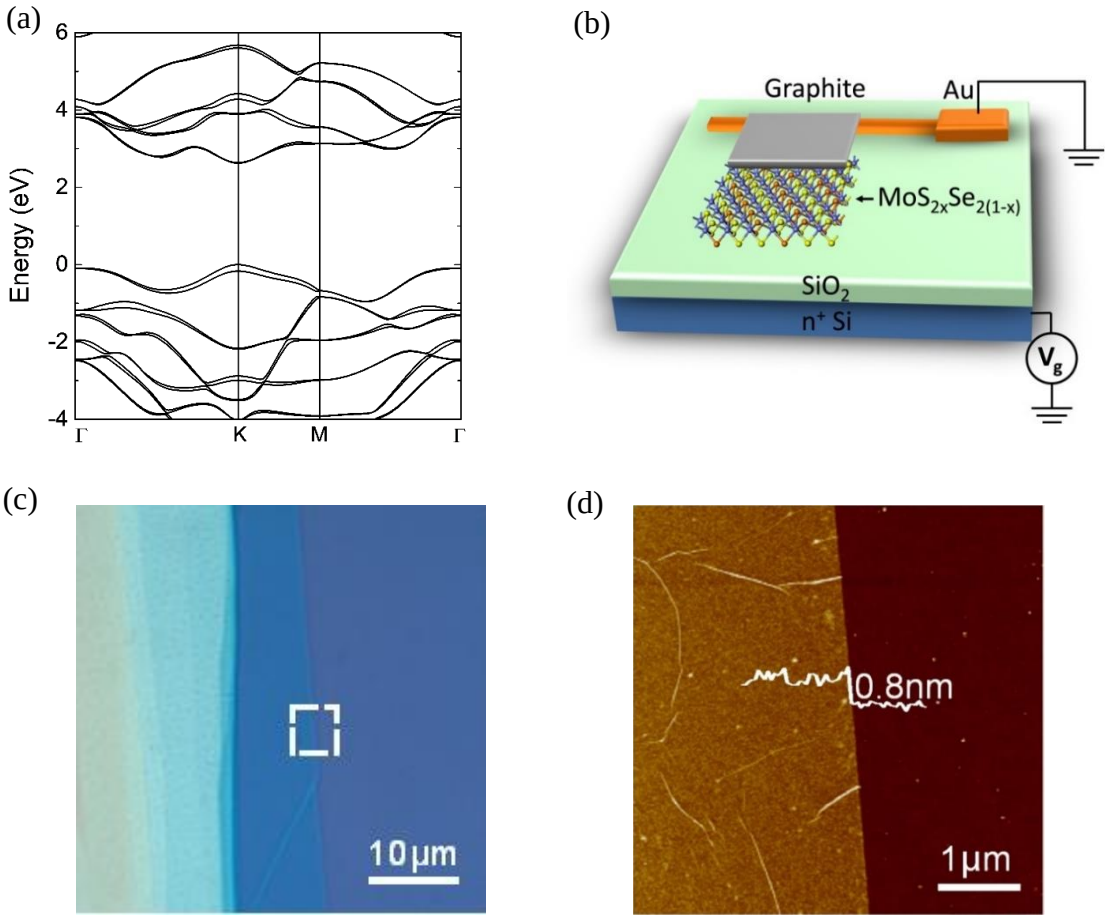

Figure 4.10 **Calculated band diagram of monolayer (1L) $MoS_{2x}Se_{2(1-x)}$ and the metal-oxide-semiconductor (MOS) structure. (a)** Band diagram of 1L $MoS_{2x}Se_{2(1-x)}$, indicating the direct bandgap at K point. **(b)** Schematic plot of a 1L $MoS_{2x}Se_{2(1-x)}$ MOS device structure. Graphite is used as the electrical bridge. **(c)** Optical microscope image of the 1L $MoS_{2x}Se_{2(1-x)}$ MOS device. **(d)** AFM image of the 1L $MoS_{2x}Se_{2(1-x)}$ MOS device.

Another thick graphite flake was similarly exfoliated and transferred onto the substrate to electrically bridge the $MoS_{2x}Se_{2(1-x)}$ (x=0.45) sample and the gold electrode, forming a MOS device (Figure 4.10). This fabrication process minimized the post-processes after

the monolayer $MoS_{2x}Se_{2(1-x)}$ (x=0.45) flake had been transferred, as well as keeping $MoS_{2x}Se_{2(1-x)}$ (x=0.45) free of chemical contamination. During the measurement, the gold electrode was grounded and the doped Si substrate worked as a back gate, providing uniform electrostatic doping in $MoS_{2x}Se_{2(1-x)}$ (x=0.45) (Figure 4.10b). Figure 4.10c shows an optical microscope image of the MOS structure, and Figure 4.10d is the AFM image from the box enclosed by a dashed line in Figure 4.10c. The thickness of the sample identified by AFM was about 0.8 nm, clearly signifying that it was a monolayer $MoS_{2x}Se_{2(1-x)}$ (x=0.45) sample [135, 136].

Figure 4.11shows the PL spectra of monolayer $MoS_{2x}Se_{2(1-x)}$ (x=0.45) with back-gate voltage V_g ranging from -70 to 70V at 83 K. When the temperature was reduced to 83K, the PL emission peak split into two obvious peaks located separately at ~696 nm (1.781 eV) and ~710 nm (1.746 eV) (Figure 4.11a). In accordance with previous research on charged excitons [32, 129], the higher energy sharp peak was assigned as the neutral exciton peak (X^0) and the lower energy sharp peak was assigned as charged excitons (negatively charged trion X^-) (Figure 4.11a). In Figure 4.11a, Lorentzian fitting was used to extract the exciton and trion peaks. The dark grey curve represents the original data from experiments, the red and blue lines are fitted exciton and trion components respectively, and the dashed pink lines are the cumulative results for the fitting. The intensity weight of the exciton and trion peaks could be tuned by back-gate voltage and the intensity of the high-energy exciton peak was stimulated under negative voltage bias (V_g<0).

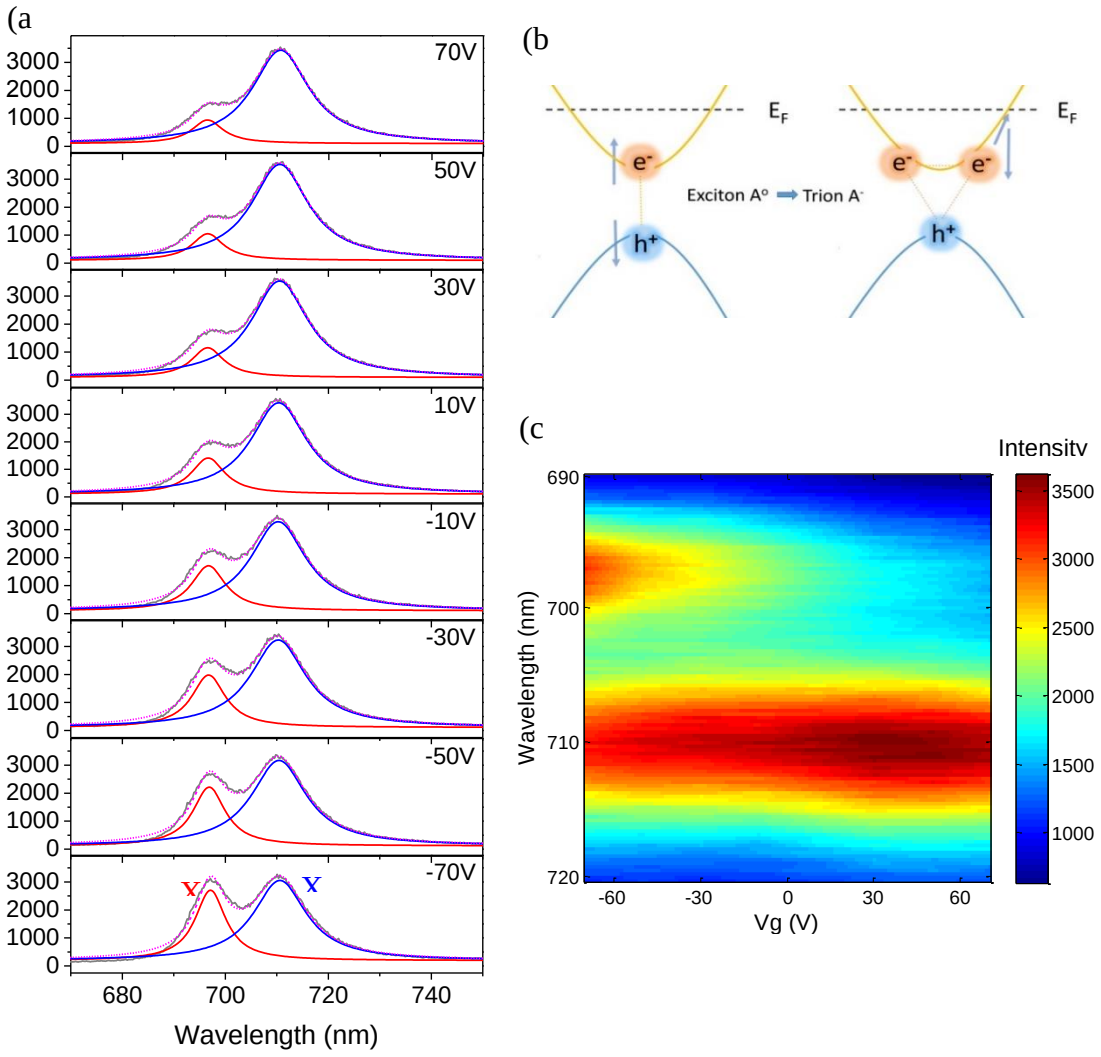

Figure 4.11 **Electrical modulation of the exciton and trion dynamics for 1L $MoS_{2x}Se_{2(1-x)}$. (a)** Measured PL spectra (solid dark grey lines) of 1L $MoS_{2x}Se_{2(1-x)}$ sample at 83 K under different back-gate voltages. PL spectra are fitted to Lorentzians (solid red lines are the exciton components, solid blue lines are the trion components, and dashed pink lines are the cumulative results for the fitting). **(b)** Schematic plot of the gate-dependent exciton and trion quasi-particle transitions. **(c)** The PL spectra of 1L $MoS_{2x}Se_{2(1-x)}$ are plotted as the function of back-gate voltage. The exciton and negative trion emissions are shown as bright spots in the 2D plot.

Figure 4.11b is a schematic diagram of exciton (X^0) and trion (X^-) transition under the modulation of the back gate [32]. Electrons and holes are shown as yellow and blue circles with e^- and h^+ in the middle. The monolayer $MoS_{2x}Se_{2(1-x)}$ (x=0.45) sample is initially negatively doped. When positive back-gate voltage is applied, electrons are injected into the sample, forming a negatively charged exciton (or negative trion X^-). This process can be described as $e + X^0 \rightarrow X^-$. Conversely, when a negative back gate is applied, holes are injected, resulting in an inverse process.

To obtain a better view of the gate-modulated exciton-trion transition process, a colour map of PL spectra with the change in back-gate voltage is shown in Figure 4.11c. When V_g is near zero, the spectrum presents a narrow high-energy exciton peak (labelled X^0) at ~696 nm (1.781 eV) and a broad low-energy trion peak (labelled X^-) at ~710 nm (1.746 eV). When the positive V_g increases the exciton peak fades, while the negative trion peak becomes increasingly strong. In contrast, with the increase of negative voltage, the exciton peak is strengthened and the negative trion peak is weakened. The observed gate-dependent PL spectra clearly demonstrate exciton and trion transition with external electrical doping.

4.2.2 Power dependence of exciton and trion emission in 1L $MoS_{2x}Se_{2(1-x)}$ (x=0.45)

To further confirm the trion assignment for the low-energy PL emission at ~710 nm, excitation power-dependent PL measurements were conducted (Figure 4.12a). As shown by Yu et al. [126] and Heinz et al. [127], the integrated PL intensities of localized excitons, trions/excitons and biexcitons grow sublinearly, linearly and quadratically respectively with the excitation power [78, 126, 127]. The integrated PL intensity of the low energy peak at ~710 nm from the monolayer at 83K grew linearly with the excitation power (α=1.05, Figure 4.12a), indicating that this was a trion peak, not a localized exciton or bi-exciton peak. Moreover, the high-energy peak at (~697 nm) was confirmed as an exciton

peak. Figure 4.12b shows the PL emission intensity under different excitation powers (60μW, 400 μW, 900 μW).

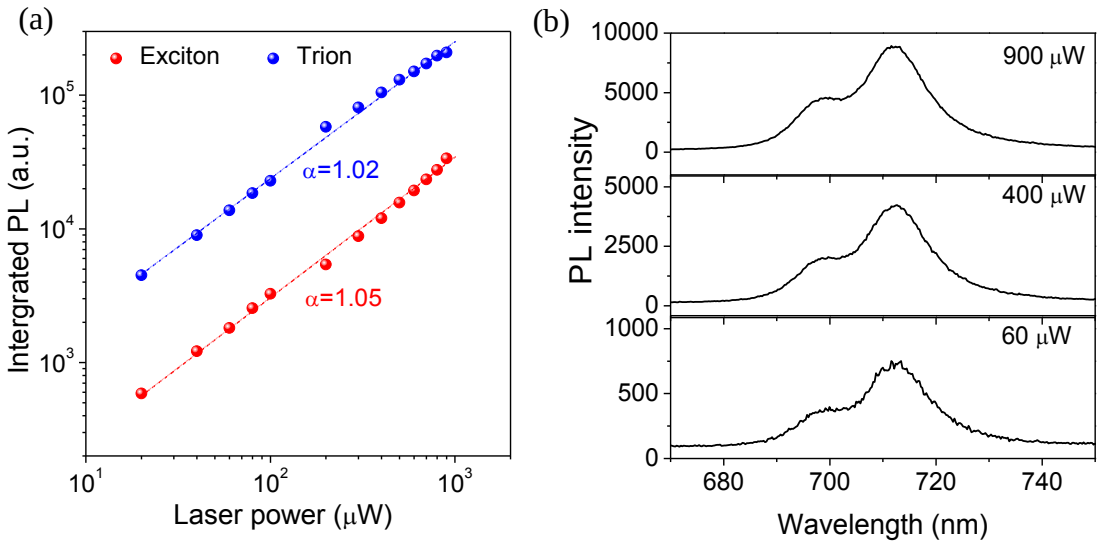

Figure 4.12 **Power dependence of exciton and trion emission in 1L $MoS_{2x}Se_{2(1-x)}$ (x=0.45). (a)** The experimental results and linear fit for integrated PL versus laser power under double logarithmic scale. The slopes of the linearly fitted lines are 1.02 for exciton and 1.05 for trion. **(b)** PL emission intensity under different excitation powers (60μW, 400 μW, 900 μW).

4.2.3 Trion binding energy in 1L $MoS_{2x}Se_{2(1-x)}$ (x=0.45)

To further identify exciton and trion transition dynamics, the extracted exciton (red) and trion (blue) peak intensities as functions of back-gate voltage are shown in Figure 4.13a. Notably, the negative trion peak is at its minimum at -70 V, gradually rises with the increase of positive back-gate voltage amplitude, and saturates when the sample is negatively doped under high voltage bias V_g (*i.e.* 30V); the exciton peak intensity displays

an opposite trend, that is, it drops from its maximum at -70V all the way down to around one-third when V_g = 70 V.

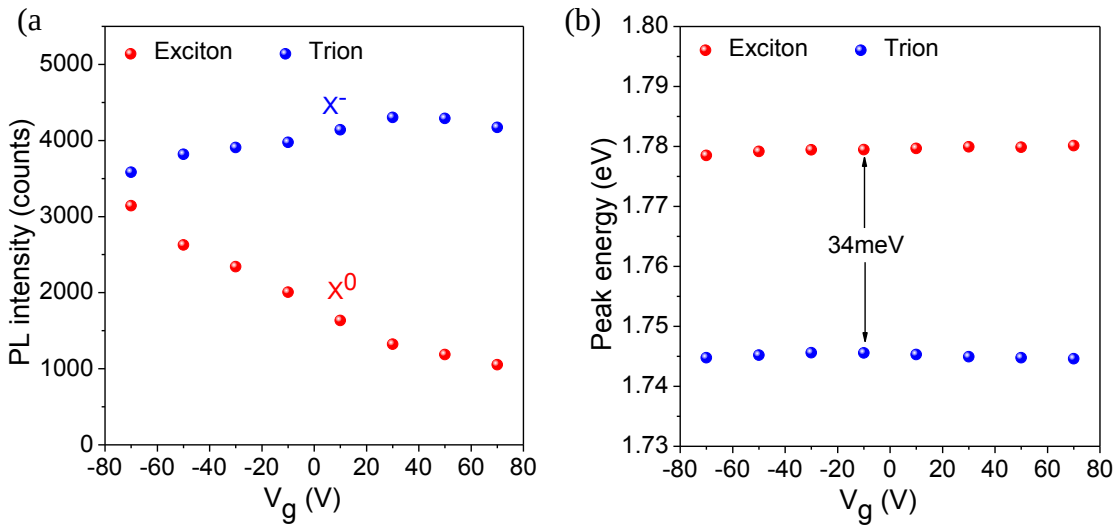

Figure 4.13 **Exciton and trion analysis of 1L $MoS_{2x}Se_{2(1-x)}$. (a)** Exciton and trion peak intensities under different back-gate voltages at 83 K. **(b)** Exciton and trion peak energies under different back-gate voltages at 83 K. The binding energies of positive trion and negative trion are measured as ~24 and ~27 meV, respectively.

Figure 4.13b presents exciton and trion peak energies from the fitting curves. It reveals that the binding energy of the negative trion (the peak energy difference of exciton and negative trion) is around 34 meV under back-gate voltages ranging from -70V to 70V. The same electrical modulation at a higher temperature (113 K) was also measured. Similar external gate modulation effects for excitons and negative trions are also evident (Figure 4.14), even though the trion peaks at 113K are much weaker than those measured at 83K. In the experiments, the low-energy emission peak at ~710 nm had the opposite doping dependence to that of the high-energy emission peak, which was consistent with the unique behaviour of trions [32].

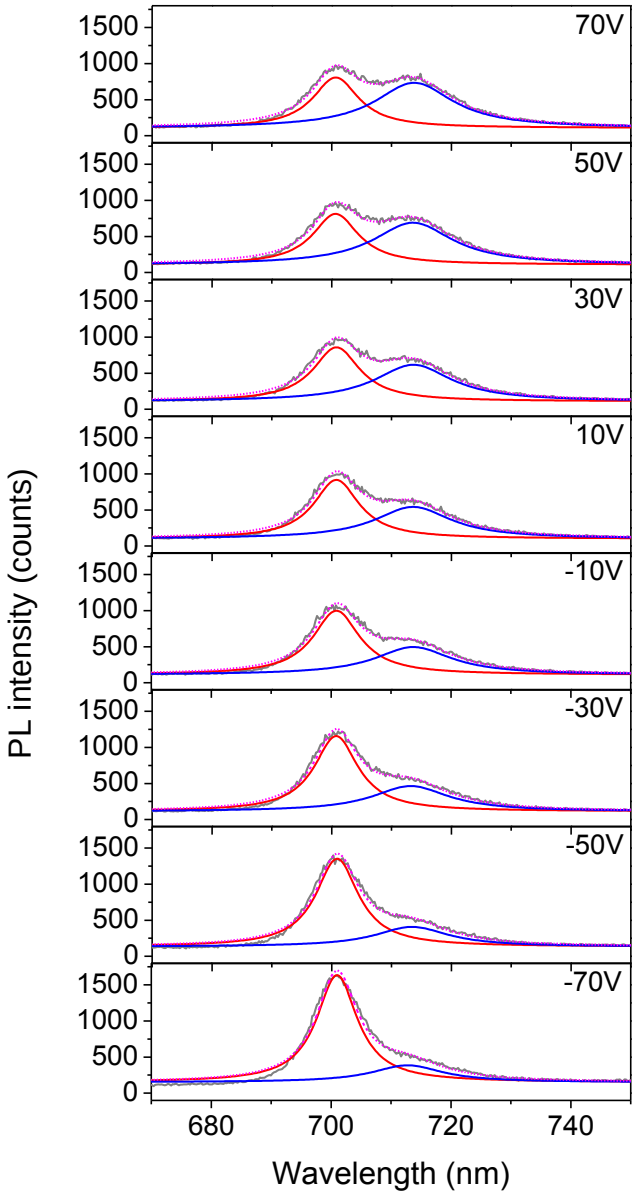

Figure 4.14 **PL spectra of monolayer $MoS_{2x}Se_{2(1-x)}$ sample at 113 K with back-gate voltage from -70 to 70 V**

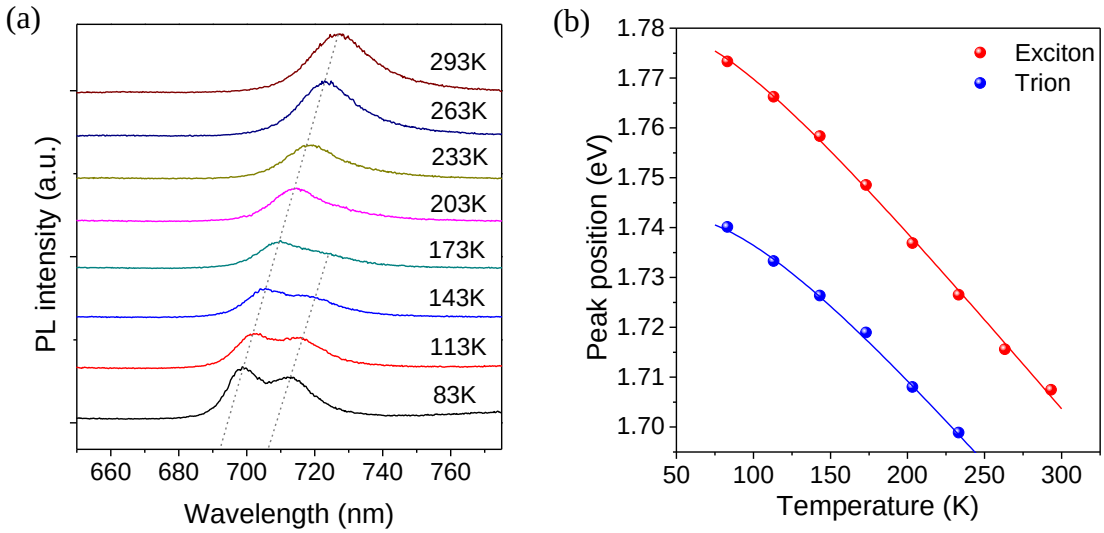

Figure 4.15 **Temperature dependence of PL intensity from the monolayer $MoS_{2x}Se_{2(1-x)}$ sample (a)** measured PL spectra of the 1L $MoS_{2x}Se_{2(1-x)}$ under various temperatures. **(b)** PL peak energy as a function of temperature. All the peaks are fitted to Lorentzians by multi-peak fitting. The solid lines are the curves fitted by a standard semiconductor bandgap dependence of $E_g(T) = E_g(0)$-Sħω[coth(ħω/2kT)-1], where $E_g(0)$ is the ground-state transition energy at 0 K, S is a dimensionless coupling constant and ħω is an average phonon energy.

4.3 Quasi-1D exciton in phosphorene

Dimensional confinement is the dominating factor that determines the binding energy of trions. In quasi-2D quantum wells, the trion binding energy is only 1-5 meV and trions are highly unstable, except at cryogenic temperatures [103, 137]. In 2013, Shan [32] and Xu [129] made important breakthroughs, showing that truly 2D atomic TMD semiconductors had trion binding energy up to 20-30 meV, which is still barely resolvable at room temperature compared with their emission bandwidth. On the other hand, trions

in the 1D space, such as carbon nanotubes, exhibit remarkably higher binding energies in the range of 100–200 meV owing to the stronger Coulomb interaction with the reduced dimensionality and screening [130]. Complete separation of the exciton and trion emission peaks was observed at room temperature [130].

However, application of 1D carbon nanotubes [138-143] in practical optoelectronic devices is intrinsically limited by their small cross-sections. The overall optical responses of such 1D lines are extremely weak. The diverse distribution of the chirality in carbon nanotubes also makes it impossible to assemble a large film with uniform optoelectronic responses. Although the reduced dimensionality leads to far more attractive exciton and trion properties, the trade-off between the cross-section and the dimensional confinement has hindered the development of useful excitonic optoelectronic devices.

From the excitons and trions dynamics study in 3L phosphorene and 1L $MoS_{2x}Se_{2(1-x)}$ (x=0.45) (reported in Chapter 4.1 and 4.2 respectively), the huge trion binding energy difference between the two 2D materials was clearly demonstrated. For 1L $MoS_{2x}Se_{2(1-x)}$ (x=0.45), the trion binding energy at ~34 meV was almost within the trion binding range for 2D materials. However, the trion binding energy of 162 meV in 2D material 3L phosphorene was within the trion binding energy range for a 1D material. To better understand the trion physics in 3L phosphorene, further experimental and theoretical investigations were conducted.

4.3.1 Polarization dependence of PL excitation and emission

The ultra-high trion binding energy measured in few-layer phosphorene is caused by the material's unique anisotropic quasi-1D excitonic nature, which can be measured using linearly polarized emission, as theoretically predicted by Yang et al. [144]. Now, the quasi-1D nature of the excitons and trions in few-layer phosphorene is demonstrated using PL measurements with an angle-resolved excitation and emission. Here, it is shown

that the PL emissions are completely linearly polarized along the armchair direction of the crystal.

In the setup of the angle-resolved PL measurement (Figure 4.16a), a linearly polarized Nd:YAG laser with a wavelength of 532 nm was used as the excitation source. The polarization angle of the incident light (θ_1) was controlled by an angle-variable half-wave plate. The polarization angle of the emission (θ_2) was characterized by inserting an angle-variable polarizer in front of the detector. θ_1 and θ_2 are relative to the same zero-degree reference, which could be arbitrarily selected initially.

From polarization-dependent PL excitation it was possible to determine the crystalline orientation of the phosphorene flake, and then the zigzag direction was selected as the shared zero-degree reference for θ1 and θ2 (Figure 4.16b).

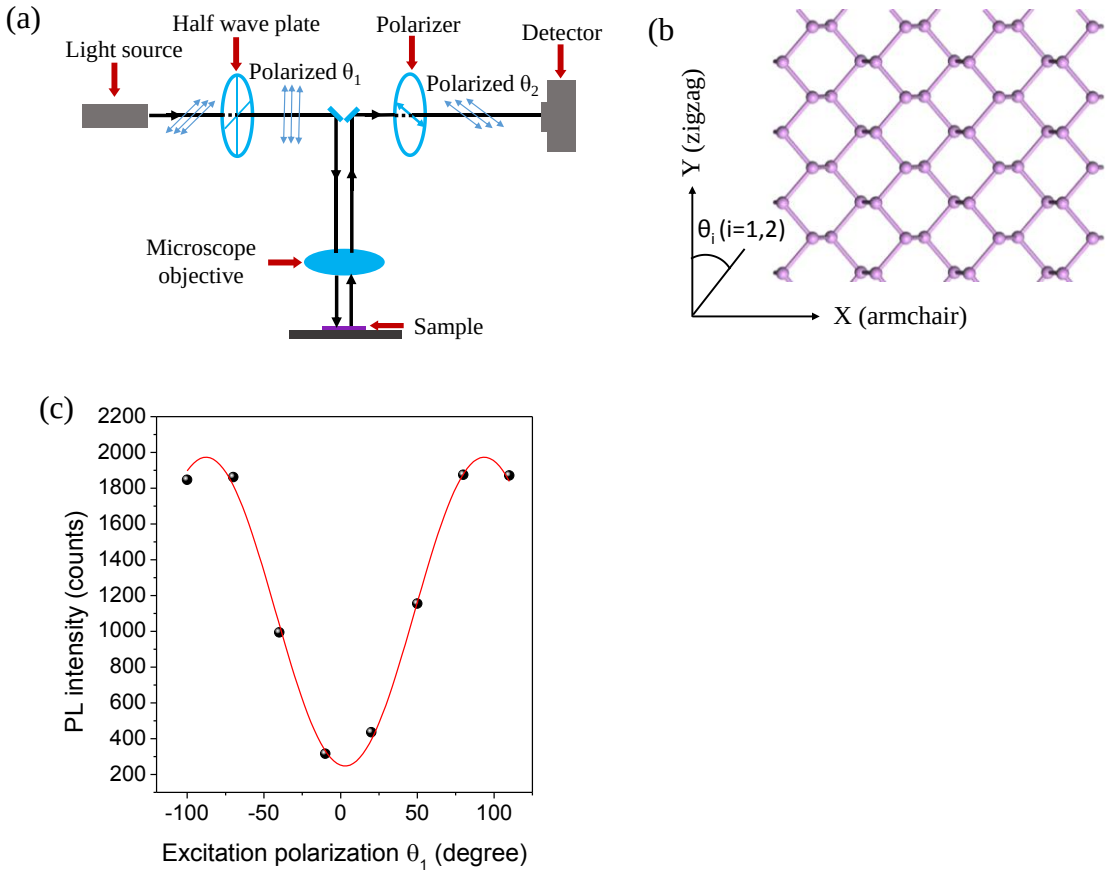

Figure 4.16 **Quasi-1D trions in phosphorene. (a)** Schematic plot of setup for measurement to characterize the polarization dependence of PL excitation and emission. The polarization angle (θ_1) incident excitation light is controlled by an angle-variable half-wave plate, and the polarization angle (θ_2) of the PL emission is characterized by inserting an angle-variable polarizer in front of the detector. **(b)** Schematic plot showing top view of phosphorene lattice structure and coordinates for polarization angles θ_1 and θ_2. **(c)** Measured excitation polarization dependence of the trion emission (~1300 nm) peak intensities from a 3L phosphorene on the SiO_2/Si substrate. Red lines in c are the fitting curves. For this measurement the polarizer in front of the detector was removed.

In the first characterization of the PL excitation polarization dependence, only the half-wave plate was used, and the polarizer in front of the detector was removed. It was found

that the PL intensity depended strongly on the excitation polarization angle θ_I (Figure 4.16c, Figure 4.17). This strong PL excitation polarization dependence was due to the highly anisotropic optical absorption in the phosphorene [144]. Because of the symmetry in its band structure and the optical selection rules [58, 145, 146], 3L phosphorene strongly absorbed armchair-polarized light and was transparent to zigzag-polarized light with energy between 0.5 and 2.8 eV [144].

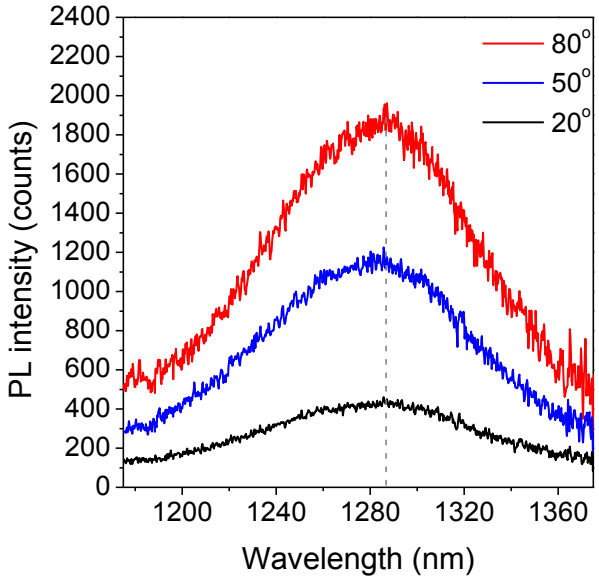

Figure 4.17 **PL spectra from a 3L phosphorene sample at different excitation polarization angles (20°, 50° and 80°)**

Because of the band symmetry and the optical selection rules in phosphorene [58, 145, 146], it strongly absorbed armchair-polarized light and was transparent to zigzag-polarized light. However, the bandgap energy of phosphorene was not sensitive to polarization angle. Therefore, there was no PL peak shift with the change of polarization angle, which was confirmed both by reported simulations [144] and by our experimental results, as shown in Figure 4.17.

Next, the polarization of the PL emission was measured by fixing the excitation polarization angle θ_1 at 95°. The maximum PL intensity was observed at $\theta_2 = 90°$ and the minimum PL intensity at $\theta_2 = 0°$ (Figure 4.18a, b). From Figure 4.18, it is evident that the PL emissions from both trions (~1300 nm) and excitons (~1100 nm) in the 3L phosphorene are completely linearly polarized along the armchair direction. The measured linear dichroism (LD) values for the PL emissions are all close to unity in few-layer phosphorene samples (Figure 4.18a, b). LD is defined as $LD = (I_x - I_y)/I_x$, where I_x and I_y are the PL emission peak intensities along the armchair and zigzag directions, respectively. The polarization of the PL emission was independent of the excitation and was determined by the intrinsic properties of phosphorene [145].

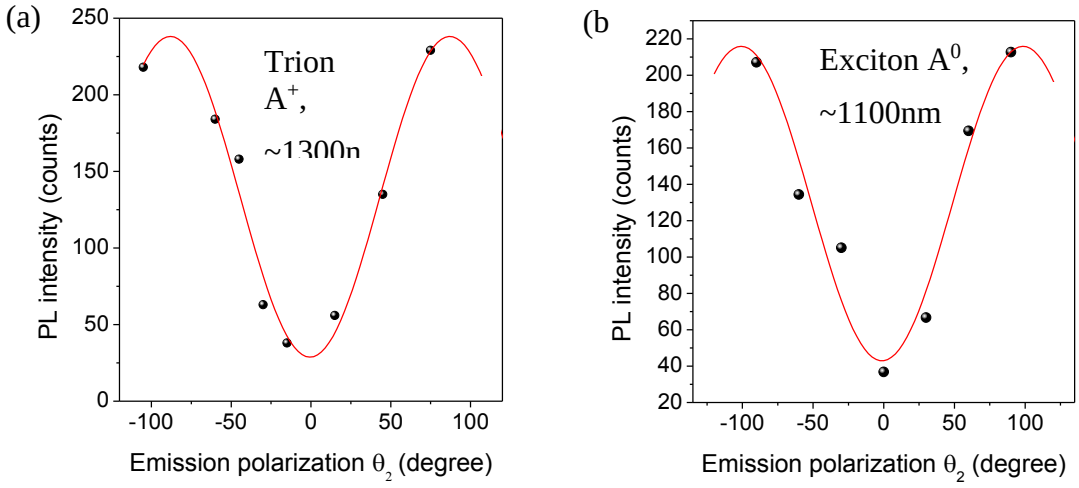

Figure 4.18 **Measured polarization dependence of trion (A^+) emission at ~1300nm (a) and exciton (A^0) emission at ~1100nm (b)**, measured from the same 3L phosphorene sample as in Figure 4.16 on SiO_2/Si substrate, with excitation angle of 95°. Red lines in a and b are the fitting curves.

The anisotropic nature of new 2D material phosphorene [53, 56-60, 64, 121, 144, 147] in contrast to other 2D materials such as graphene [22, 148, 149] and TMD semiconductors [32, 36, 39, 40, 58, 129] allows excitons to be confined in a quasi-one-dimensional (quasi-1D) space predicted in theory [58, 144] leading to remarkable phenomena arising from the reduced dimensionality and screening.

The quasi-1D excitons and trions in phosphorene were demonstrated by measured linearly polarized PL emission from the excitons and trions. In this regard, phosphorene was equivalent to a system made up of a bundle of identical 1D materials. The measured layer-dependent trion binding energies in the few-layer phosphorene agreed well with the theoretical calculations. These results open exciting avenues for optoelectronic applications, including tunable light sources [119, 150], spin manipulation devices [118, 151] and quantum logical systems [120, 152].

4.3.2 Trion effective dimension calculation

Theoretical calculation is very important for better understanding of the extraordinary trion binding energy (as high as ~162 meV) of 3L phosphorene.

Exciton and trion binding energies have been calculated using many different well-developed approaches, such as the diffusion Monte Carlo technique [153, 154], the boundary-matching-matrix method [155] and the hyperspherical approach [156, 157]. However, those methods were mainly applicable for 2D TMD semiconductors and quasi-2D GaAs quantum wells [153-157]. Attempts made to implement those approaches for 3L phosphorene yielded the trion binding energy of 50−70 meV [153-157], which was lower than the value measured in the present experiments. This difference was primarily caused by the excitons and trions in phosphorene being confined to a quasi-1D space, which was demonstrated by the angle-resolved PL measurements on 3L phosphorene samples. Here, the quasi-1D trion binding energy was calculated using a variational

quantum Monte Carlo method because this approach had been demonstrated to work well for both quasi-1D trions from carbon nanotubes and quasi- 2D trions from GaAs quantum wells [34, 127, 130, 158, 159]. The binding energies of excitons (E_E) and trions (E_T) was estimated using the equation [160]:

$$E_E = \frac{4}{(D_E - 1)^2} \times R_y^*$$

$$E_T = \left(-\frac{4}{(D_E - 1)^2} - c_0 - \sum_{i=1}^{4} c_i \, D_T^{-i} e^{-D_T} \right) \times R_y^* \quad (4.3)$$

where D_E is the effective dimension of excitons, D_T is the effective dimension of trions, R_y^* is the effective Rydberg unit of energy, and $c_{i,j=1-4}$ are the coefficients [160] given in Table 4.1

Table 4.1 Parameters used for the calculation of trion binding energy in 3L phosphorene

Parameter	Value
C_0	-0.42 [160]
C_1	158 [160]
C_2	-1330 [160]
C_3	3113 [160]
C_4	-2640 [160]
μ	0.67 [161]
ε	3.4 [162]

where μ is reduced mass and ε is dielectric constant.

The effective dimension of a trion is expected to be slightly smaller than that of an exciton because of the extra charge in the trion [160]. For calculation and analysis convenience, [160] the equation can be simplified by taking D = D_E = D_T.

$$E_E = \frac{4}{(D-1)^2} \times R_y^*$$

$$E_T = \left(-\frac{4}{(D-1)^2} - c_0 - \sum_{i=1}^{4} c_i \, D^{-i} e^{-D} \right) \times R_y^* \qquad (4.4)$$

The calculated trion binding using the simplified Equation 4.4 is expected to be slightly smaller than that from the original Equation 4.3. On the basis of 4.4, the trion and exciton binding energies were calculated as a function of the effective dimension D in 3L phosphorene (Figure 4.19).

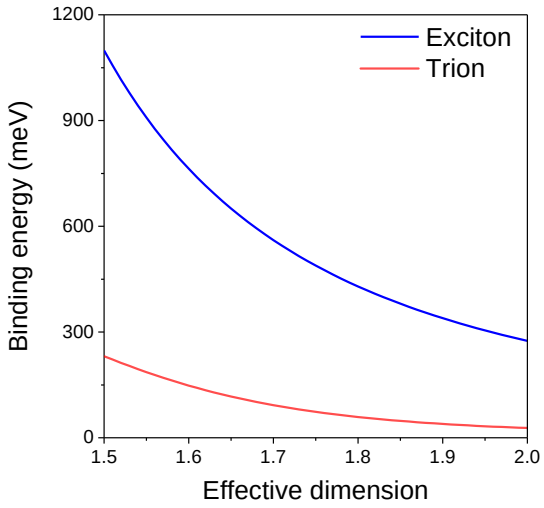

Figure 4.19 **Trion and exciton binding energy versus effective dimension in 3L phosphorene**

Using the measured trion binding energy value of ~162 meV in 3L phosphorene, the effective dimension of trions in 3L phosphorene was estimated to be D~ 1.58, which further supports the quasi-1D nature of trions as demonstrated earlier.

Based on previous theoretical calculations, the trion binding energies of TMD materials were 10−15% of their exciton binding energies[153-157], and this result was confirmed by experimental measurements in TMD semiconductors [32, 39, 129]. On the basis of Tran's simulation [144], the exciton binding energy of monolayer phosphorene (~0.9 eV) was greater than the exciton binding energies of all reported TMD monolayers [34, 153-158], because of the quasi-1D exciton nature of phosphorene [144]. More importantly, from Equation 4.4 and Figure 4.19, the binding energies of excitons and trions increased with the decrease in the effective dimensionality of the excitons and trions in the materials. That is the main reason that trions in 1D space, such as carbon nanotubes, have remarkably higher binding energies in the range of ~200 meV.

Here, it became clear that phosphorene presented an intriguing platform to overcome the aforementioned trade-off. Quasi-1D trions with ultra-high binding energies up to ~162 meV were observed in 2D phosphorene atomic semiconductors. Using back-gated MOS devices, it was possible to demonstrate the reversible electrostatic tunability of the exciton charging effects between trions and excitons in 3L phosphorene. The measured ultra-high trion binding energies (~162 meV), comparable to those in truly 1D semiconductors [130], were attributable to the formation of quasi-1D trions and excitons in 2D phosphorene.

4.4 Summary

In conclusion, extraordinarily bound quasi-1D trions were observed in 2D phosphorene atomic semiconductor crystals. The measured ultra-high trion binding energies in few-layer phosphorene were approximately one order of magnitude higher than those in 2D TMD semiconductors. The large trion binding energy was attributed to the strongly confined 1D excitonic nature in few-layer phosphorene, which was demonstrated by measured linearly polarized PL emission. Phosphorene possesses both a large optical cross-section (as typically exhibited by a 2D material system) and high trion binding

energies (as typically exhibited by a 1D system), allowing remarkable optoelectronic applications including tunable light sources, photo-detectors and spin manipulation devices. In addition, the measured layer-dependent trion binding energies in few-layer phosphorene were consistent with the theoretical calculations performed, and will enable the development of a wide range of tunable energy gaps and corresponding optoelectronic applications. Few-layer phosphorene can also serve as a room-temperature platform for investigating many-body interactions and excitonic physics.

Chapter 5 Elastic light-matter interactions

This chapter presents research results for elastic light-matter interactions in phosphorene, and consists of two parts: an OPL study of layer-dependent phosphorene and a phosphorene-based micro-lens study.

PSI was used to measure the OPL of few-layer phosphorene. The giant OPL in few-layer phosphorene on one hand implies the strong elastic light-matter interactions in phosphorene; on the other hand, it provides an accurate and fast method for identifying the number of layers in phosphorene.

The conventional way of identifying the number of layers is by measuring physical thickness using AFM. However, few-layer phosphorene samples degrade (react with oxygen and water) very quickly during physical thickness measurements. Fortunately, OPL study provided an alternative way to tackle the degradation problem. Based on the measurements of physical thickness and OPL from tens of few-layer phosphorene samples, the linear relationship between OPL and number of layers of phosphorene was established. In one-layer phosphorene the physical thickness was below 1nm (via AFM), while its OPL was around 20nm (the instrumental error from PSI being around 2nm), making the method very accurate in identifying the number of layers. Moreover, the measurement by PSI took only around 5 minutes, while measurement by AFM normally takes around 20 minutes. Therefore, the number of layers of phosphorene could be accurately and quickly measured via PSI, effectively limiting the degradation.

5.1 Optical path length

5.1.1 Phase-shifting interferometry (PSI) working principle[163]

PSI was used to investigate the surface topography based on analysing the digitized interference data obtained during a well-controlled phase shift introduced by the Mirau interferometer [83]. The PSI system (Vecco NT9100) used in the experiments operates with a green LED source centred near 535 nm by a 10 nm band-pass filter [79, 163].

The working principle of the PSI system is as follows [164]. For simplicity, a wavefront phase is used for analysis. The expressions for the reference and test wave-fronts in the phase-shifting interferometer are:

$$w_r(x,y) = a_r(x,y)e^{i\phi_r(x,y)} \tag{5.1}$$

$$w_t(x,y,t) = a_t(x,y)e^{i[\phi_t(x,y)+\delta(t)]} \tag{5.2}$$

where $a_r(x,y)$ and $a_t(x,y)$ are the wavefront amplitudes, $\phi_r(x,y)$ and $\phi_t(x,y)$ are the corresponding wavefront phases, and $\delta(t)$ is a time-dependent phase shift introduced by the Mirau interferometer. $\delta(t)$ is the relative phase shift between the reference beam and the test beam.

The interference pattern of these two beams is:

$$w_i(x,y,t) = a_r(x,y)e^{i\phi_r(x,y)} + a_t(x,y)e^{i[\phi_t(x,y)+\delta(t)]} \tag{5.3}$$

The interference intensity pattern detected by the detector is:

$$\boldsymbol{I}_i(x,y,t) = w_i^*(x,y,t) * w_i(x,y,t) = \boldsymbol{I}'(x,y) + \boldsymbol{I}''(x,y)\cos[\phi(x,y) + \delta(t)] \tag{5.4}$$

where $\boldsymbol{I}'(x,y) = a_r^2(x,y) + a_t^2(x,y)$ is the averaged intensity, $\boldsymbol{I}''(x,y) = 2a_r(x,y) * a_t(x,y)$ is known as intensity modulation and $\phi(x,y)$ is the wavefront phase shift $\phi_r(x,y) - \phi_t(x,y)$.

From Equation 5.4, the sinusoidally-varying intensity of the interferogram at a given measurement point as a function of $\delta(t)$ is shown as:

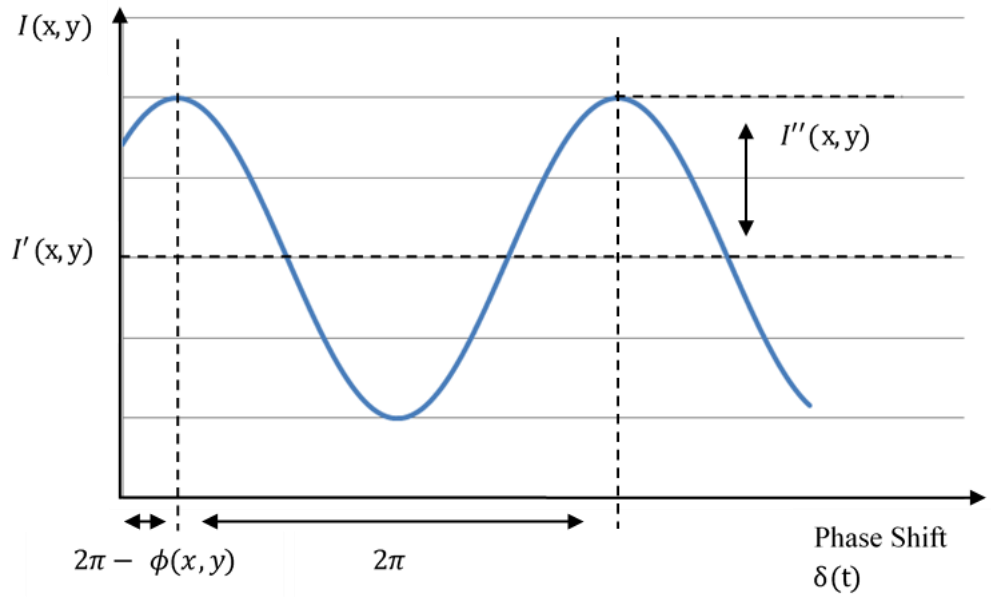

Figure 5.1 **Variation of intensity with the reference phase at a point in an interferogram.** $\boldsymbol{I'(x,y)}$ is the averaged intensity, $\boldsymbol{I''(x,y)}$ is half of the peak-to-valley intensity modulation and $\phi(x,y)$is the temporal phase shift of this sinusoidal variation.

$\delta(t)$ is introduced by the Mirau interferometer. As the Mirau interferometer moves gradually towards the sample platform, the OPL of the test beam decreases while the OPL of the reference beam remains invariant.

The PSI computational method is a four-step algorithm, which needs to acquire four separately recorded and digitalized interferograms of the measurement region. For each separate and sequentially recorded interferograms, the phase shift difference is:

$$\delta(t_i) = 0, \frac{\pi}{2}, \pi, \frac{3\pi}{2}; \;\; i = 1,2,3,4 \tag{5.5}$$

Substitution of the four values into Equation 5.4 leads to the following four equations describing the four measured intensity patterns of the interferogram:

$$\boldsymbol{I}_1(x,y) = \boldsymbol{I}'(x,y) + \boldsymbol{I}''(x,y)\cos[\phi(x,y)] \tag{5.6}$$

$$\boldsymbol{I}_2(x,y) = \boldsymbol{I}'(x,y) + \boldsymbol{I}''(x,y)\cos[\phi(x,y) + \tfrac{\pi}{2}] \tag{5.7}$$

$$\boldsymbol{I}_3(x,y) = \boldsymbol{I}'(x,y) + \boldsymbol{I}''(x,y)\cos[\phi(x,y) + \pi] \tag{5.8}$$

$$\boldsymbol{I}_4(x,y) = \boldsymbol{I}'(x,y) + \boldsymbol{I}''(x,y)\cos[\phi(x,y) + \tfrac{3\pi}{2}] \tag{5.9}$$

After the trigonometric identity, this yields:

$$\boldsymbol{I}_1(x,y) = \boldsymbol{I}'(x,y) + \boldsymbol{I}''(x,y)\cos[\phi(x,y)] \tag{5.10}$$

$$\boldsymbol{I}_2(x,y) = \boldsymbol{I}'(x,y) - \boldsymbol{I}''(x,y)\sin[\phi(x,y)] \tag{5.11}$$

$$\boldsymbol{I}_3(x,y) = \boldsymbol{I}'(x,y) - \boldsymbol{I}''(x,y)\cos[\phi(x,y)] \tag{5.12}$$

$$\boldsymbol{I}_4(x,y) = \boldsymbol{I}'(x,y) + \boldsymbol{I}''(x,y)\sin[\phi(x,y)] \tag{5.13}$$

The unknown variables $\boldsymbol{I}'(x,y)$, $\boldsymbol{I}''(x,y)$ and $\phi(x,y)$ can be solved by using only three of the four equations; but for computational convenience, four equations are used here. Subtracting Equation 5.11 from Equation 5.13 gives:

$$\boldsymbol{I}_4(x,y) - \boldsymbol{I}_2(x,y) = 2\boldsymbol{I}''(x,y)\sin[\phi(x,y)] \tag{5.14}$$

And subtracting Equation 5.12 from Equation 5.10 yields:

$$\boldsymbol{I}_1(x,y) - \boldsymbol{I}_3(x,y) = 2\boldsymbol{I}''(x,y)\cos[\phi(x,y)] \tag{5.15}$$

Taking the ratio of Equation 5.14 over Equation 5.15, the intensity modulation $\boldsymbol{I}''(x,y)$ is eliminated as:

$$\frac{\boldsymbol{I}_4(x,y) - \boldsymbol{I}_2(x,y)}{\boldsymbol{I}_1(x,y) - \boldsymbol{I}_3(x,y)} = \tan[\phi(x,y)] \tag{5.16}$$

Rearranging Equation 5.16 obtains the wavefront phase shift term $\phi(x,y)\ as$:

$$\phi(x,y) = \tan^{-1}\frac{\boldsymbol{I}_4(x,y)-\boldsymbol{I}_2(x,y)}{\boldsymbol{I}_1(x,y)-\boldsymbol{I}_3(x,y)} \tag{5.17}$$

This equation is performed at each measurement point to acquire a map of the measured wavefront. Also, in PSI, the phase shift is transferred to the surface height or the optical path difference (OPD):

$$h(x,y) = \frac{\lambda\phi(x,y)}{4\pi} \tag{5.18}$$

$$OPD(x,y) = \frac{\lambda\phi(x,y)}{2\pi} \tag{5.19}$$

Here, the OPL of the phosphorene flake OPL_{BP} is calculated as:

$$OPL_{BP} = -(OPD_{BP} - OPD_{SiO_2}) = -\frac{\lambda}{2\pi}(\phi_{\mathrm{BP}} - \phi_{SiO_2}) \tag{5.20}$$

where λ is the wavelength of the light source, ϕ_{BP} and ϕ_{SiO_2} are the measured phase shifts of the reflected light from the phosphorene flake and the SiO_2 substrate, respectively. In the experiments, ϕ_{SiO_2} was typically set to zero, as shown in Figure 5.8d, e.

5.1.2 Calculation of the OPL of few-layer phosphorene

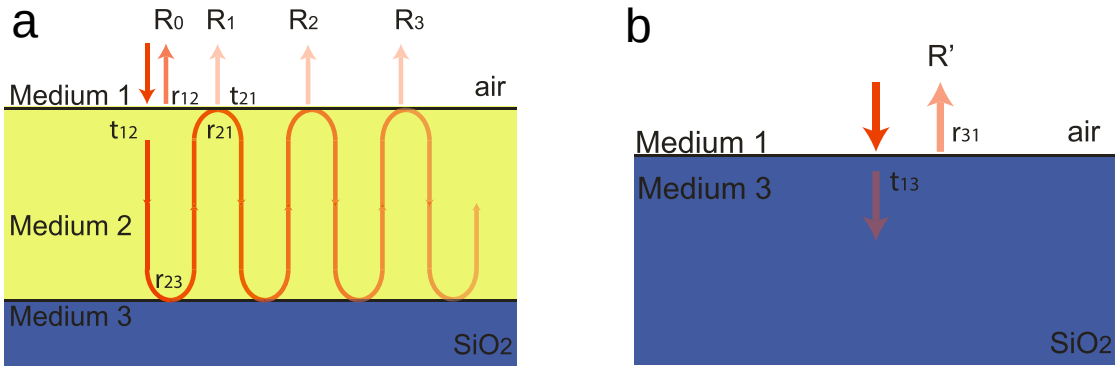

Figure 5.2 **(a)** Reflection of a three-layer structure. Medium 1 is air, Medium 2 is the 2D material and Medium 3 is an infinite SiO_2 substrate. **(b)** The reference configuration. Light is incident from air into the infinite SiO_2 substrate.

The incident light comes from the air resonance within the 2D material. The total reflection is determined by the interference of all reflected beams R_i. To calculate the amplitude of the total reflection, r_{ij} (i,j=1,2,3) is used to represent the reflection coefficients when the light travels from medium i to medium j.

$$r_{ij} = \frac{n_i - n_j}{n_i + n_j} \tag{5.21}$$

t_{ij} (i,j =1,2,3) is used to represent the transmission from medium i to medium j

$$t_{ij} = \frac{2n_i}{n_i + n_j} \tag{5.22}$$

where n_i, n_j (i,j =1,2,3) is the refractive index of medium i,j. Assuming that the thickness of the 2D material is d and the wave vector of incident light in air is k_0, it is possible to calculate the reflection of each order:

$$R_0 = r_{12}$$

$$R_1 = t_{12} r_{23} t_{21} e^{i2k_0 nd}$$

$$R_2 = t_{12}r_{23}r_{21}r_{23}t_{21}(e^{i2k_0nd})^2$$

$$R_3 = t_{12}r_{23}r_{21}r_{23}r_{21}r_{23}t_{21}(e^{i2k_0nd})^3 \tag{5.23}$$

where $2k_0nd$ is the round-trip propagation phase and n is the refractive index of the 2D material.

Then the total reflected amplitude is the summation of all reflections, which is

$$R = R_0 + R_1 + R_2 + \cdots$$

$$= r_{12} + t_{12}r_{23}t_{21}e^{i2k_0nd}\left[1 + r_{21}r_{23}e^{i2k_0nd} + \left(r_{21}r_{23}e^{i2k_0nd}\right)^2 + \cdots\right]$$

$$= r_{12} + \frac{t_{12}r_{23}t_{21}e^{i2k_0nd}}{1 - r_{21}r_{23}e^{i2k_0nd}}$$

$$= \frac{1-n}{1+n} + \frac{4n}{(1+n)^2}\frac{(n-1.46)}{(n+1.46)}e^{i2k_0nd}\frac{1}{1-\frac{(n-1)(n-1.46)}{(n+1)(n+1.46)}e^{i2k_0nd}} \tag{5.24}$$

Here the refractive indices of air and SiO_2 are assumed to be 1 and 1.46, respectively.

The OPL was calculated by comparing the phase difference of the reflected light with and without the 2D material. Figure 5.2b shows the reference setup. Light is incident directly into the infinite SiO_2 substrate from the air. In this case the reflected amplitude is

$$R' = \frac{n_1 - n_3}{n_1 + n_3} \tag{5.25}$$

So we get:

$$OPL = -\frac{\left(phase(R) - phase(R')\right)}{2\pi}\lambda \tag{5.26}$$

where λ is the wavelength of light. The magnitude of OPL is plotted in Figure 5.8d.

For phosphorene OPL calculations, the measured refractive index from bulk black phosphorus crystals (n = 3.4) is used [165-167].

5.1.3 Measurements of OPL in few-layer phosphorene

In this project, the challenge in working with unstable phosphorene is identification of the number of layers. AFM is typically unreliable for the identification of very-few-layer phosphorene (one or two layers) because of its slow scanning speed and the potential contact contamination.

Few-layer phosphorene flakes (Figure 5.3~Figure 5.8), were fabricated using mechanical exfoliation techniques onto a Si/SiO_2 chip substrate (275 nm SiO_2), similar to that used for graphene and MoS_2 [5, 8, 168]. The flakes were first identified by optical contrast in a microscope. Regions with different colours correspond to phosphorene flakes with different thickness. Figure 5.3a displays the optical microscope image of a typical thin phosphorene sample (2 layers, indicated by "2L") on a Si/SiO_2 substrate. The identification of the number of layers was confirmed by an AFM image of the sample shown in Figure 5.3b. More microscope and AFM images of the phosphorene flakes of different thicknesses are shown in Figure 5.3~Figure 5.7.

Here, a rapid, noninvasive and highly accurate approach is proposed and implemented to determine the number of layers, using optical interferometry. Specifically, the OPL of the light reflected from phosphorene was measured. The OPL was determined by $OPL_{BP} = -\frac{\lambda}{2\pi}(\phi_{BP} - \phi_{SiO_2})$, where $\lambda = 535\ nm$ is the wavelength of the light source, and ϕ_{BP} and ϕ_{SiO_2} are the phase shifts of the light reflected from the phosphorene flake and the SiO_2/Si substrate (Figure 5.8d inset), respectively. More PSI images and OPLs of the phosphorene flakes of different thicknesses are shown in Figure 5.4~Figure 5.7.

(a)

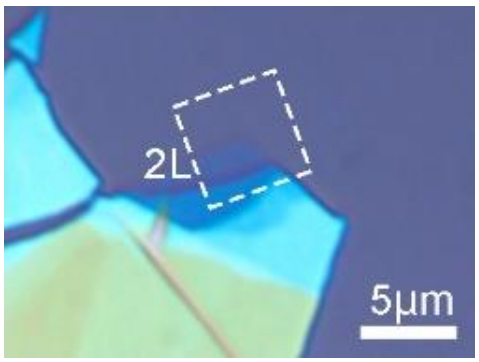

(b

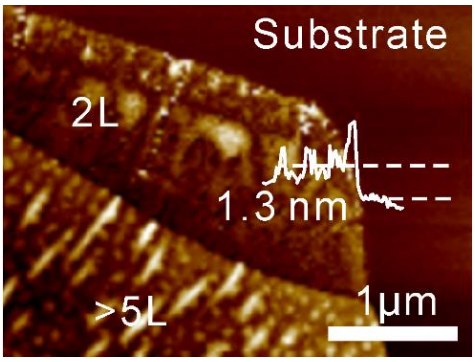

Figure 5.3 **Images and characterization of exfoliated phosphorene. (a)** Microscope image of 2L phosphorene. **(b)** AFM image of 2L phosphorene, with region indicated in the dashed line box in (a)

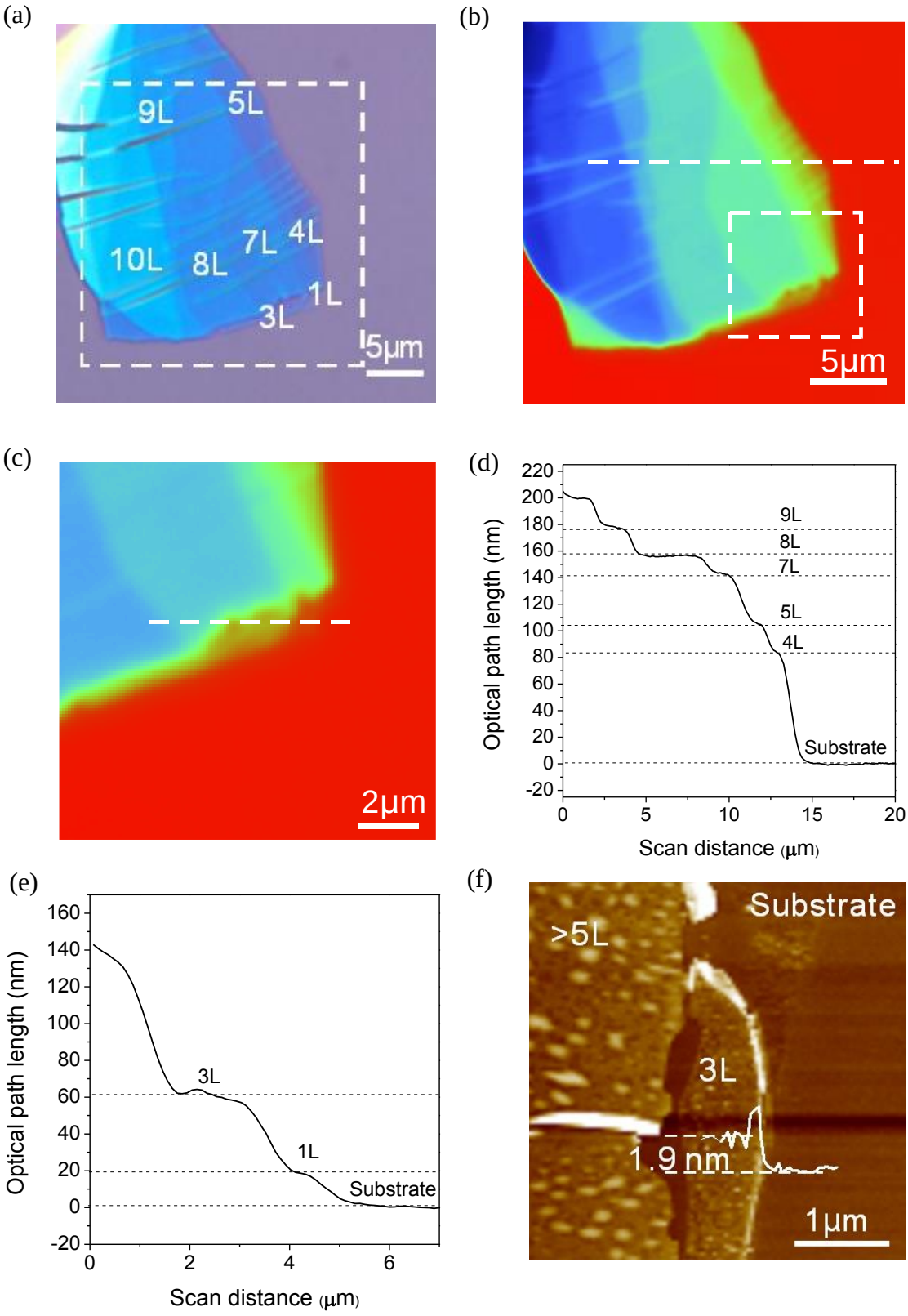

Figure 5.4 **Images and characterization of exfoliated phosphorene. (a)** Optical microscope image of a phosphorene flake containing multiple layers. **(b)** PSI image of the phosphorene flake from the dashed line box area indicated in (a). **(c)** PSI image of

the phosphorene flake from the dashed line box area indicated in (b). **(d)** and **(e)** display the OPL measured by PSI versus position along the dashed line in (b) and (c) respectively. **(f)** AFM image of the 3L phosphorene flake.

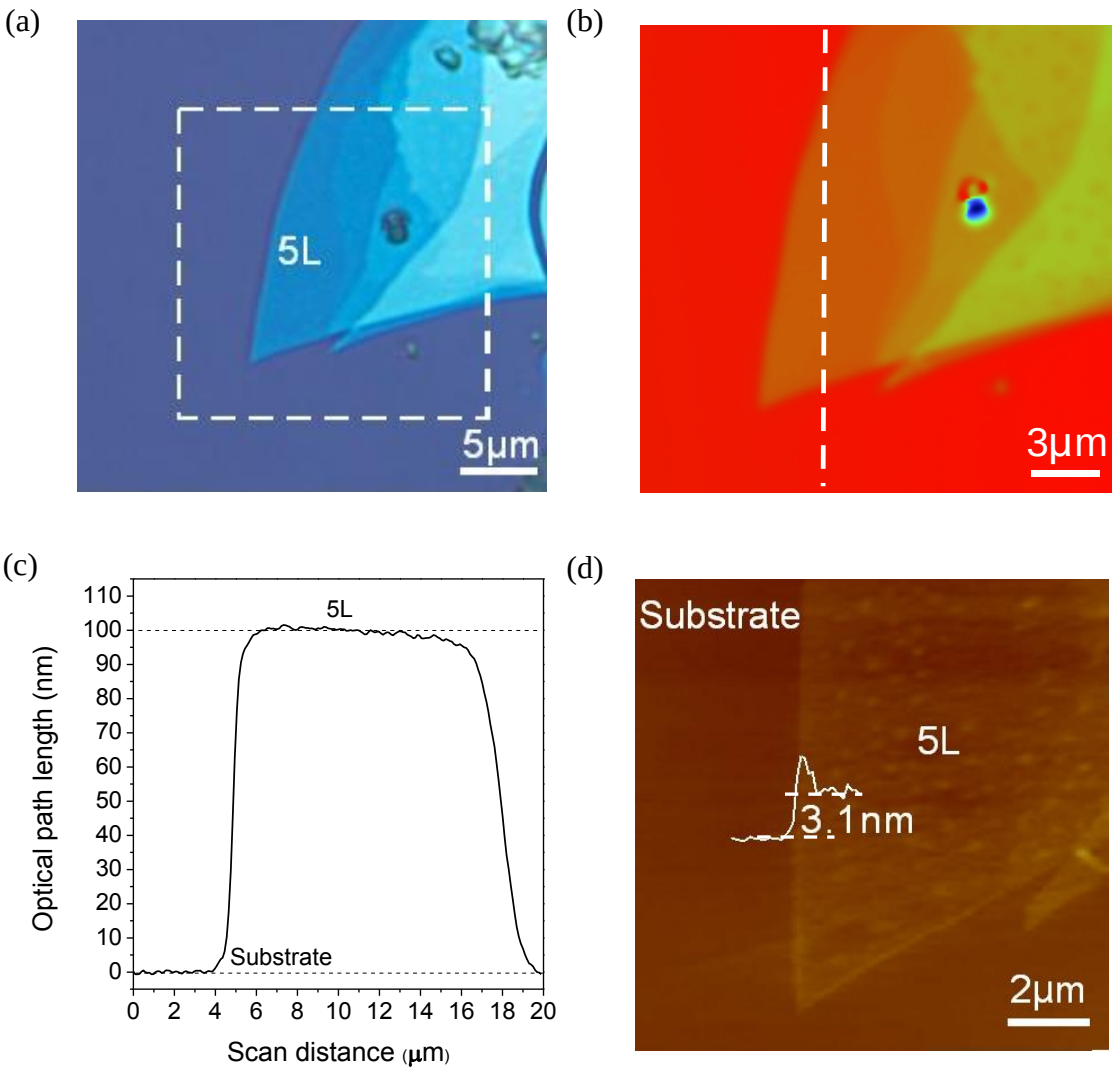

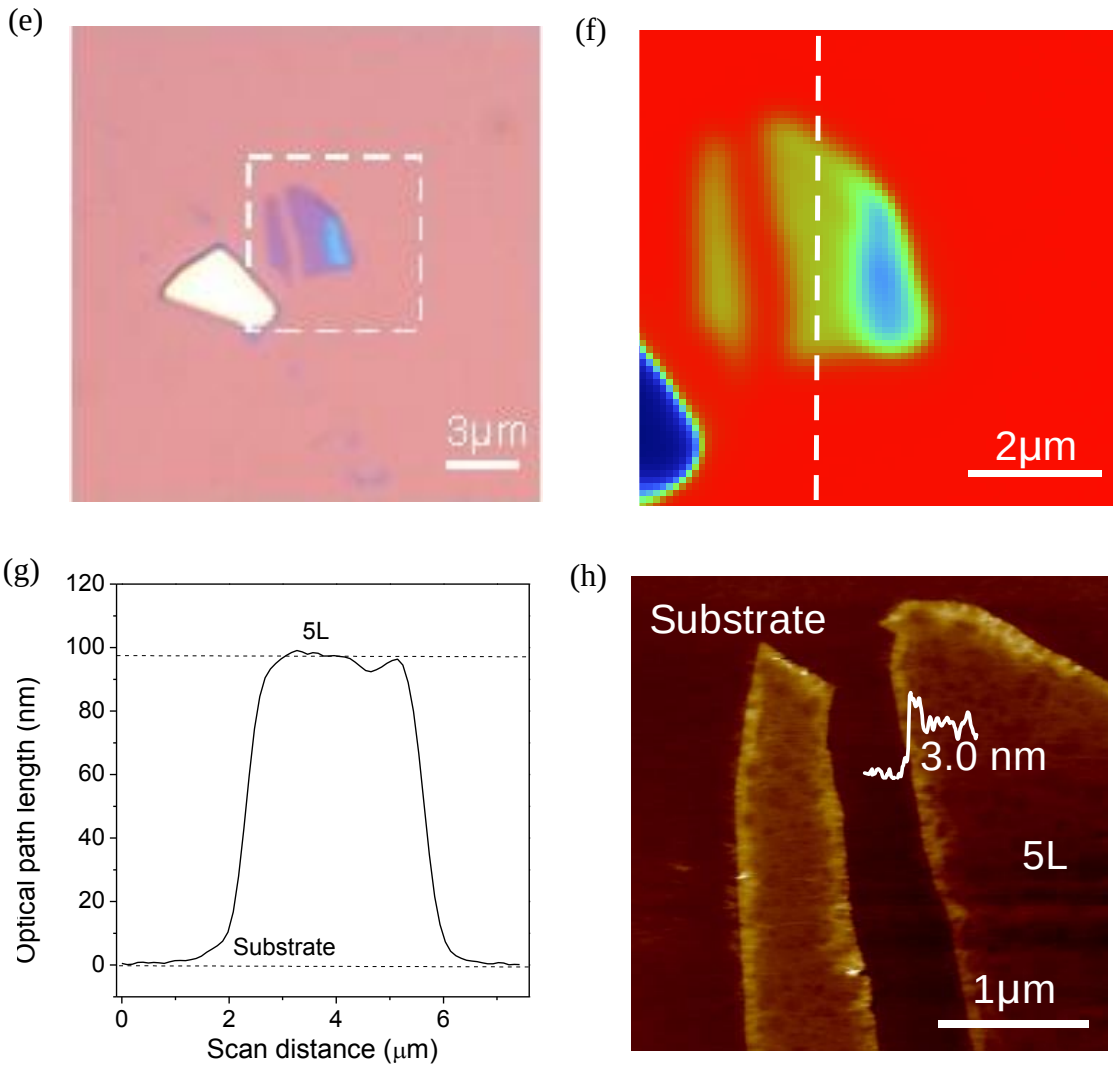

Figure 5.5 **Images and characterization of exfoliated 5L phosphorene. (a**) Optical microscope image of a 5L phosphorene flake. **(b)** PSI image of the 5L phosphorene from the dashed line box area indicated in (a). **(c)** OPL measured by PSI along the dashed line in (b). **(d)** AFM image of 5L phosphorene. **(e)**, **(f)**, **(g)** and **(h)** display optical microscope image, PSI image (from the dashed line box area indicated in e), OPL (along the dashed line in f) and AFM image of another 5L phosphorene flake, respectively.

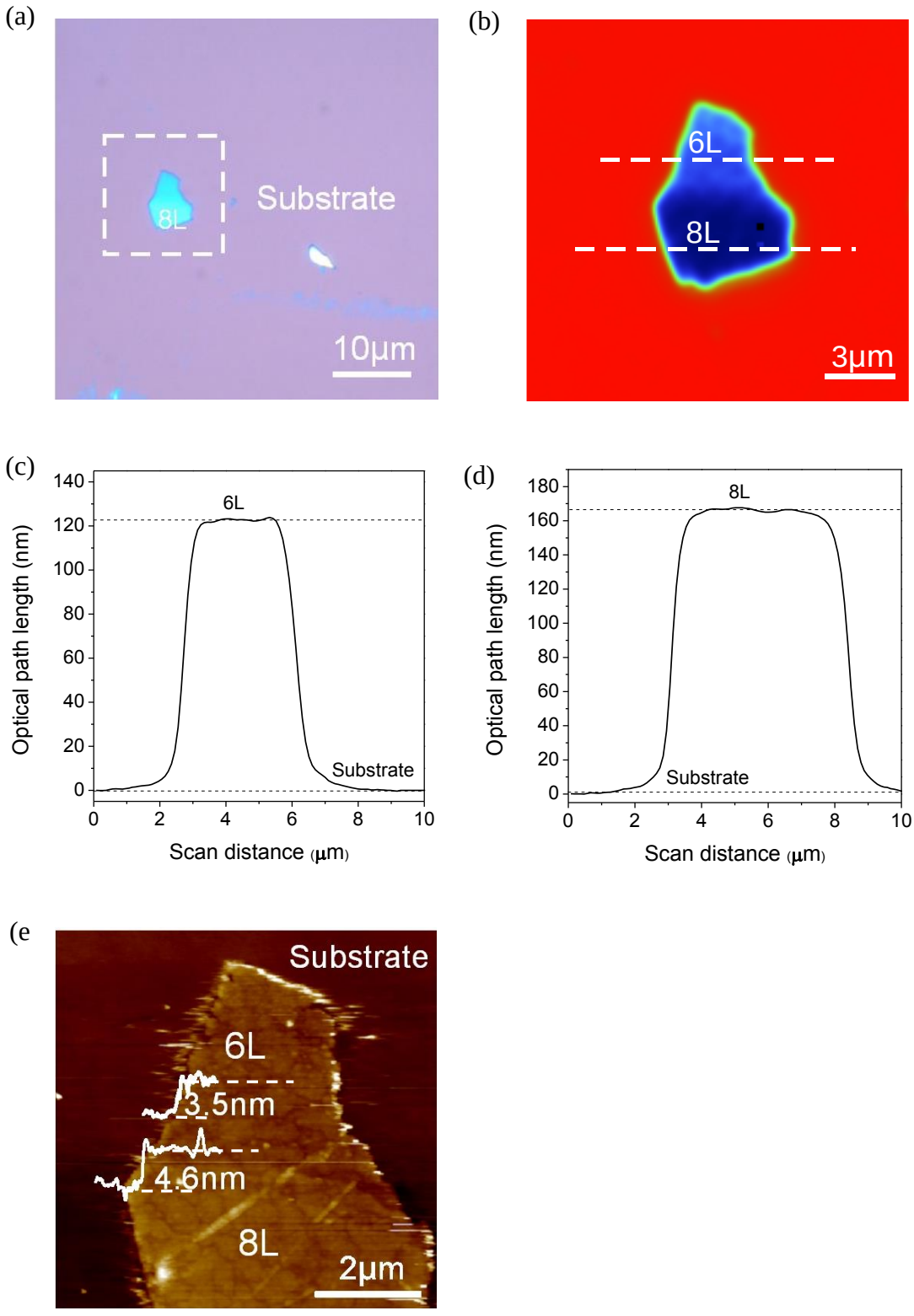

Figure 5.6 **Images and characterization of exfoliated 6L and 8L phosphorene flakes.** **(a)** Optical microscope image of a phosphorene flake containing 6L and 8L. **(b)** PSI image of the phosphorene flake from the dashed line box area indicated in (a). **(c)** and **(d)** display

OPL values measured by PSI from the 6L and 8L phosphorene along the dashed lines in (b). **(e)** AFM image of the 6L and 8L phosphorene.

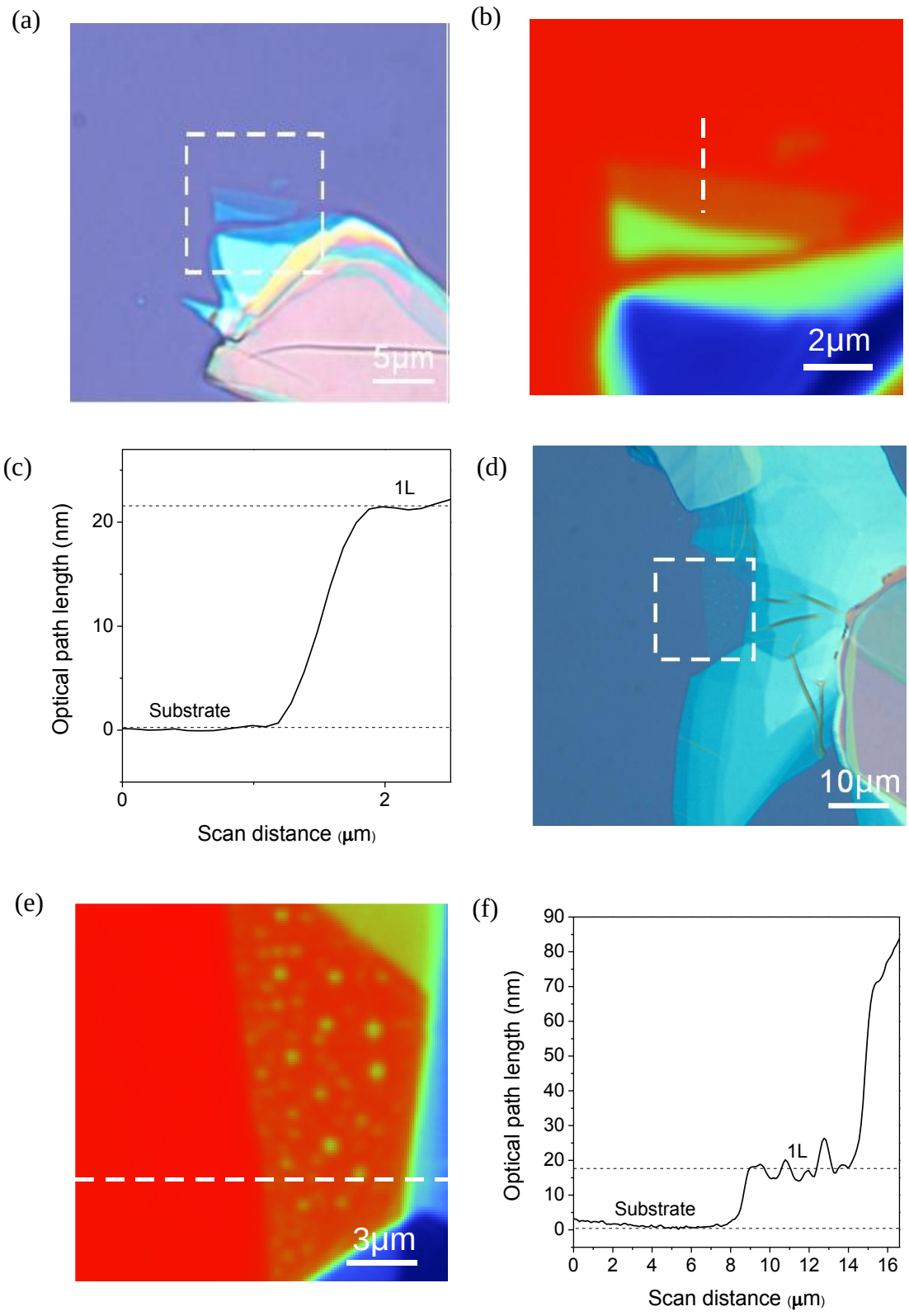

Figure 5.7 **Images of exfoliated 1L phosphorene flakes and their measured OPLs by PSI. (a)** Optical microscope image of a 1L phosphorene flake. **(b)** PSI image of the 1L

phosphorene flake from the dashed line box area indicated in (a). **(c)** OPL measured by PSI versus position along the dashed line in (b). **(d)**, **(e)** and **(f)** indicate the optical microscope image, PSI image (from the dashed line box in d) and OPL (along the dashed line in e) of another 1L flake, respectively.

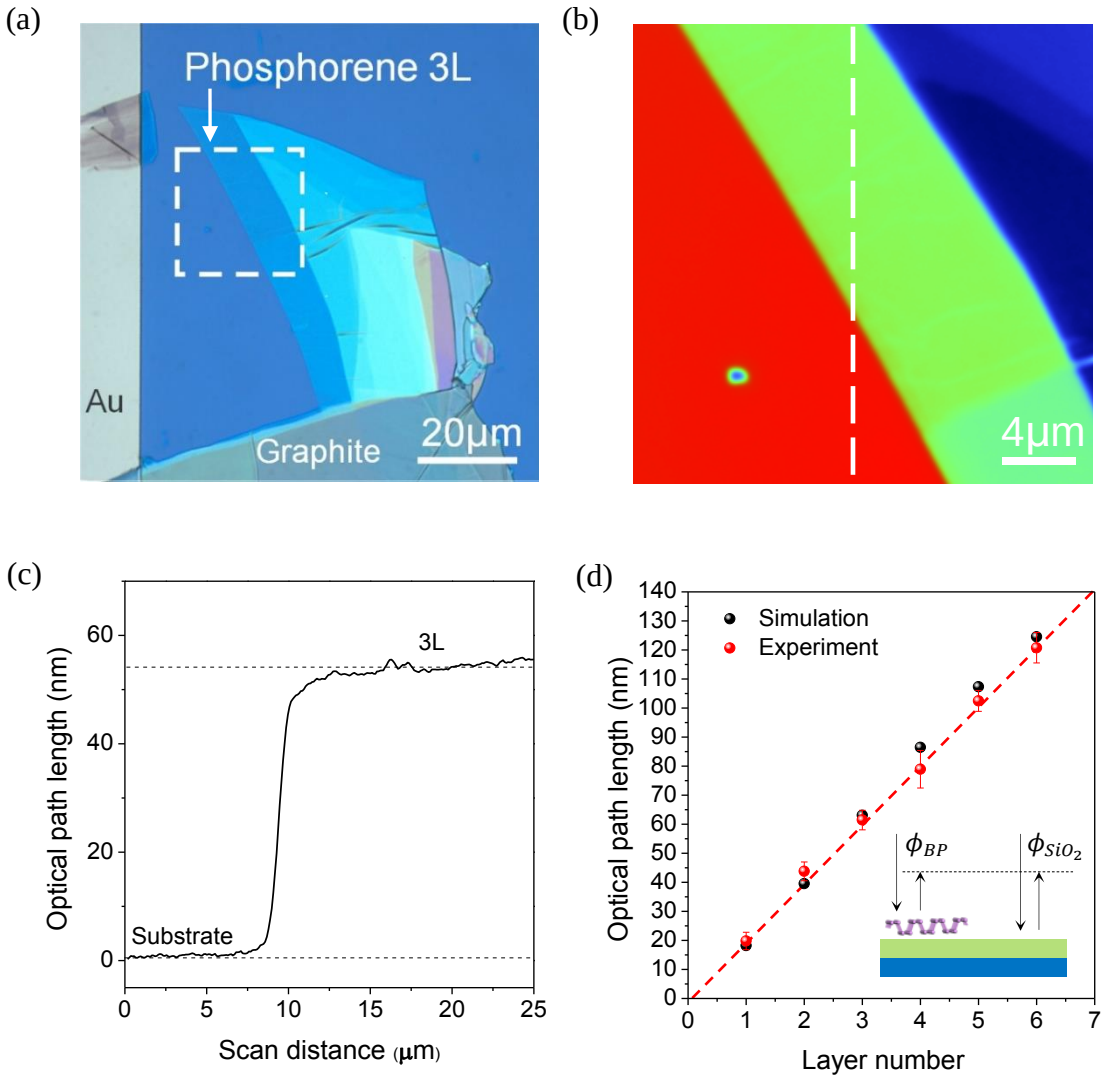

Figure 5.8 **Phosphorene characteristics and OPLs (a)** Optical microscope image of the MOS device with bi-layer phosphorene (labelled "3L"). **(b)** PSI image of the region inside the box indicated by the dashed line in (a). **(c)** PSI-measured OPL values versus position for 3L phosphorene along the dashed line in (b). **(d)** Statistical data of the OPL experimental values from PSI for 1–6L phosphorene samples. For each number of

phosphorene layers, at least three different samples were characterized for the statistical measurements. Theoretical simulation data is also plotted, for comparison. Inset: schematic plot indicating the PSI-measured phase shifts of the reflected light from the phosphorene flake (ϕ_{BP}) and the SiO2 substrate (ϕ_{SiO_2}).

The one-to-one relation between the OPL and the number of layers was firmly established by a first-principles optical calculation and experimental calibration, as shown in Figure 5.8d. Note that even though the thickness of one-layer phosphorene is less than 1 nm, its OPL is greater than 20 nm, owing to the multiple interfacial light reflections (Figure 5.2). That is, the virtual thickness of a phosphorene flake was amplified more than 20 times by the optical interferometry, allowing the flakes to be easily identified. Considering that the accuracy of the instrument was ~0.1 nm, a step change of 20 nm yielded a very robust measurement.

In the experiments, the number of layers of the phosphorene flake was first estimated according to its optical contrast in an optical microscope (Figure 5.8a) and then accurately identified by PSI (Figure 5.8b and c). After the PSI test, the sample was placed into a microscope-compatible chamber for PL measurements, with a slow flow of nitrogen gas to prevent degradation of the sample [121]. The layer-dependence of the PL emission also helped to verify the number of layers in few-layer phosphorene.

5.2 Micro-lens properties

The few-layer phosphorene was achieved by mechanical exfoliation (using 3M tape) from bulk black phosphorus single crystals (from Smart-elements) and then it was transferred onto a Si/SiO_2 substrate (275 nm thermal SiO_2). The few-layer phosphorene reacted with oxygen and water spontaneously in the air, forming bubbles that could be used as micro-

lenses. The few-layer phosphorene flakes and micro-lens were identified by optical microscope, after which characterization of the OPL and geometry data (thickness and diameter) was conducted by PSI (Vecco NT9100) and AFM respectively.

For the phosphorene-based micro-lens optical focal length study, a far-field scanning optical microscopy (SOM) system was built on the base of the micro-Raman system. In the SOM system, green laser at 532nm was applied and focused on the focal plane of an Olympus 50X object lens (NA=0.25, depth of focus 10μm). The micro-lens was moved along the z axis at the step of 10μm by a piezo-electrical driven stage. A camera was used to record the laser intensity distribution when the phosphorene-based micro-lens was moved at different z values. After the measurements, a three-dimensional laser light distribution dataset was built. For measurement of the power-dependent optical property of the micro-lens, a neutral-density filter was applied to tune the incident laser power continuously; for measurement of the gate-dependent optical property, a Keithley 4200 semiconductor analyser was applied.

Furthermore, nanoindentation was used to characterize the mechanical properties of the micro-lens. EDX (energy-dispersive X-ray spectroscopy) SEM measurements were made to characterize the chemical composition and distribution of the micro-lens, respectively.

5.2.1 Micro-lens geometry and focal length

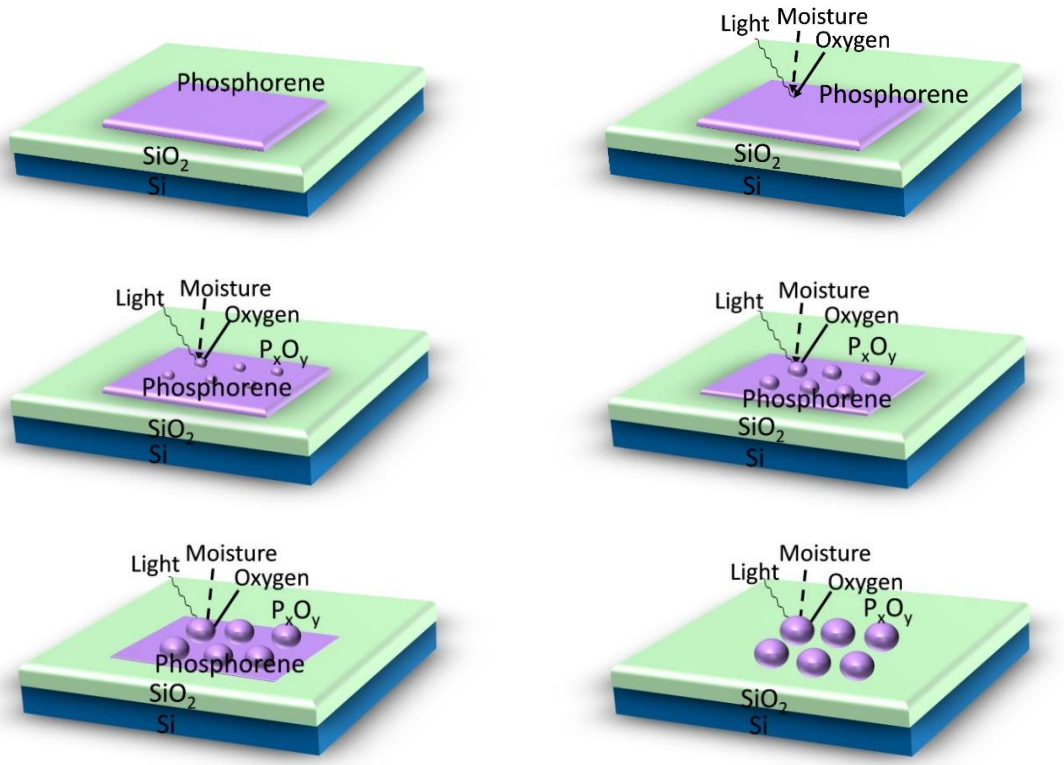

Figure 5.9 **Schematic plot of black phosphorus micro-lens transformation process.**

Phosphorene is very active in air when light and moisture are involved [106, 169]. A schematic plot of the black phosphorus micro-lens transformation process is shown in Figure 5.9. The schematic diagram shows clearly how black phosphorus degrades when light, water and oxygen are present [170]. The bubble growth process is also shown in Figure 5.9.

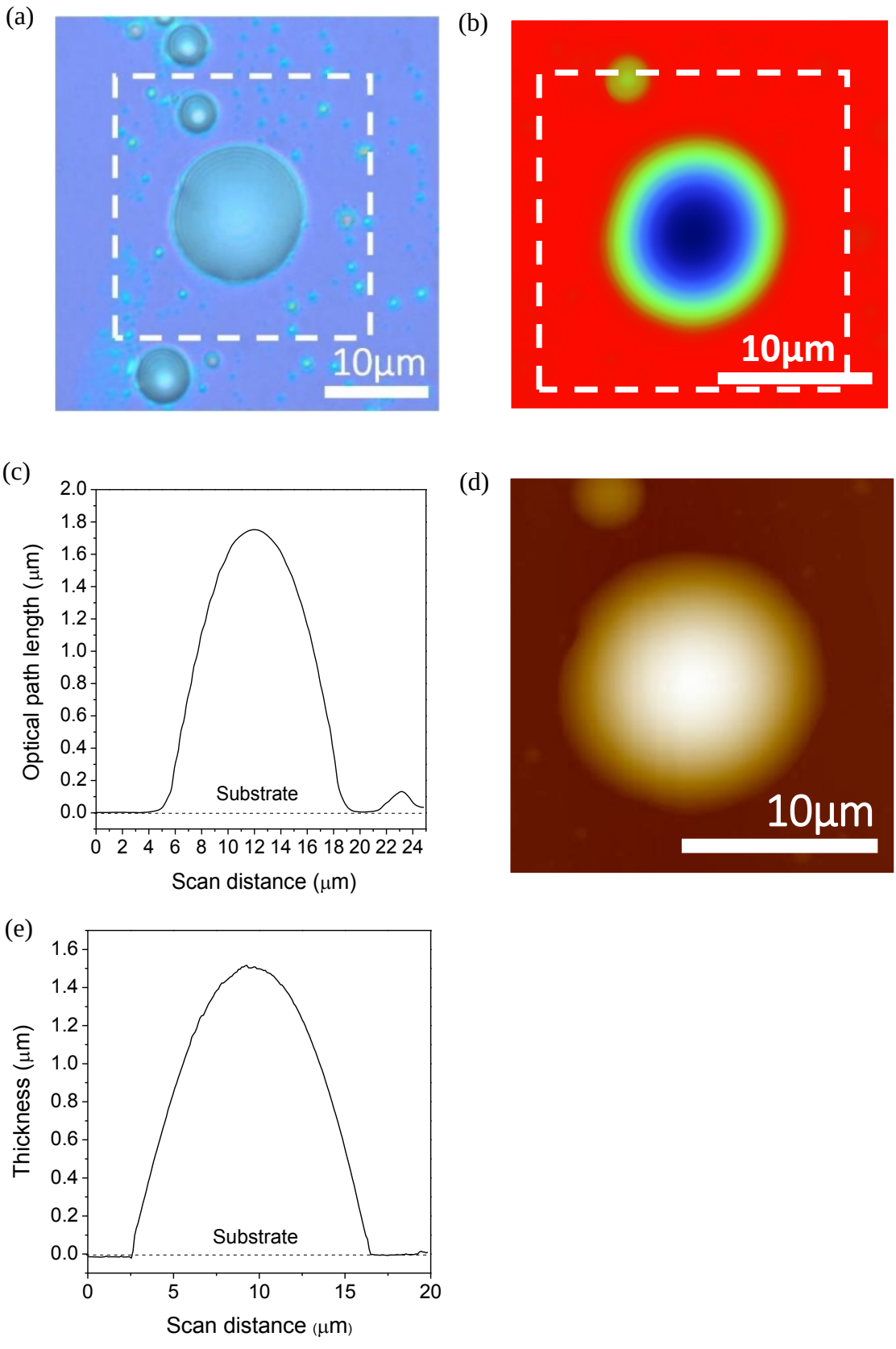

Figure 5.10 **Black phosphorus characterization by microscope, PSI and AFM (a)** Optical microscope image of black phosphorus micro-lens. **(b)** PSI image of black

phosphorus micro-lens from the dashed line box area in (a). **(c)** OPL measured by PSI along the dashed line indicated in (b). **(d)** AFM image of black phosphorus micro-lens from the dashed line box area indicated in (b). **(e)** Thickness measured by AFM along the dashed line indicated in (d).

After degradation, the black phosphorus bubbles were characterized by optical microscope. As shown in Figure 5.10a, different colours represent different thicknesses. Then the optical geometry (Figure 5.10b) and physical geometry (Figure 5.10d) of these bubbles were measured via PSI and AFM respectively. The optical thickness and physical thickness of the phosphorene bubble are shown in Figure 5.10c and Figure 5.10d respectively, indicating that the bubble had symmetry and a surface gradient.

5.2.2 Micro-lens optical property

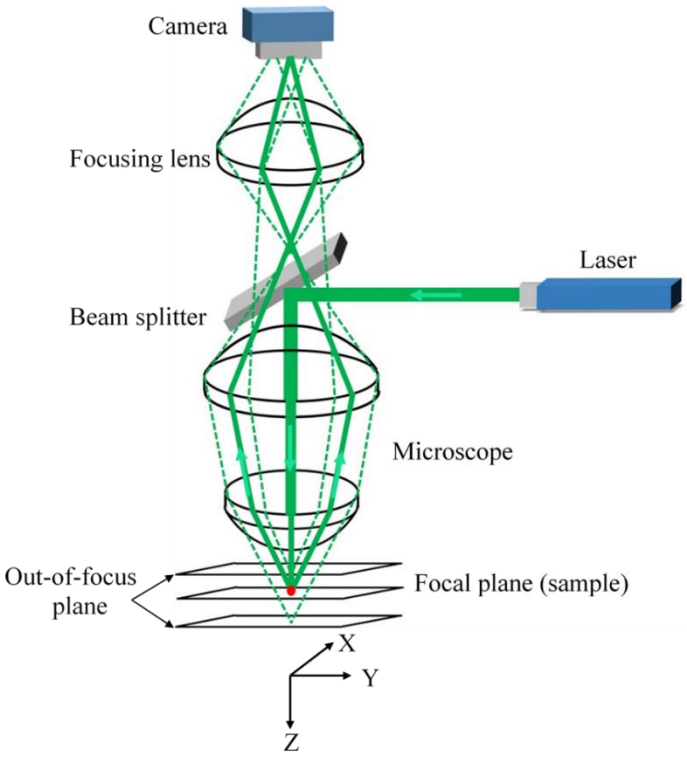

Figure 5.11 **Schematic plot of the far-field optical microscope (SOM) used for black phosphorus micro-lens characterization** [80].

After the geometry characterization of the bubble, the optical focal length was measured by SOM. From the SOM measurements and image processing, a 3D distribution dataset was obtained and a cross-section of the light intensity distribution along the x axis and z axis directions was plotted and shown in Figure 5.11. When the micro-lens was placed at a distance of 2|f| above (or below) the focal plane, the focused incident laser was reimaged, equivalent to that from a point source. Thus, a well-focused laser light spot appeared, and the distance f was the focal length of the phosphorene-based micro-lens.

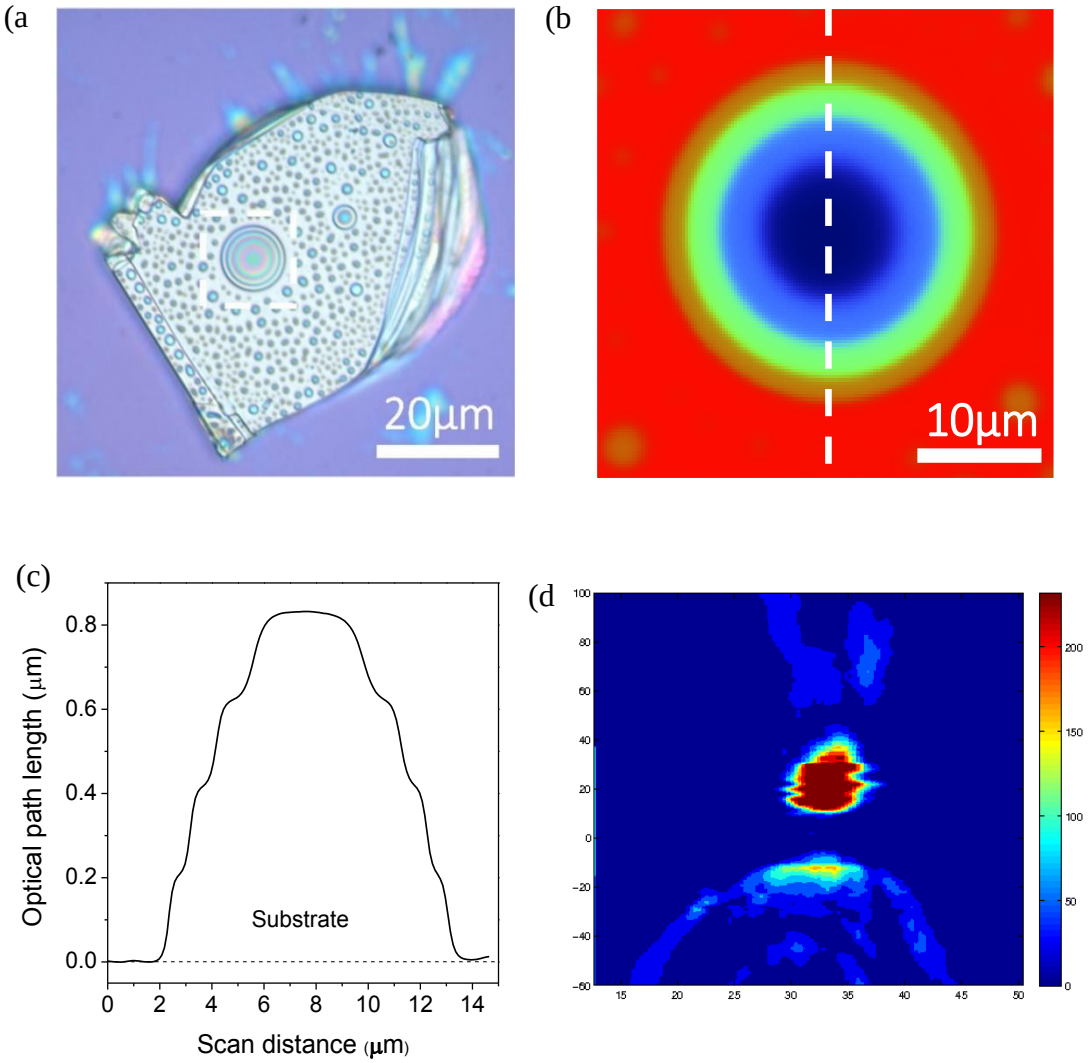

Figure 5.12 **Spontaneously formed micro-lens on a thick black phosphorus flake (a)** Microscope image of a spontaneously formed micro-lens on a thick black phosphorus

flake. **(b)** PSI image of spontaneously formed micro-lens on a thick black phosphorus flake. **(c)** OPL measured by PSI along the dashed line indicated in (b). **(d)** Intensity distribution of spontaneously formed micro-lens on a thick black phosphorus flake characterized by SOM.

The optical microscope and PSI image of a spontaneously formed black phosphorus micro-lens on a thick black phosphorus flake are shown in Figure 5.12a and Figure 5.12b respectively, and OPL is displayed in Figure 5.12c. Figure 5.12d is the intensity distribution of the spontaneously formed black phosphorus micro-lens on a thick black phosphorus flake characterized by SOM. From Figure 5.12d it is obvious that light refocuses at two out-of-focus planes at f=10 μ m and f=-6 μ m, respectively, and there is no light refocusing of the SiO_2/Si substrate at an out-of-focus plane.

5.2.3 Micro-lens optical property stability

Figure 5.13 provides information about the tunability of a spontaneously formed black phosphorus micro-lens with different incident laser power and different applied back-gate voltage. From Figure 5.13a it is evident that the focal length of the black phosphorus remains at around f=18 μ m and f= -9 μ m when the power of the incident laser ranges from 0 to 160 μ W, indicating that the phosphorene-based micro-lens has good stability within the power range.

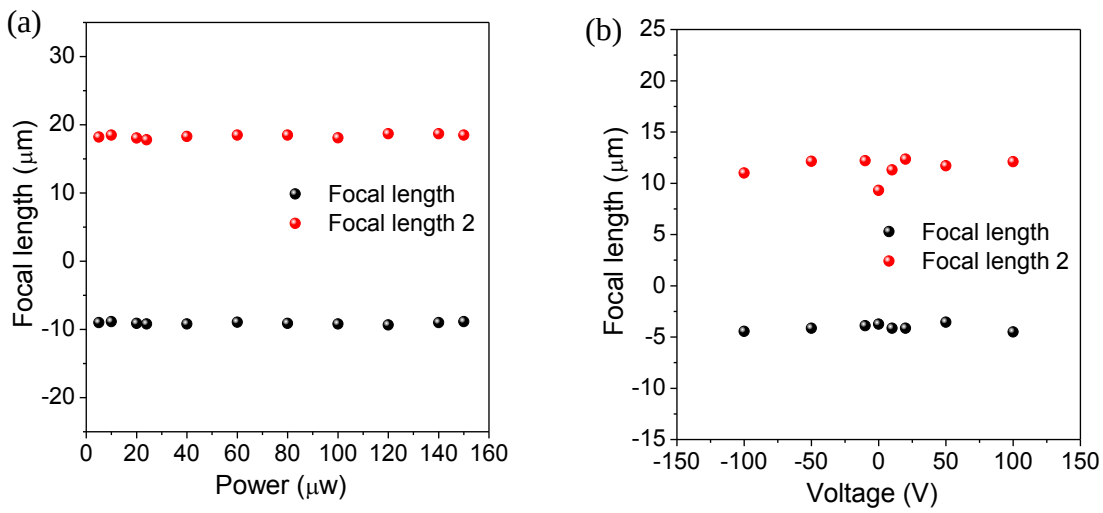

Figure 5.13 **Tunability of spontaneously formed black phosphorus micro-lens. (a)** Measured focal length data with laser power ranging from 10μw to 100 μw. **(b)** Measured focal length data with voltage raging from -50V to 50V.

To measure the gate-dependent focal length, Au electrodes were pre-patterned via lithography on n doped Si/SiO_2 substrate (275 nm thermal SiO_2). Then a black phosphorus micro-lens formed on the pre-patterned Au electrode was selected, forming a MOS device. The Au electrode was then grounded, and back-gate voltage was applied to the MOS device. While the applied back-gate voltage varied from -150V to 150V, the focal lengths exhibited relatively stable states of ~12 μ m and ~ -4 μ m respectively, except for some fluctuations around 0V.

5.2.4 Micro-lens optical property tunability

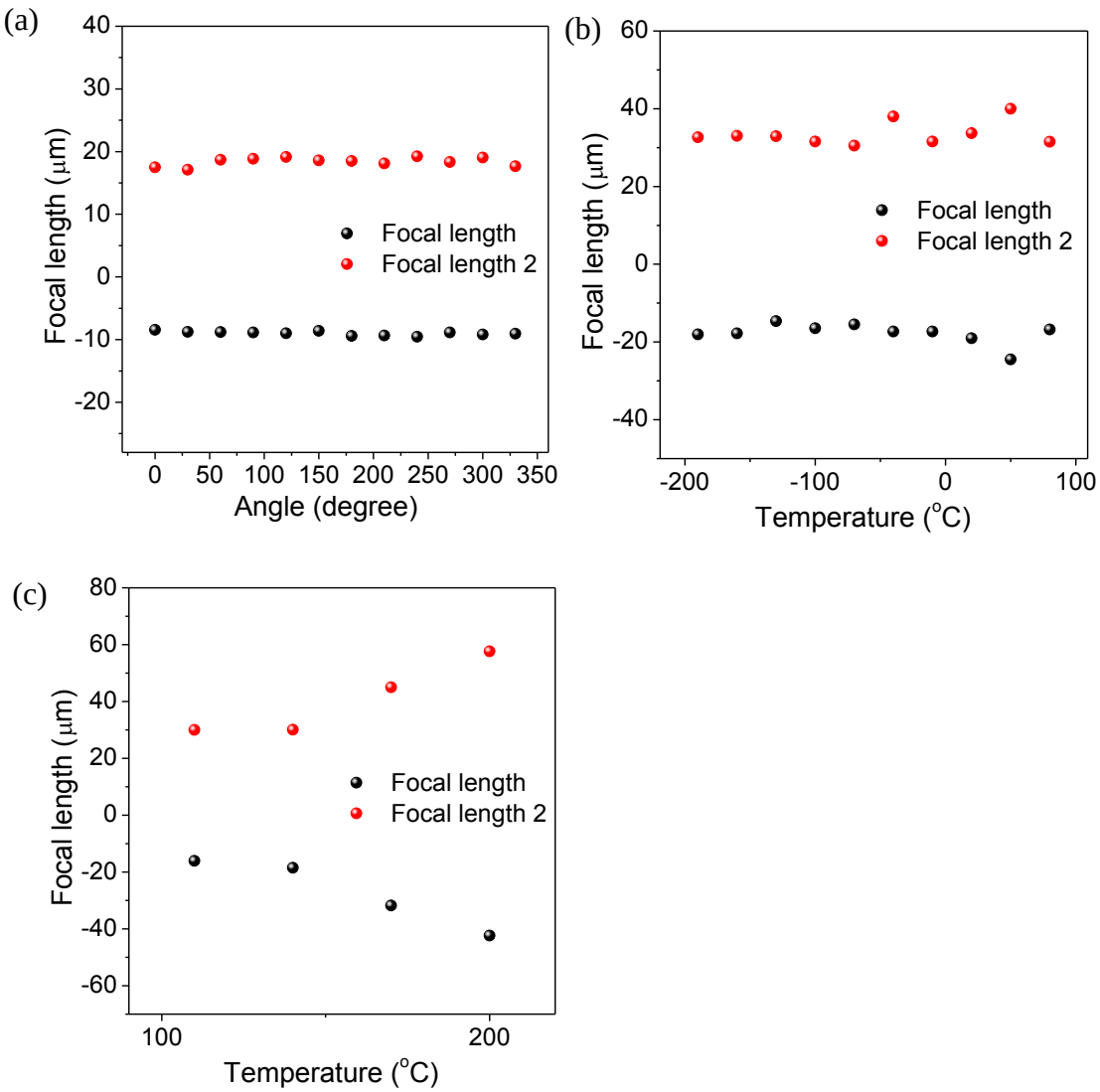

Figure 5.14 **Tunability of spontaneously formed black phosphorus micro-lens. (a)** Measured focal length data with different incident laser polarization angles ranging from 0 to 330 degrees. **(b)** Measured focal length data at temperatures ranging from -190 to 80℃. **(c)** Measured focal length data with temperatures ranging from 110 to 200℃

Figure 5.14a shows the tunability of a spontaneously formed black phosphorus micro-lens with the polarization angle ranging from 0 degree to 330 degrees. The focal length of the spontaneously formed black phosphorus micro-lens shows an isotropic nature. In terms of the temperature-dependent focal length, the measurements demonstrated that the focal length remained stable with the temperature ranging from -190 to 80℃, while the focal length was tuned when the temperature varied from 110 to 200℃. Moreover, the micro-lens was destroyed when a temperature greater than 200℃ was applied to the system.

5.2.5 Micro-lens mechanical properties

The mechanical properties of a spontaneously formed black phosphorus micro-lens were measured via nanoindentation. A series of loading and unloading nanoindentation traces are shown in Figure 5.15.

Figure 5.15a and Figure 5.15d demonstrate load and unload plotting with the loading force of 100μN, from which it is obvious that black phosphorus bubbles show elastic deformation at the loading force of 100μN. Similar elastic deformation at the loading force of 500μN is demonstrated in Figure 5.15b. After the measurements, the reduced modulus E_r of the micro-lens is achieved (around 291GPa) by a fitting load-displacement curve, assuming that a perfectly pyramidal indenter is used with data obtained using a calibrated area.

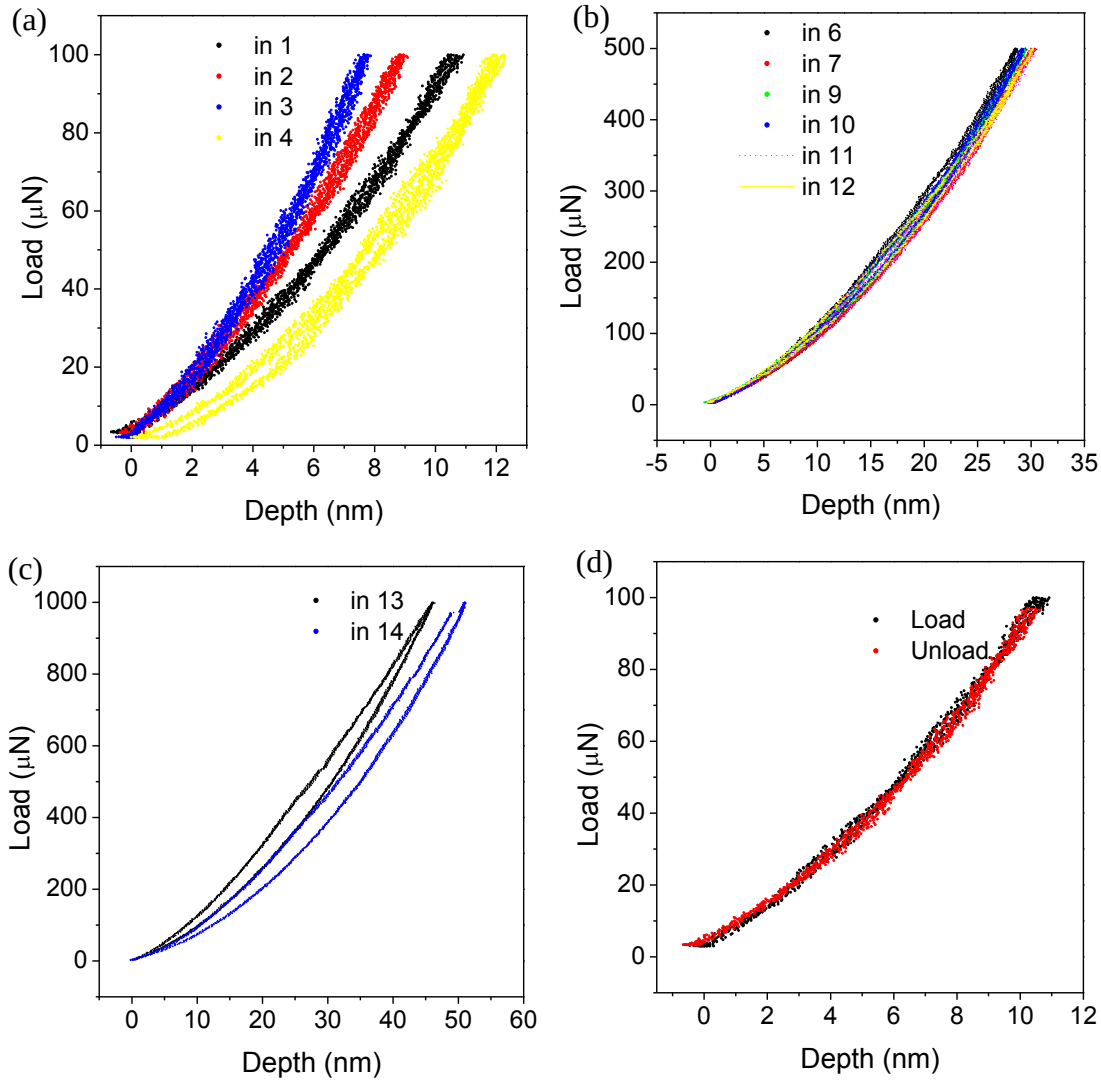

Figure 5.15 **Mechanical properties of spontaneously formed black phosphorus micro-lens.** A series of nanoindentation traces for a spontaneously formed black phosphorus micro-lens with maximum load at **(a)** 100μN, **(b)** 500μN and **(c)** 1000μN. **(d)** Load-displacement data for spontaneously formed black phosphorus micro-lens. The maximum force is 100μN.

5.2.6 Micro-lens chemical composition

In order to qualitatively characterize the chemical composition of the spontaneously formed black phosphorus micro-lens, SEM and EDX measurements were conducted. Figure 5.16a shows the SEM image of a spontaneously formed black phosphorus micro-lens on silicon substrate. Figure 5.16 b, c and d indicate the distribution of the elements O, Si and P around the micro-lens area respectively. The spontaneously formed black phosphorus micro-lens shown in Figure 5.16 had a porous surface and was composed mainly of chemicals O and P, which was consistent with those from previous reports [170, 171]. From the quantity analysis from EDX, the chemical ratio between P and O was about 1.03.

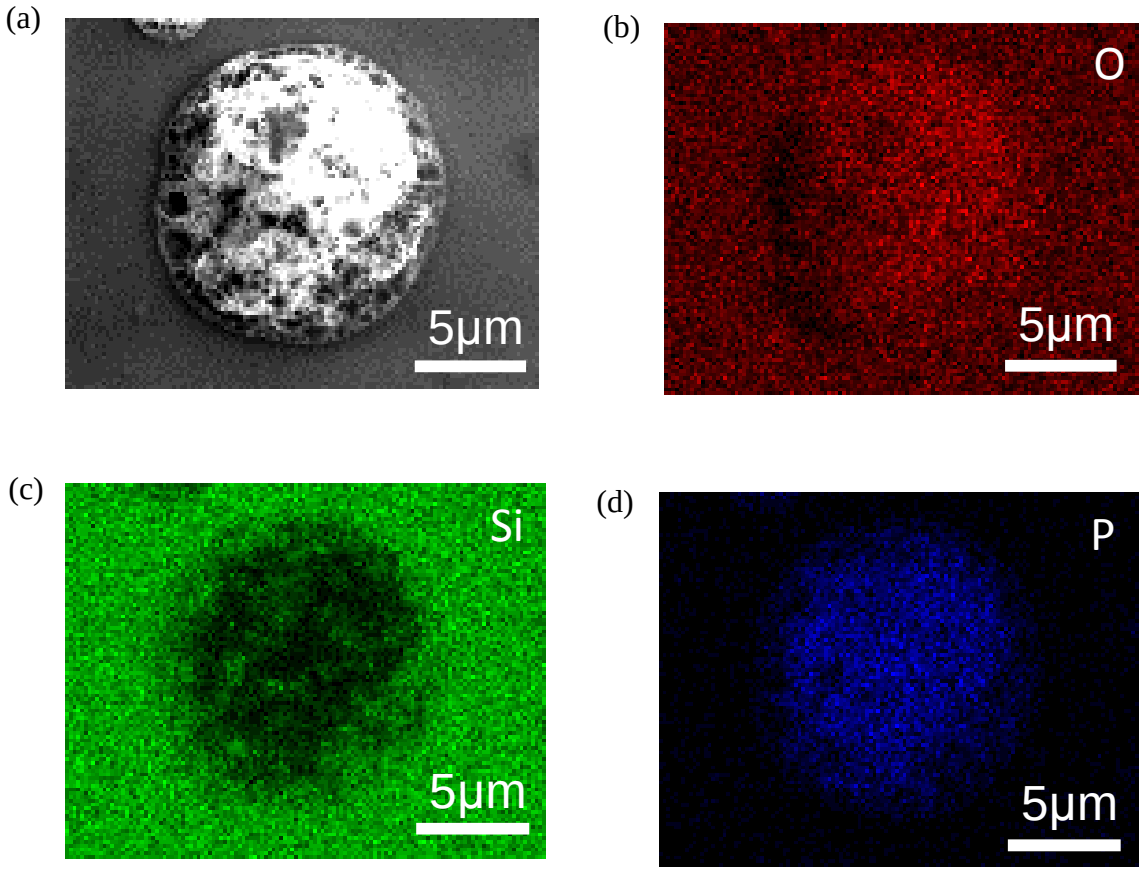

Figure 5.16 **SEM and EDX mapping of a spontaneously formed black phosphorus micro-lens on silicon substrate. (a)** SEM image of a spontaneously formed black

phosphorus micro-lens. **(b)-(d)** are the corresponding EDX mappings of O, Si and P respectively.

5.2.7 Other forms of black-phosphorus-based micro-lens

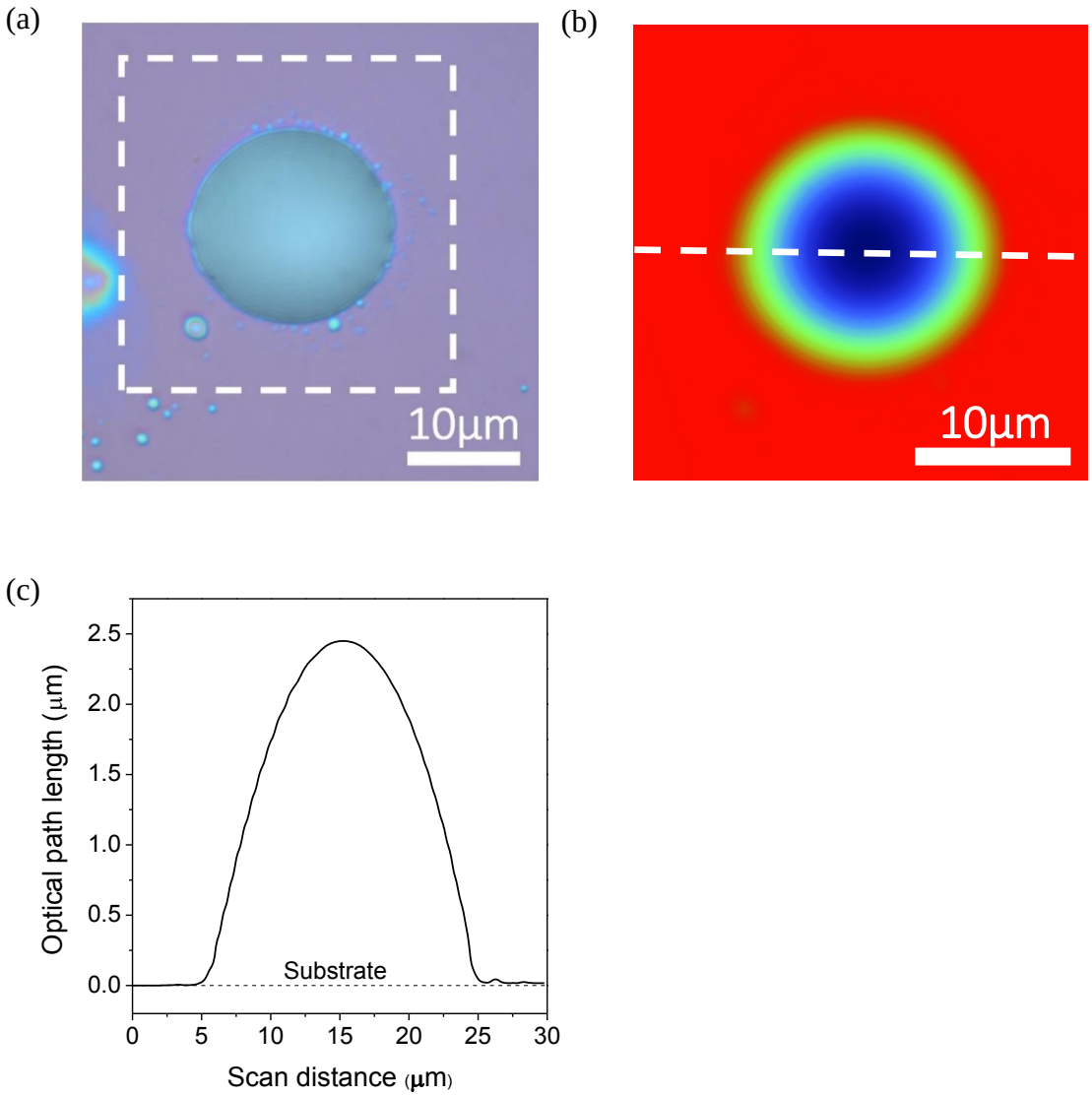

Figure 5.17 **Spontaneously formed black phosphorus micro-lens. (a)** Microscope image of a spontaneously formed black phosphorus micro-lens **(b)** PSI image of the spontaneously formed black phosphorus micro-lens from the dashed box line area in (a). **(c)** OPL measured by PSI along the dashed line indicated in (b).

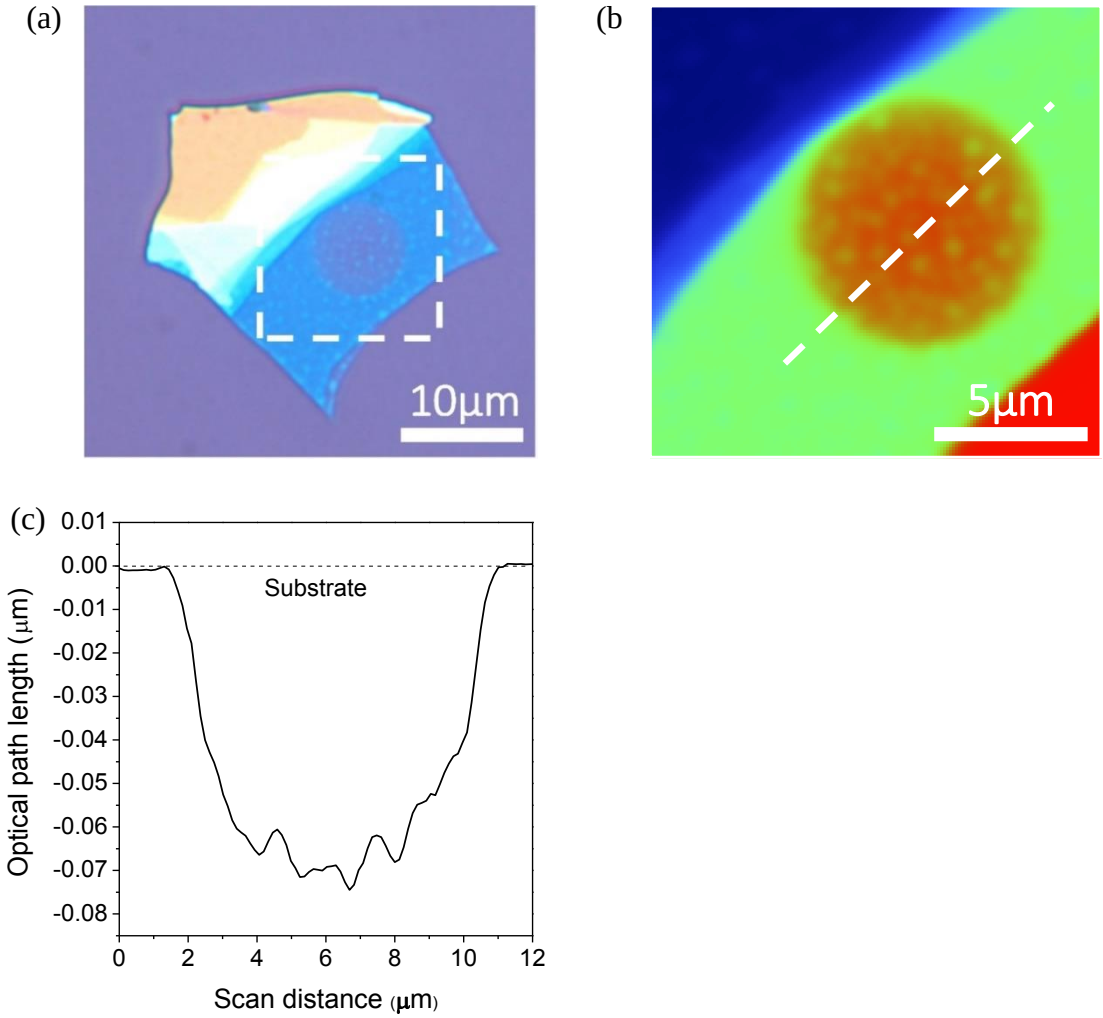

Figure 5.18 **Atomic thin micro-lens fabricated from black phosphorus by focused ion beam (FIB). (a)** Microscope image of the atomic thin micro-lens fabricated from black phosphorus **(b)** PSI image of the atomic thin micro-lens fabricated from black phosphorus. **(c)** OPL measured by PSI along the dashed line indicated in (b).

Apart from the spontaneously formed micro-lens on a thick black phosphorus flake, another two types of black-phosphorus-based micro-lens were also studied, namely a spontaneously formed black-phosphorus-based micro-lens on SiO_2/Si substrate and a black-phosphorus-based atomic thin micro-lens fabricated by FIB, which are presented in Figure 5.17 and Figure 5.18 respectively.

5.3 Summary

Phase-shifting interferometry (PSI) was used to measure OPL by analysing the digitized interference pattern, for investigating elastic light-matter interactions. Giant OPLs were observed, owing to multiple interfacial light reflections. Based on the OPL study, a one-to-one relation between the OPL and the number of layers was firmly established by first-principles optical calculation and experimental calibration. Note that even though the thickness of one-layer phosphorene is less than 1 nm, its OPL is significantly greater than 20 nm. That is, the virtual thickness of a phosphorene flake is amplified more than 20 times in optical interferometry, allowing the flakes to be easily identified. Moreover, measurement by PSI takes much less time than the conventional way of determining number of layers, thus effectively decreasing the phosphorene degradation problem. Therefore, this research into OPL determination via the PSI method provides an accurate and efficient way to identify the number of layers in few-layer phosphorene.

When phosphorene reacts with oxygen and the moisture, the phosphorene degrades and the reaction product P_xO_y is formed. The chemical reaction products are spontaneously present in the form of micro-bubbles, which can be applied for building micro-lenses. These micro-lenses have stable focal length, with variably applied back-gate voltage, incident laser power and polarization angle. The focal length of these micro-lenses remains stable in surrounding temperatures ranging from -190 to 80℃; however, the focal length can be tuned in surrounding temperatures ranging from 110 to 200℃. Furthermore, the micro-lens demonstrates an elastic property when a load is applied to it by microprobe. This research provides useful experimental data regarding the phosphorus degradation products and their relevant, promising applications in the area of optical devices.

Chapter 6 Conclusion

The main objective of the research reported in this thesis was to study inelastic and elastic light-matter interactions in the newly discovered 2D nanomaterial, phosphorene. The research scope covers:

1. Study of atomic oscillation performance in phosphorene, and related temperature-dependent, polarization-dependent Raman response. The anisotropic Raman response in few-layer phosphorene was observed and enabled the use of an optical method to quickly determine the crystalline orientation.

2. Bandgap energy and band structure of few-layer phosphorene were investigated. This new material was rediscovered and predicted to be promising in spectra range. However, very few experimental reports were available regarding the bandgap energy for phosphorene. The results presented here provide much-needed experimental information about the band structures and exciton nature in few-layer phosphorene.

3. Exciton and trion dynamics in 3L phosphorene were studied by controlling the carrier doping level using electrostatic modulation. For the first time, the extraordinary binding energy of 3L phosphorene as well as its quasi-1D excitonic and trionic behaviours were verified by experimental results and theoretical calculations.

4. Layer-dependent OPL in few-layer phosphorene was studied. A new method based on OPL was developed to identify the number of layers of phosphorene efficiently and accurately, in order to resolve the phosphorene degradation problem.

5. Few-layer phosphorene-based micro-lenses were fabricated and their optical performance was evaluated.

6.1 Concluding remarks

6.1.1 Atomic oscillation performance in phosphorene

The atomic arrangement in phosphorene is anisotropic in different directions: zigzag, armchair and z directions. Raman peaks result from the vibrations from atoms in the three different directions. Relying on the inelastic light-matter interaction, the Raman effect gives information about photon-phonon energy transfer.

The measured Raman peaks at 359, 437, and 466 cm^{-1} were attributed to the $A\,{}^{1}_{g}$, B_{2g} and A_g^2 phonon modes in crystalline few-layer phosphorene flakes, which matched well with observations in bulk black phosphorus.

Temperature-dependent Raman measurements were performed to further understand the fine structure and properties of the material. The results indicated that the phonon frequencies in few-layer phosphorene were more sensitive to temperature modulation than those in graphene and MoS_2, which could be due to the superior mechanical flexibility of phosphorene originating from its unique puckered crystal structure.

Compared with other 2D materials, phosphorene shows strong anisotropic properties. A polarization-dependent Raman study was conducted and is was observed that the Raman intensities of B_{2g} and A_g^2 modes were significantly dependent on the polarization angle. The angle-dependent intensities of B_{2g} and A_g^2 modes both showed an angle period of 180° and were out of phase. The Raman intensity of A_g^1 was less sensitive to the polarization angle.

The measurement results could be perfectly explained by the vibration directions of these three Raman modes in crystalline black phosphorus [104]. In A_g^2, B_{2g} and A_g^1 vibrational modes, the phosphorus atoms oscillate along the zigzag, armchair and out-of-plane directions, respectively. When the laser polarization is parallel to the zigzag direction

(armchair direction), the intensity of the B_{2g} mode reaches its maximum (minimum) value, and the intensity of the A_g^2 mode reach its minimum (maximum) value. The measurement results matched the theoretical prediction well. On the basis of this polarization-dependent Raman measurement, the crystalline orientation of this 15L phosphorene flake was quickly determined. This technique provided fast and precise determination of the crystalline orientation without the need for complicated and high-resolution imaging systems such as STM or TEM.

6.1.2 Extraordinary photoluminescence from few-layer phosphorene

Few-layer phosphorene with narrow bandgaps ranging from mid-infrared to near-infrared wavelengths can fill the space between the gapless graphene and the comparably large gap TMD semiconductors. However, very few experimental reports regarding the bandgap energy were available to confirm the theoretical prediction for phosphorene.

In the research reported in this thesis, the bandgap energy in few-layer phosphorene was investigated via PL measurements. The PL measurements were conducted in a T64000 micro-Raman/PL system equipped with both CCD and InGaAs detectors. Few-layer phosphorene flakes were quickly identified by optical contrast under an optical microscope, after which the sample was quickly put into a microscope-compatible chamber with a slow flow of nitrogen protection gas used to slow the reaction of phosphorene with moisture and other possible reactants from the environment. Then PSI was applied to quickly and accurately identify the number of layers to slow the degradation of few-layer phosphorene.

After the PL measurements, strong and highly layer-dependent photoluminescence in few-layer phosphorene (two to five layers) was observed successfully. The measured PL spectra in few-layer phosphorus were highly dependent on the number of layers (2 to 5). Strong PL peaks at 961 nm, 1268 nm, 1413 nm and 1558 nm were observed in 2, 3, 4 and

5-layered phosphorene, respectively, which corresponded to energy peaks of 1.29 eV, 0.98eV, 0.88 eV and 0.80 eV, respectively. The measured PL peaks were likely attributable to the nature of excitons which represented lower bounds on the fundamental bandgap values in few-layer phosphorene. The energy position of the measured PL peak increased rapidly as the number of layers decreased. This result indirectly confirmed the theoretical calculation findings that the bandgap of few-layer phosphorene increased rapidly as the number of layers decreased, due to the quantum confinement effect.

The internal luminescence quantum efficiency was studied to further understand the band structure in few-layer phosphorene. The PL peak intensity was observed to increase dramatically when the number of layers decreased, despite the reduced amount of material. The strong PL in few-layer phosphorene arose from direct electronic transitions with high radiative recombination rate. The internal luminescence quantum efficiency from such direct electronic transitions in few-layer phosphorene was related to rates of radiative recombination, defect trapping and electron relaxation within the conduction and valence bands respectively. The rates of both radiative recombination and electron relaxation were highly related to the density of states and the band structures. Then the band structures in few-layer phosphorene were calculated, from which this strong layer-dependent internal quantum efficiency could be understood. As the number of layers increased from monolayer to five-layer, increasing band valleys and band maxima showed up within both the conduction and valence bands, respectively. Those emerging valleys (maxima) in the conduction (valence) band significantly changed the density of states distribution for electrons (holes). In particular, the states provided by those valleys or maxima at the off-Γ points highly enhanced the relaxation rates within the conduction or valence bands, leading to lower internal quantum efficiency in 5L phosphorene compared to that in 2L.

The results presented in this thesis provide much-needed experimental information about the band structures and exciton nature in few-layer phosphorene.

6.1.3 Exciton and trion dynamics and quasi-one-dimension nature in 3L phosphorene

Exciton and trion dynamics in 3L phosphorene were studied by exploiting their inelastic interactions with laser. For the first time, 3L phosphorene's extraordinary binding energy and quasi-1D excitonic and trionic behaviours in a large 2D area were measured by experimental results and theoretical calculations.

A neutral exciton is a bound quasi-particle state between one electron and one hole through a Coulomb interaction, similar to a neutral hydrogen atom. A trion is a charged exciton composed of two electrons and one hole (or two holes and one electron), analogous to H^- (or H_2^+). Trions have been of considerable interest in the fundamental studies of many-body interactions. In contrast to the exciton, a trion has an extra charge with nonzero spin, which can be used for spin manipulation [118, 151]. More importantly, the density of trions can be electrically tuned by the gate voltage, enabling remarkable optoelectronic applications [103, 119, 120, 150, 152]. For these purposes, a large trion binding energy is critical in order to overcome room-temperature thermal fluctuations as well as to widen the spectral tuning range.

Back-gate voltage was applied to a phosphorene MOS device and a trion (charged exciton) binding energy of ~162 meV was observed in 3L phosphorene at room temperature, which is nearly 1−2 orders of magnitude larger than that reported in 2D transition metal dichalcogenide semiconductors (20−30 meV) and quasi-2D quantum wells (~1−5 meV). For comparison, the trion binding energy in 1L $MoS_{2x}Se_{2(1-x)}$ (x=0.45) was studied, further testifying that the trion binding energy in 3L phosphorene was far greater than that in conventional 2D materials.

Such a large trion binding energy has only been observed in truly 1D materials such as carbon nanotubes, whose optoelectronic applications are severely hindered by their intrinsically small optical cross-sections. Phosphorene offers an elegant way of

overcoming this hurdle by enabling quasi-1D excitonic and trionic behaviours in a large 2D area, allowing optoelectronic integration.

In addition, the quasi-1D nature of excitonic and trionic dynamics in phosphorene were experimentally validated by demonstrating completely linearly polarized light emission from excitons and trions in few-layer phosphorene. Moreover, the dimension of trions in 3L phosphorene was also calculated via the variational quantum Monte Carlo method and the effective dimension of trions in 3L phosphorene was estimated to be $D \sim 1.58$, further supporting the quasi-1D nature of trions demonstrated earlier by experiments. The implications of the extraordinarily large trion binding energy in a higher-than-one-dimensional material are far-reaching. It provides a room-temperature 2D platform for observing fundamental many-body interactions in the quasi-1D region. The strong photoluminescence emission in phosphorene was electrically tuned over a large spectral range at room temperature, opening a new route for tunable light sources.

6.1.4 Optical path length of few-layer phosphorene

The layer-dependent OPL in few-layer phosphorene was measured by PSI and the OPL results provided information about light propagation in few-layer phosphorene.

The phosphorene flakes were fabricated using mechanical exfoliation techniques and identified by optical contrast in a microscope. Regions with different colours corresponded to phosphorene flakes of different thickness. Typically, atomic force microscopy (AFM) is applied in determination of the thickness of few-layer materials. But few-layer phosphorene is very sensitive to oxygen and water, while monolayer phosphorene becomes P_xO_y in as little as ten minutes in air. Therefore, AFM tends to be unreliable for the identification of very-few-layer phosphorene (one or two layers) because of its slow scanning speed and the potential contact contamination. A unique challenge in working with unstable phosphorene is determination of the number of layers.

In this project, a rapid, noninvasive and highly accurate approach was proposed to determine the number of layers using optical interferometry. Specifically, the OPL of the light reflected from the phosphorene was measured. The OPL was determined as $OPL_{BP} = -\frac{\lambda}{2\pi}(\phi_{BP} - \phi_{SiO_2})$, where λ =535 nm is the wavelength of the light source andϕ_{BP} and ϕ_{SiO_2} are the phase shifts of the light reflected from the phosphorene flake and the SiO2/Si substrate respectively. The one-to-one relation between the OPL and the number of layers was firmly established by first-principles optical calculation and experimental calibration (one-to-one relationship between OPL and physical thickness measured by AFM). Note that even though the thickness of one-layer phosphorene is less than 1 nm, its OPL is significantly larger than 20 nm, owing to the multiple interfacial light reflections. That is, the virtual thickness of a phosphorene flake is amplified more than 20 times in optical interferometry, allowing the flakes to be easily identified.

Considering that the accuracy of the instrument was ~0.1 nm, a step change of 20 nm yielded an extremely robust measurement. In experiment, the number of layers of the phosphorene flake was first estimated according to its optical contrast in an optical microscope and then accurately identified by PSI.

In summary, the OPL study in my research implied the elastic light-matter interactions. Moreover, based on OPL, a new method was developed to identify the number of layers of phosphorene efficiently and accurately, effectively eliminating the side effects resulting from phosphorene degradation problems.

6.1.5 Phosphorene-based micro-lens

Few-layer phosphorene-based micro-lenses were fabricated and their optical performance was evaluated. The optical performance of the micro-lens was measured based on elastic light-matter interactions.

During the micro-Raman/PL measurements, actions were taken to eliminate phosphorene degradation in order to achieve accurate determination of the optical properties of phosphorene. However, the degradation of phosphorene occurred spontaneously when phosphorene reacted with oxygen and moisture, and the reaction products turned out to be P_xO_y. The degradation products occurred in the form of micro-bubbles, and these bubbles functioned well as black-phosphorus-based micro-lenses.

For the study of black-phosphorus-based micro-lens optical focal lengths, a far-field scanning optical microscopy (SOM) system was built on the base of a micro-Raman system. The measurements showed that black-phosphorus-based micro-lenses had a stable focal length, with variations of the applied back-gate voltage, incident laser power and polarization angle. Moreover, the focal length of these micro-lenses remained stable while the surrounding temperature ranged from -190 to 80℃. However, the focal length was tuned with the surrounding temperature rising from 110 to 200℃. In addition, the micro-lenses showed an elastic property when a load of 100 μN was applied by microprobe. This research provides experimental data regarding phosphorus degradation products and their relevant, promising applicability in the area of optical devices.

6.2 Highlights

The main highlights of my project are summarized as:

a) Experimentally measured the temperature-dependent Raman effect and polarization-dependent Raman effect in black phosphorus flakes; demonstrated that few-layer phosphorene is more sensitive to temperature modulation than graphene and MoS_2 in Raman scattering; Proposed an optical method, based on anisotropic Raman response in few-layer phosphorene, to quickly determine the crystalline orientation without tunnelling electron microscopy or scanning tunnelling microscopy.

b) Experimentally verified strong and highly layer-dependent photoluminescence in few-layer phosphorene (two to five layers). The results confirmed the theoretical prediction that few-layer phosphorene has a direct and layer-sensitive bandgap. The internal luminescence quantum efficiency was also studied to further understand the band structure in few-layer phosphorene. My work provides much-needed experimental information about the band structures and exciton nature in few-layer phosphorene. Temperature and power dependence of PL were also studied in phosphorene.

c) Experimentally studied the exciton and trion dynamics in few-layer phosphorene and monolayer $MoS_{2x}Se_{2(1-x)}$ (x=0.45). Reported a trion (charged exciton) binding energy of ∼162 meV in 3L phosphorene at room temperature, which is nearly 1−2 orders of magnitude larger than that in two-dimensional (2D) transition metal dichalcogenide semiconductors (20−30 meV) and quasi-2D quantum wells (∼1−5 meV). And then experimentally validated the quasi-1D nature of excitonic and trionic dynamics in phosphorene by demonstrating completely linearly polarized light emission from excitons and trions in few-layer phosphorene. The dimension of trions in 3L phosphorene was also calculated via a variational quantum Monte Carlo method and the effective dimension of trions in 3L phosphorene was estimated to be D ∼ 1.58, further supporting the quasi-1D nature of trions demonstrated earlier by experiments.

d) Conducted material characterization measurements via optical microscope, PSI and AFM. On the basis of these measurements, proposed implementation of a rapid, noninvasive and highly accurate approach based on OPL. The one-to-one relation between the OPL and the number of layers was firmly established by first-principles optical calculation and experimental calibration; A few-layer phosphorene-based micro-lens was fabricated and its optical performance was evaluated. The optical

performance of the micro-lens was measured based on elastic light-matter interactions.

6.3 Future work

1) In my research, I found that the PL of phosphorene can be tuned by temperature, back-gate voltage and excitation laser polarization angle. Furthermore, the direct bandgap nature of phosphorene leads to extraordinary PL emission which enables few-layer phosphorene to be applied in highly efficient light-emitting devices. Therefore, the development of few-layer phosphorene-based light-emitting devices with tunable light emission is anticipated.

2) Phosphorene possesses both a large optical cross-section (as typically exhibited by a 2D material system) and high trion binding energies (as typically exhibited by a 1D system), allowing remarkable optoelectronic applications, including photo-detectors and spin manipulation devices.

3) The $MoS_{2x}Se_{2(1-x)}$ bandgap compatible with Si semiconductor is also a promising research target.

Bibliography

[1] F. Xia, H. Wang, D. Xiao, M. Dubey, A. Ramasubramaniam, Two-dimensional material nanophotonics, Nature Photonics, 8(12) (2014) 899-907.

[2] Y.-L. Kang, Z.-F. Zhang, H.-W. Wang, Q.-H. Qin, Experimental investigations of the effect of thickness on fracture toughness of metallic foils, Materials Science and Engineering: A, 394(1-2) (2005) 312-319.

[3] H.-W. Wang, Y.-L. Kang, Z.-F. Zhang, Q.-H. Qin, Size effect on the fracture toughness of metallic foil, International Journal of Fracture, 123(3-4) (2003) 177-185.

[4] G. Eda, S.A. Maier, Two-dimensional crystals: managing light for optoelectronics, Acs Nano, 7(7) (2013) 5660-5665.

[5] K.S. Novoselov, A.K. Geim, S.V. Morozov, D. Jiang, M.I. Katsnelson, I.V. Grigorieva, S.V. Dubonos, A.A. Firsov, Two-dimensional gas of massless Dirac fermions in graphene, Nature, 438(7065) (2005) 197-200.

[6] Y. Zhang, Y.-W. Tan, H.L. Stormer, P. Kim, Experimental observation of the quantum Hall effect and Berry's phase in graphene, nature, 438(7065) (2005) 201-204.

[7] K.F. Mak, C. Lee, J. Hone, J. Shan, T.F. Heinz, Atomically Thin MoS2: A New Direct-Gap Semiconductor Physical Review Letters, 105(13) (2010) 136805.

[8] A. Splendiani, L. Sun, Y. Zhang, T. Li, J. Kim, C.-Y. Chim, G. Galli, F. Wang, Emerging Photoluminescence in Monolayer MoS2, Nano Letters, 10(4) (2010) 1271-1275.

[9] M. Liu, X. Yin, E. Ulin-Avila, B. Geng, T. Zentgraf, L. Ju, F. Wang, X. Zhang, A graphene-based broadband optical modulator, Nature, 474(7349) (2011) 64-67.

[10] X. Gan, R.-J. Shiue, Y. Gao, I. Meric, T.F. Heinz, K. Shepard, J. Hone, S. Assefa, D. Englund, Chip-integrated ultrafast graphene photodetector with high responsivity, Nature Photonics, 7(11) (2013) 883-887.

[11] X. Wang, Z. Cheng, K. Xu, H.K. Tsang, J.-B. Xu, High-responsivity graphene/silicon-heterostructure waveguide photodetectors, Nature Photonics, 7(11) (2013) 888-891.

[12] A. Pospischil, M. Humer, M.M. Furchi, D. Bachmann, R. Guider, T. Fromherz, T. Mueller, CMOS-compatible graphene photodetector covering all optical communication bands, Nature Photonics, 7(11) (2013) 892-896.

[13] M. Furchi, A. Urich, A. Pospischil, G. Lilley, K. Unterrainer, H. Detz, P. Klang, A.M. Andrews, W. Schrenk, G. Strasser, Microcavity-integrated graphene photodetector, Nano letters, 12(6) (2012) 2773-2777.

[14] X. Gan, K.F. Mak, Y. Gao, Y. You, F. Hatami, J. Hone, T.F. Heinz, D. Englund, Strong enhancement of light–matter interaction in graphene coupled to a photonic crystal nanocavity, Nano letters, 12(11) (2012) 5626-5631.

[15] A. Majumdar, J. Kim, J. Vuckovic, F. Wang, Electrical control of silicon photonic crystal cavity by graphene, Nano letters, 13(2) (2013) 515-518.

[16] X. Gan, Y. Gao, K. Fai Mak, X. Yao, R.-J. Shiue, A. van der Zande, M.E. Trusheim, F. Hatami, T.F. Heinz, J. Hone, Controlling the spontaneous emission rate of monolayer MoS2 in a photonic crystal nanocavity, Applied physics letters, 103(18) (2013) 181119.

[17] A. Sobhani, A. Lauchner, S. Najmaei, C. Ayala-Orozco, F. Wen, J. Lou, N.J. Halas, Enhancing the photocurrent and photoluminescence of single crystal monolayer MoS2 with resonant plasmonic nanoshells, Applied Physics Letters, 104(3) (2014) 031112.

[18] A.K. Geim, I.V. Grigorieva, Van der Waals heterostructures, Nature, 499(7459) (2013) 419-425.

[19] A.C. Ferrari, D.M. Basko, Raman spectroscopy as a versatile tool for studying the properties of graphene, Nature nanotechnology, 8(4) (2013) 235-246.

[20] C.H. Lui, K.F. Mak, J. Shan, T.F. Heinz, Ultrafast photoluminescence from graphene, Physical review letters, 105(12) (2010) 127404.

[21] F. Schwierz, Graphene transistors, Nature nanotechnology, 5(7) (2010) 487-496.

[22] A.K. Geim, K.S. Novoselov, The rise of graphene, Nat Mater, 6(3) (2007) 183-191.

[23] K.S. Novoselov, A.K. Geim, S.V. Morozov, D. Jiang, Y. Zhang, S.V. Dubonos, I.V. Grigorieva, A.A. Firsov, Electric Field Effect in Atomically Thin Carbon Films, Science, 306(5696) (2004) 666-669.

[24] T. Cao, G. Wang, W. Han, H. Ye, C. Zhu, J. Shi, Q. Niu, P. Tan, E. Wang, B. Liu, J. Feng, Valley-selective circular dichroism of monolayer molybdenum disulphide, Nat Commun, 3 (2012) 887.

[25] H.R. Gutiérrez, N. Perea-López, A.L. Elías, A. Berkdemir, B. Wang, R. Lv, F. López-Urías, V.H. Crespi, H. Terrones, M. Terrones, Extraordinary Room-Temperature Photoluminescence in Triangular WS2 Monolayers, Nano Letters, 13(8) (2012) 3447-3454.

[26] RadisavljevicB, RadenovicA, BrivioJ, GiacomettiV, KisA, Single-layer MoS2 transistors, Nat Nano, 6(3) (2011) 147-150.

[27] G. Constantinescu, A. Kuc, T. Heine, Stacking in Bulk and Bilayer Hexagonal Boron Nitride, Physical Review Letters, 111(3) (2013) 036104.

[28] J. Xue, J. Sanchez-Yamagishi, D. Bulmash, P. Jacquod, A. Deshpande, K. Watanabe, T. Taniguchi, P. Jarillo-Herrero, B.J. LeRoy, Scanning tunnelling microscopy and spectroscopy of ultra-flat graphene on hexagonal boron nitride, Nat Mater, 10(4) (2011) 282-285.

[29] K.F. Mak, K. He, J. Shan, T.F. Heinz, Control of valley polarization in monolayer MoS2 by optical helicity, Nat Nano, 7(8) (2012) 494-498.

[30] Z. Yin, H. Li, H. Li, L. Jiang, Y. Shi, Y. Sun, G. Lu, Q. Zhang, X. Chen, H. Zhang, Single-Layer MoS2 Phototransistors, ACS Nano, 6(1) (2011) 74-80.

[31] T.C. Berkelbach, M.S. Hybertsen, D.R. Reichman, Theory of neutral and charged excitons in monolayer transition metal dichalcogenides, Physical Review B, 88(4) (2013) 045318.

[32] K.F. Mak, K. He, C. Lee, G.H. Lee, J. Hone, T.F. Heinz, J. Shan, Tightly bound trions in monolayer MoS2, Nat Mater, 12(3) (2013) 207-211.

[33] A. Chernikov, T.C. Berkelbach, H.M. Hill, A. Rigosi, Y. Li, O.B. Aslan, D.R. Reichman, M.S. Hybertsen, T.F. Heinz, Exciton binding energy and nonhydrogenic Rydberg series in monolayer WS 2, Physical review letters, 113(7) (2014) 076802.

[34] M.M. Ugeda, A.J. Bradley, S.-F. Shi, H. Felipe, Y. Zhang, D.Y. Qiu, W. Ruan, S.-K. Mo, Z. Hussain, Z.-X. Shen, Giant bandgap renormalization and excitonic effects in a monolayer transition metal dichalcogenide semiconductor, Nature materials, (2014).

[35] L. Britnell, R. Ribeiro, A. Eckmann, R. Jalil, B. Belle, A. Mishchenko, Y.-J. Kim, R. Gorbachev, T. Georgiou, S. Morozov, Strong light-matter interactions in heterostructures of atomically thin films, Science, 340(6138) (2013) 1311-1314.

[36] J. Yang, Z. Wang, F. Wang, R. Xu, J. Tao, S. Zhang, Q. Qin, B. Luther-Davies, C. Jagadish, Z. Yu, Atomically Thin Optical Lenses and Gratings, arXiv preprint arXiv:1411.6200, (2014).

[37] M.-L. Tsai, S.-H. Su, J.-K. Chang, D.-S. Tsai, C.-H. Chen, C.-I. Wu, L.-J. Li, L.-J. Chen, J.-H. He, Monolayer MoS2 heterojunction solar cells, ACS nano, 8(8) (2014) 8317-8322.

[38] J.K. Ellis, M.J. Lucero, G.E. Scuseria, The indirect to direct band gap transition in multilayered MoS2 as predicted by screened hybrid density functional theory, Applied Physics Letters, 99(26) (2011) 261908.

[39] J. Pei, J. Yang, R. Xu, Y.H. Zeng, Y.W. Myint, S. Zhang, J.C. Zheng, Q. Qin, X. Wang, W. Jiang, Exciton and Trion Dynamics in Bilayer MoS2, Small, 11(48) (2015) 6384-6390.

[40] J. Yang, T. Lü, Y.W. Myint, J. Pei, D. Macdonald, J.-C. Zheng, Y. Lu, Robust excitons and trions in monolayer MoTe2, ACS nano, 9(6) (2015) 6603-6609.

[41] H. Liu, Y. Du, Y. Deng, D.Y. Peide, Semiconducting black phosphorus: synthesis, transport properties and electronic applications, Chemical Society Reviews, 44(9) (2015) 2732-2743.

[42] P. Bridgman, TWO NEW MODIFICATIONS OF PHOSPHORUS, Journal of the American Chemical Society, 36(7) (1914) 1344-1363.

[43] H. Krebs, H. Weitz, K. Worms, Über die struktur und eigenschaften der halbmetalle. Viii. Die katalytische darstellung des schwarzen phosphors, Zeitschrift für anorganische und allgemeine Chemie, 280(1-3) (1955) 119-133.

[44] A. Brown, S. Rundqvist, Refinement of the crystal structure of black phosphorus, Acta Crystallographica, 19(4) (1965) 684-685.

[45] Y. Maruyama, S. Suzuki, K. Kobayashi, S. Tanuma, Synthesis and some properties of black phosphorus single crystals, Physica B+ c, 105(1-3) (1981) 99-102.

[46] Y. Maruyama, T. Inabe, T. Nishii, L. He, A. Dann, I. Shirotani, M. Fahy, M. Willis, Electrical conductivity of black phosphorus-silicon compound, Synthetic Metals, 29(2-3) (1989) 213-218.

[47] Y. Maruyama, T. Inabe, L. He, K. Oshima, Electrical conductivity of black phosphorous-germanium compound, Synthetic Metals, 43(3) (1991) 4067-4070.

[48] I. Shirotani, Growth of large single crystals of black phosphorus at high pressures and temperatures, and its electrical properties, Molecular Crystals and Liquid Crystals, 86(1) (1982) 203-211.

[49] S. Lange, P. Schmidt, T. Nilges, Au3SnP7@ black phosphorus: an easy access to black phosphorus, Inorganic chemistry, 46(10) (2007) 4028-4035.

[50] T. Nilges, M. Kersting, T. Pfeifer, A fast low-pressure transport route to large black phosphorus single crystals, Journal of solid state chemistry, 181(8) (2008) 1707-1711.

[51] M. Köpf, N. Eckstein, D. Pfister, C. Grotz, I. Krüger, M. Greiwe, T. Hansen, H. Kohlmann, T. Nilges, Access and in situ growth of phosphorene-precursor black phosphorus, Journal of crystal growth, 405 (2014) 6-10.

[52] J. Lu, J. Yang, A. Carvalho, H. Liu, Y. Lu, C.H. Sow, Light–matter interactions in phosphorene, Accounts of chemical research, 49(9) (2016) 1806-1815.

[53] H. Liu, A.T. Neal, Z. Zhu, Z. Luo, X. Xu, D. Tománek, P.D. Ye, Phosphorene: An Unexplored 2D Semiconductor with a High Hole Mobility, ACS Nano, 8(4) (2014) 4033-4041.

[54] M. Zelisko, Y. Hanlumyuang, S. Yang, Y. Liu, C. Lei, J. Li, P.M. Ajayan, P. Sharma, Anomalous piezoelectricity in two-dimensional graphene nitride nanosheets, Nature communications, 5 (2014).

[55] M. Buscema, D.J. Groenendijk, S.I. Blanter, G.A. Steele, H.S.J. van der Zant, A. Castellanos-Gomez, Fast and Broadband Photoresponse of Few-Layer Black Phosphorus Field-Effect Transistors, Nano Letters, 14(6) (2014) 3347-3352.

[56] T. Hong, B. Chamlagain, W. Lin, H.-J. Chuang, M. Pan, z. zhou, Y. Xu, Polarized Photocurrent Response in Black Phosphorus Field-Effect Transistors, Nanoscale, (2014).

[57] R. Fei, L. Yang, Strain-Engineering the Anisotropic Electrical Conductance of Few-Layer Black Phosphorus, Nano Letters, 14(5) (2014) 2884-2889.

[58] J. Qiao, X. Kong, Z.-X. Hu, F. Yang, W. Ji, High-mobility transport anisotropy and linear dichroism in few-layer black phosphorus, Nat Commun, 5 (2014).

[59] F. Xia, H. Wang, Y. Jia, Rediscovering black phosphorus as an anisotropic layered material for optoelectronics and electronics, Nat Commun, 5 (2014).

[60] L. Li, Y. Yu, G.J. Ye, Q. Ge, X. Ou, H. Wu, D. Feng, X.H. Chen, Y. Zhang, Black phosphorus field-effect transistors, Nature nanotechnology, 9(5) (2014) 372-377.

[61] J. Pei, J. Yang, Y. Lu, Elastic and Inelastic Light–Matter Interactions in 2D Materials, IEEE Journal of Selected Topics in Quantum Electronics, 23(1) (2017) 206-213.

[62] J. Weiner, P.-T. Ho, Light-Matter Interaction, Volume 1: Fundamentals and Applications, John Wiley & Sons, 2008.

[63] R. Xu, J. Yang, Y.W. Myint, J. Pei, H. Yan, F. Wang, Y. Lu, Exciton brightening in monolayer phosphorene via dimensionality modification, Advanced Materials, 28(18) (2016) 3493-3498.

[64] R. Xu, J. Yang, Y. Zhu, H. Yan, J. Pei, Y.W. Myint, S. Zhang, Y. Lu, Layer-dependent surface potential of phosphorene and anisotropic/layer-dependent charge transfer in phosphorene–gold hybrid systems, Nanoscale, 8(1) (2016) 129-135.

[65] Y. Zhu, J. Yang, S. Zhang, S. Mokhtar, J. Pei, X. Wang, Y. Lu, Strongly enhanced photoluminescence in nanostructured monolayer MoS2 by chemical vapor deposition, Nanotechnology, 27(13) (2016) 135706.

[66] N. Engheta, R.W. Ziolkowski, Metamaterials: physics and engineering explorations, John Wiley & Sons, 2006.

[67] F. Bonaccorso, Z. Sun, T. Hasan, A. Ferrari, Graphene photonics and optoelectronics, Nature photonics, 4(9) (2010) 611.

[68] C.-C. Shen, Y.-T. Hsu, L.-J. Li, H.-L. Liu, Charge dynamics and electronic structures of monolayer MoS2 films grown by chemical vapor deposition, Applied Physics Express, 6(12) (2013) 125801.

[69] H.O. Churchill, P. Jarillo-Herrero, Two-dimensional crystals: Phosphorus joins the family, Nature nanotechnology, 9(5) (2014) 330.

[70] A. Carvalho, R. Ribeiro, A.C. Neto, Band nesting and the optical response of two-dimensional semiconducting transition metal dichalcogenides, Physical Review B, 88(11) (2013) 115205.

[71] L. Mattheiss, Band structures of transition-metal-dichalcogenide layer compounds, Physical Review B, 8(8) (1973) 3719.

[72] J.S. Ross, P. Klement, A.M. Jones, N.J. Ghimire, J. Yan, D. Mandrus, T. Taniguchi, K. Watanabe, K. Kitamura, W. Yao, Electrically tunable excitonic light-emitting diodes based on monolayer WSe 2 p–n junctions, Nature nanotechnology, 9(4) (2014) 268.

[73] A. Newaz, D. Prasai, J. Ziegler, D. Caudel, S. Robinson, R. Haglund Jr, K. Bolotin, Electrical control of optical properties of monolayer MoS 2, Solid State Communications, 155 (2013) 49-52.

[74] S. Tongay, J. Zhou, C. Ataca, K. Lo, T.S. Matthews, J. Li, J.C. Grossman, J. Wu, Thermally driven crossover from indirect toward direct bandgap in 2D semiconductors: MoSe2 versus MoS2, Nano letters, 12(11) (2012) 5576-5580.

[75] H. Qiu, T. Xu, Z. Wang, W. Ren, H. Nan, Z. Ni, Q. Chen, S. Yuan, F. Miao, F. Song, Hopping transport through defect-induced localized states in molybdenum disulphide, Nature communications, 4 (2013) 2642.

[76] W. Zhou, X. Zou, S. Najmaei, Z. Liu, Y. Shi, J. Kong, J. Lou, P.M. Ajayan, B.I. Yakobson, J.-C. Idrobo, Intrinsic structural defects in monolayer molybdenum disulfide, Nano letters, 13(6) (2013) 2615-2622.

[77] H. Nan, Z. Wang, W. Wang, Z. Liang, Y. Lu, Q. Chen, D. He, P. Tan, F. Miao, X. Wang, Strong photoluminescence enhancement of MoS2 through defect engineering and oxygen bonding, ACS nano, 8(6) (2014) 5738-5745.

[78] S. Tongay, J. Suh, C. Ataca, W. Fan, A. Luce, J.S. Kang, J. Liu, C. Ko, R. Raghunathanan, J. Zhou, Defects activated photoluminescence in two-dimensional semiconductors: interplay between bound, charged, and free excitons, Scientific reports, 3 (2013).

[79] D.K. Venkatachalam, P. Parkinson, S. Ruffell, R.G. Elliman, Rapid, substrate-independent thickness determination of large area graphene layers, Appl. Phys. Lett., 99(23) (2011) 234106.

[80] J. Yang, Z. Wang, F. Wang, R. Xu, J. Tao, S. Zhang, Q. Qin, B. Luther-Davies, C. Jagadish, Z. Yu, Atomically thin optical lenses and gratings, Light: Science & Applications, 5(3) (2016) e16046.

[81] J.Y. Lee, B.H. Hong, W.Y. Kim, S.K. Min, Y. Kim, M.V. Jouravlev, R. Bose, K.S. Kim, I.-C. Hwang, L.J. Kaufman, Near-field focusing and magnification through self-assembled nanoscale spherical lenses, Nature, 460(7254) (2009) 498.

[82] X. Zheng, B. Jia, H. Lin, L. Qiu, D. Li, M. Gu, Highly efficient and ultra-broadband graphene oxide ultrathin lenses with three-dimensional subwavelength focusing, Nature communications, 6 (2015) 8433.

[83] P. de Groot, Phase Shifting Interferometry, in: R. Leach (Ed.) Optical Measurement of Surface Topography, Springer Berlin Heidelberg, 2011, pp. 167-186.

[84] D. Abergel, A. Russell, V.I. Fal'ko, Visibility of graphene flakes on a dielectric substrate, Applied Physics Letters, 91(6) (2007) 063125.

[85] M. Benameur, B. Radisavljevic, J. Heron, S. Sahoo, H. Berger, A. Kis, Visibility of dichalcogenide nanolayers, Nanotechnology, 22(12) (2011) 125706.

[86] P. Blake, E. Hill, A. Castro Neto, K. Novoselov, D. Jiang, R. Yang, T. Booth, A. Geim, Making graphene visible, Applied Physics Letters, 91(6) (2007) 063124.

[87] A. Castellanos-Gomez, M. Buscema, R. Molenaar, V. Singh, L. Janssen, H.S.J.v.d. Zant, G.A. Steele, Deterministic transfer of two-dimensional materials by all-dry viscoelastic stamping, 2D Materials, 1(1) (2014) 011002.

[88] Q.-H. Qin, S.-W. Yu, An arbitrarily-oriented plane crack terminating at the interface between dissimilar piezoelectric materials, International Journal of Solids and Structures, 34(5) (1997) 581-590.

[89] Q.-H. Qin, Y.-W. Mai, A closed crack tip model for interface cracks inthermopiezoelectric materials, International Journal of Solids and Structures, 36(16) (1999) 2463-2479.

[90] S.W. Yu, Q.H. Qin, Damage analysis of thermopiezoelectric properties: Part I — crack tip singularities, Theoretical and Applied Fracture Mechanics, 25(3) (1996) 263-277.

[91] Q.-H. Qin, Y.-W. Mai, S.-W. Yu, Some problems in plane thermopiezoelectric materials with holes, International Journal of Solids and Structures, 36(3) (1999) 427-439.

[92] Q.-H. Qin, Y.W. Mai, S.-W. Yu, Effective moduli for thermopiezoelectric materials with microcracks, 91 (1998) 359-371.

[93] Q.H. Qin, H. Wang, Matlab and C programming for Trefftz finite element methods, in, New York: CRC Press, 2009.

[94] Q.H. Qin, Trefftz finite element method and its applications, Applied Mechanics Reviews, 58(5) (2005) 316-337.

[95] H. Wang, Q.-H. Qin, A meshless method for generalized linear or nonlinear Poisson-type problems, Engineering Analysis with Boundary Elements, 30(6) (2006) 515-521.

[96] H. Wang, Q.H. Qin, FE approach with Green's function as internal trial function for simulating bioheat transfer in the human eye, 2010.

[97] Q.H. Qin, Hybrid-Trefftz finite element method for Reissner plates on an elastic foundation, Computer Methods in Applied Mechanics and Engineering, 122(3) (1995) 379-392.

[98] Q.-S. Yang, Q.-H. Qin, Numerical simulation of cracking processes in dissimilar media, Composite Structures, 53(4) (2001) 403-407.

[99] M. Cardona, Y.Y. Peter, Fundamentals of semiconductors, Springer, 2005.

[100] C.V. Raman, A change of wave-length in light scattering, Nature, 121(3051) (1928) 619.

[101] P. Graves, D. Gardiner, Practical Raman Spectroscopy, in, Springer, 1989.

[102] S.M. Sze, Semiconductor devices: physics and technology, John Wiley & Sons, 2008.

[103] K. Kheng, R.T. Cox, M.Y. d' Aubigné, F. Bassani, K. Saminadayar, S. Tatarenko, Observation of negatively charged excitons in semiconductor quantum wells, Physical Review Letters, 71(11) (1993) 1752-1755.

[104] S. Sugai, I. Shirotani, Raman and infrared reflection spectroscopy in black phosphorus, Solid State Communications, 53(9) (1985) 753-755.

[105] R.S. Vy Tran, Yufeng Liang, Li Yang, Tunable Band Gap and Anisotropic Optical Response in Few-layer Black Phosphorus, arXiv:1402.4192, (2014).

[106] L.V. Andres Castellanos-Gomez, Elsa Prada, Joshua O. Island, K. L. Narasimha-Acharya, Sofya I. Blanter, Dirk J. Groenendijk, Michele Buscema, Gary A. Steele, J. V. Alvarez, Henny W. Zandbergen, J. J. Palacios, Herre S.J. van der Zant, Isolation and characterization of few-layer black phosphorus, arXiv:1403.0499, (2014).

[107] X. Yin, Z. Ye, D.A. Chenet, Y. Ye, K. O'Brien, J.C. Hone, X. Zhang, Edge Nonlinear Optics on a MoS2 Atomic Monolayer, Science, 344(6183) (2014) 488-490.

[108] I. Calizo, A.A. Balandin, W. Bao, F. Miao, C.N. Lau, Temperature Dependence of the Raman Spectra of Graphene and Graphene Multilayers, Nano Letters, 7(9) (2007) 2645-2649.

[109] S. Sahoo, A.P.S. Gaur, M. Ahmadi, M.J.F. Guinel, R.S. Katiyar, Temperature-Dependent Raman Studies and Thermal Conductivity of Few-Layer MoS2, The Journal of Physical Chemistry C, 117(17) (2013) 9042-9047.

[110] C. Postmus, J.R. Ferraro, S.S. Mitra, Pressure Dependence of Infrared Eigenfrequencies of KCl and KBr, Physical Review, 174(3) (1968) 983-987.

[111] X.P. Qun Wei, Superior mechanical flexibility of phosphorene and few-layer black phosphorus, arXiv:1403.7882, (2014).

[112] G. Kresse, J. Furthmüller, Efficient iterative schemes for ab-initio total-energy calculations using a plane-wave basis set, Physical Review B, 54(16) (1996) 11169-11186.

[113] G. Kresse, J. Furthmüller, Efficiency of ab-initio total energy calculations for metals and semiconductors using a plane-wave basis set, Computational Materials Science, 6(1) (1996) 15-50.

[114] J. Heyd, G.E. Scuseria, M. Ernzerhof, Erratum: "Hybrid functionals based on a screened Coulomb potential" [J. Chem. Phys.118, 8207 (2003)], The Journal of Chemical Physics, 124(21) (2006) -.

[115] W.P. Dumke, Spontaneous Radiative Recombination in Semiconductors, Physical Review, 105(1) (1957) 139-144.

[116] S. Mouri, Y. Miyauchi, K. Matsuda, Tunable Photoluminescence of Monolayer MoS2 via Chemical Doping, Nano Letters, 13(12) (2013) 5944-5948.

[117] E. Wigner, On the Interaction of Electrons in Metals, Physical Review, 46(11) (1934) 1002-1011.

[118] X. Xu, W. Yao, D. Xiao, T.F. Heinz, Spin and pseudospins in layered transition metal dichalcogenides, Nat Phys, 10(5) (2014) 343-350.

[119] G.D. Scholes, G. Rumbles, Excitons in nanoscale systems, Nat Mater, 5(9) (2006) 683-696.

[120] A.A. High, E.E. Novitskaya, L.V. Butov, M. Hanson, A.C. Gossard, Control of Exciton Fluxes in an Excitonic Integrated Circuit, Science, 321(5886) (2008) 229-231.

[121] S. Zhang, J. Yang, R. Xu, F. Wang, W. Li, M. Ghufran, Y.-W. Zhang, Z. Yu, G. Zhang, Q. Qin, Extraordinary photoluminescence and strong temperature/angle-dependent Raman responses in few-layer phosphorene, ACS nano, 8(9) (2014) 9590-9596.

[122] J. Yang, R. Xu, J. Pei, Y.W. Myint, F. Wang, Z. Wang, S. Zhang, Z. Yu, Y. Lu, Optical Tuning of Exciton and Trion Emissions in Monolayer Phosphorene, arXiv preprint arXiv:1504.06386, (2015).

[123] M. Buscema, G.A. Steele, H.S. van der Zant, A. Castellanos-Gomez, The effect of the substrate on the Raman and photoluminescence emission of single-layer MoS 2, Nano research, 7(4) (2014) 561-571.

[124] Z. Yin, H. Li, H. Li, L. Jiang, Y. Shi, Y. Sun, G. Lu, Q. Zhang, X. Chen, H. Zhang, Single-Layer MoS2 Phototransistors, ACS Nano, 6(1) (2012) 74-80.

[125] U. Bhanu, M.R. Islam, L. Tetard, S.I. Khondaker, Photoluminescence quenching in gold - MoS2 hybrid nanoflakes, Sci. Rep., 4 (2014).

[126] J. Shang, X. Shen, C. Cong, N. Peimyoo, B. Cao, M. Eginligil, T. Yu, Observation of Excitonic Fine Structure in a 2D Transition-Metal Dichalcogenide Semiconductor, ACS nano, 9(1) (2015) 647-655.

[127] Y. You, X.-X. Zhang, T.C. Berkelbach, M.S. Hybertsen, D.R. Reichman, T.F. Heinz, Observation of biexcitons in monolayer WSe2, Nature Physics, (2015).

[128] J.S. Park, Y. Hirana, S. Mouri, Y. Miyauchi, N. Nakashima, K. Matsuda, Observation of Negative and Positive Trions in the Electrochemically Carrier-Doped Single-Walled Carbon Nanotubes, Journal of the American Chemical Society, 134(35) (2012) 14461-14466.

[129] J.S. Ross, S. Wu, H. Yu, N.J. Ghimire, A.M. Jones, G. Aivazian, J. Yan, D.G. Mandrus, D. Xiao, W. Yao, X. Xu, Electrical control of neutral and charged excitons in a monolayer semiconductor, Nat Commun, 4 (2013) 1474.

[130] R. Matsunaga, K. Matsuda, Y. Kanemitsu, Observation of Charged Excitons in Hole-Doped Carbon Nanotubes Using Photoluminescence and Absorption Spectroscopy, Physical Review Letters, 106(3) (2011) 037404.

[131] H. Li, Q. Zhang, X. Duan, X. Wu, X. Fan, X. Zhu, X. Zhuang, W. Hu, H. Zhou, A. Pan, Lateral Growth of Composition Graded Atomic Layer MoS2 (1–x) Se2 x Nanosheets, Journal of the American Chemical Society, 137(16) (2015) 5284-5287.

[132] H. Li, X. Duan, X. Wu, X. Zhuang, H. Zhou, Q. Zhang, X. Zhu, W. Hu, P. Ren, P. Guo, Growth of Alloy MoS2 x Se2 (1–x) Nanosheets with Fully Tunable Chemical Compositions and Optical Properties, Journal of the American Chemical Society, 136(10) (2014) 3756-3759.

[133] Q. Feng, N. Mao, J. Wu, H. Xu, C. Wang, J. Zhang, L. Xie, Growth of MoS2 (1–x) Se2 x (x= 0.41–1.00) Monolayer Alloys with Controlled Morphology by Physical Vapor Deposition, ACS nano, 9(7) (2015) 7450-7455.

[134] L. Chen, B. Liu, A.N. Abbas, Y. Ma, X. Fang, Y. Liu, C. Zhou, Screw-Dislocation-Driven Growth of Two-Dimensional Few-Layer and Pyramid-like WSe2 by Sulfur-Assisted Chemical Vapor Deposition, ACS nano, 8(11) (2014) 11543-11551.

[135] J. Mann, Q. Ma, P.M. Odenthal, M. Isarraraz, D. Le, E. Preciado, D. Barroso, K. Yamaguchi, G. von Son Palacio, A. Nguyen, 2-Dimensional Transition Metal Dichalcogenides with Tunable Direct Band Gaps: MoS2 (1–x) Se2x Monolayers, Advanced Materials, 26(9) (2014) 1399-1404.

[136] Q. Feng, Y. Zhu, J. Hong, M. Zhang, W. Duan, N. Mao, J. Wu, H. Xu, F. Dong, F. Lin, Growth of Large-Area 2D MoS2 (1-x) Se2x Semiconductor Alloys, Advanced Materials, 26(17) (2014) 2648-2653.

[137] V. Huard, R.T. Cox, K. Saminadayar, A. Arnoult, S. Tatarenko, Bound States in Optical Absorption of Semiconductor Quantum Wells Containing a Two-Dimensional Electron Gas, Physical Review Letters, 84(1) (2000) 187-190.

[138] Z. Qin, Q.-H. Qin, X.-Q. Feng, Mechanical property of carbon nanotubes with intramolecular junctions: Molecular dynamics simulations, Physics Letters A, 372(44) (2008) 6661-6666.

[139] K. Cai, Y. Li, Q.H. Qin, H. Yin, Gradientless temperature-driven rotating motor from a double-walled carbon nanotube, Nanotechnology, 25(50) (2014) 505701.

[140] K. Cai, H. Yin, Q.H. Qin, Y. Li, Self-excited oscillation of rotating double-walled carbon nanotubes, Nano letters, 14(5) (2014) 2558-2562.

[141] W. Qiu, Y.L. Kang, Z.K. Lei, Q.H. Qin, Q. Li, Q. Wang, Experimental study of the Raman strain rosette based on the carbon nanotube strain sensor, Journal of Raman Spectroscopy, 41(10) (2010) 1216-1220.

[142] W. Qiu, Y.-L. Kang, Z.-K. Lei, Q.H. Qin, Q. Li, A new theoretical model of a carbon nanotube strain sensor, Chinese Physics Letters, 26(8) (2009) 080701.

[143] W. Qiu, Q. Li, Z.-K. Lei, Q.-H. Qin, W.-L. Deng, Y.-L. Kang, The use of a carbon nanotube sensor for measuring strain by micro-Raman spectroscopy, Carbon, 53 (2013) 161-168.

[144] V. Tran, R. Soklaski, Y. Liang, L. Yang, Layer-controlled band gap and anisotropic excitons in few-layer black phosphorus, Physical Review B, 89(23) (2014) 235319.

[145] H. Yuan, X. Liu, F. Afshinmanesh, W. Li, G. Xu, J. Sun, B. Lian, G. Ye, Y. Hikita, Z. Shen, S.-C. Zhang, X. Chen, M. Brongersma, H.Y. Hwang, Y. Cui, Broadband Linear-Dichroic Photodetector in a Black Phosphorus Vertical p-n Junction, arXiv:1409.4729, (2014).

[146] H. Yuan, X. Liu, F. Afshinmanesh, W. Li, G. Xu, J. Sun, B. Lian, A.G. Curto, G. Ye, Y. Hikita, Polarization-sensitive broadband photodetector using a black phosphorus vertical p–n junction, Nature nanotechnology, 10(8) (2015) 707.

[147] M. Buscema, D.J. Groenendijk, S.I. Blanter, G.A. Steele, H.S. van der Zant, A. Castellanos-Gomez, Fast and broadband photoresponse of few-layer black phosphorus field-effect transistors, Nano letters, 14(6) (2014) 3347-3352.

[148] D. Li, Y. Ye, X. Liao, Q.H. Qin, A novel method for preparing and characterizing graphene nanoplatelets/aluminum nanocomposites, Nano Research, 11(3) (2017) 1642-1650.

[149] C. Xu, T. Xue, J. Guo, Q.H. Qin, S. Wu, H. Song, H. Xie, An experimental investigation on the mechanical properties of the interface between large-sized graphene and a flexible substrate, Journal of Applied Physics, 117(16) (2015) 164301.

[150] V.I. Klimov, A.A. Mikhailovsky, S. Xu, A. Malko, J.A. Hollingsworth, C.A. Leatherdale, H.-J. Eisler, M.G. Bawendi, Optical Gain and Stimulated Emission in Nanocrystal Quantum Dots, Science, 290(5490) (2000) 314-317.

[151] C. Galland, A. Imamoğlu, All-Optical Manipulation of Electron Spins in Carbon-Nanotube Quantum Dots, Physical Review Letters, 101(15) (2008) 157404.

[152] S.G. Carter, V. Birkedal, C.S. Wang, L.A. Coldren, A.V. Maslov, D.S. Citrin, M.S. Sherwin, Quantum Coherence in an Optical Modulator, Science, 310(5748) (2005) 651-653.

[153] D.M. Ceperley, B. Alder, Ground state of the electron gas by a stochastic method, Physical Review Letters, 45(7) (1980) 566.

[154] R. Needs, M. Towler, N. Drummond, P.L. Ríos, Continuum variational and diffusion quantum Monte Carlo calculations, Journal of Physics: Condensed Matter, 22(2) (2009) 023201.

[155] B. Ganchev, N. Drummond, I. Aleiner, V. Fal'ko, Three-particle complexes in two-dimensional semiconductors, Physical review letters, 114(10) (2015) 107401.

[156] A. Thilagam, Exciton complexes in low dimensional transition metal dichalcogenides, Journal of Applied Physics, 116(5) (2014) 053523.

[157] W. Ruan, K. Chan, H. Ho, R. Zhang, E. Pun, Hyperspherical approach for charged excitons in quantum wells, Physical Review B, 60(8) (1999) 5714.

[158] Z. Ye, T. Cao, K. O'Brien, H. Zhu, X. Yin, Y. Wang, S.G. Louie, X. Zhang, Probing excitonic dark states in single-layer tungsten disulphide, Nature, 513(7517) (2014) 214-218.

[159] J. Yang, R. Xu, J. Pei, Y.W. Myint, F. Wang, Z. Wang, S. Zhang, Z. Yu, Y. Lu, Unambiguous identification of monolayer phosphorene by phase-shifting interferometry, arXiv preprint arXiv:1412.6701, (2014).

[160] T.F. Rønnow, T.G. Pedersen, B. Partoens, K.K. Berthelsen, Variational quantum Monte Carlo study of charged excitons in fractional dimensional space, Physical Review B, 84(3) (2011) 035316.

[161] Y. Cai, G. Zhang, Y.-W. Zhang, Layer-dependent band alignment and work function of few-layer phosphorene, Scientific reports, 4 (2014).

[162] J. Yang, R. Xu, J. Pei, Y.W. Myint, F. Wang, Z. Wang, S. Zhang, Z. Yu, Y. Lu, Optical tuning of exciton and trion emissions in monolayer phosphorene, Light Sci Appl, 4 (2015) e312.

[163] S. Zhang, R. Xu, F. Wang, J. Yang, Z. Wang, J. Pei, Y.W. Myint, B. Xing, Z. Yu, L. Fu, Extraordinarily bound quasi-one-dimensional trions in two-dimensional phosphorene atomic semiconductors, arXiv preprint arXiv:1411.6124, (2014).

[164] H. Schreiber, J.H. Bruning, Phase Shifting Interferometry, in: Optical Shop Testing, John Wiley & Sons, Inc., 2006, pp. 547-666.

[165] T. Nagahama, M. Kobayashi, Y. Akahama, S. Endo, S.-i. Narita, Optical Determination of Dielectric Constant in Black Phosphorus, J. Phys. Soc. Jpn., 54(6) (1985) 2096-2099.

[166] J. Shi, H. Cai, K. Cai, Q.-H. Qin, Dynamic behavior of a black phosphorus and carbon nanotube composite system, Journal of Physics D: Applied Physics, 50(2) (2016) 025304.

[167] K. Cai, L. Liu, J. Shi, Q.H. Qin, Self-assembly of a jammed black phosphorus nanoribbon on a fixed carbon nanotube, The Journal of Physical Chemistry C, 121(18) (2017) 10174-10181.

[168] J.S. Bunch, A.M. van der Zande, S.S. Verbridge, I.W. Frank, D.M. Tanenbaum, J.M. Parpia, H.G. Craighead, P.L. McEuen, Electromechanical Resonators from Graphene Sheets, Science, 315(5811) (2007) 490-493.

[169] S.P. Koenig, R.A. Doganov, H. Schmidt, A. Castro Neto, B. Özyilmaz, Electric field effect in ultrathin black phosphorus, Applied Physics Letters, 104(10) (2014) 103106.

[170] J.D. Wood, S.A. Wells, D. Jariwala, K.-S. Chen, E. Cho, V.K. Sangwan, X. Liu, L.J. Lauhon, T.J. Marks, M.C. Hersam, Effective passivation of exfoliated black phosphorus transistors against ambient degradation, Nano letters, 14(12) (2014) 6964-6970.

[171] A. Favron, E. Gaufrès, F. Fossard, P. Lévesque, A. Phaneuf-L'Heureux, N. Tang, A. Loiseau, R. Leonelli, S. Francoeur, R. Martel, Exfoliating pristine black phosphorus down to the monolayer: photo-oxidation and electronic confinement effects, arXiv preprint arXiv:1408.0345, (2014).

List of publications

- **Shuang Zhang***, Jiong Yang*, Renjing Xu, Fan Wang, Weifeng Li, Muhammad Ghufran, Yong-Wei Zhang, Zongfu Yu, Gang Zhang, Qinghua Qin, and Yuerui Lu "Extraordinary photoluminescence and strong temperature/angle-dependent Raman responses in few-layer phosphorene."***ACS nano*** 8.9 (2014): 9590-9596. Cited by 345 (Journal Paper)
- **Shuang Zhang*,** Renjing Xu*, Fan Wang, Jiong Yang, Zhu Wang, Jiajie Pei, Ye Win Myint et al. "Extraordinarily bound quasi-one-dimensional trions in two-dimensional phosphorene atomic semiconductors." ACS nano 10, no. 2 (2016): 2046-2053. Cited by 36 (Journal Paper)
- **Shuang Zhang**, Xinghua Wang, Jiong Yang, Jiajie Pei, Renjing Xu, Qinghua Qin and Yuerui Lu. "Robust Excitons and Trions in Monolayer MoS2xSe2(1-x) (x=0.45)". To be sumitted (Journal Paper)
- **Shuang Zhang**, Jin Tao, Jiong Yang, Juntao Sun, Qinaghua Qin and Yuerui Lu. "Few-layer phosphorene based micro-lens". To be submitted (Journal Paper)

<u>Publications not as first author:</u>

- Yi Zhu, Jiong Yang, **Shuang Zhang**, Salman Mokhtar, Jiajie Pei, Xinghua Wang, and Yuerui Lu. "Strongly enhanced photoluminescence in nanostructured monolayer MoS2 by chemical vapor deposition." Nanotechnology 27, no. 13 (2016): 135706.
- Renjing Xu, Jiong Yang, **Shuang Zhang**, Jiajie Pei, and Yuerui Lu. "2D materials for nanophotonic devices." In *Micro+ Nano Materials, Devices, and Systems*, vol. 9668, p. 966834. International Society for Optics and Photonics, 2015.

- Yang, Jiong, Zhu Wang, Fan Wang, Renjing Xu, Jin Tao, **Shuang Zhang**, Qinghua Qin et al. "Atomically thin optical lenses and gratings." Light: Science & Applications 5, no. 3 (2016): e16046.
- Qiran Cai, Aijun Du, Guoping Gao, Srikanth Mateti, Bruce CC Cowie, Dong Qian, **Shuang Zhang** et al. "Molecule‐Induced Conformational Change in Boron Nitride Nanosheets with Enhanced Surface Adsorption." Advanced Functional Materials 26, no. 45 (2016): 8202-8210.
- Xu, Renjing, Jiong Yang, Yi Zhu, Han Yan, Jiajie Pei, Ye Win Myint, **Shuang Zhang**, and Yuerui Lu. "Layer-dependent surface potential of phosphorene and anisotropic/layer-dependent charge transfer in phosphorene–gold hybrid systems." Nanoscale 8, no. 1 (2016): 129-135.
- Jiajie Pei, Jiong Yang, Renjing Xu, Yong‐Hui Zeng, Ye Win Myint, **Shuang Zhang**, Jin‐Cheng Zheng et al. "Exciton and trion dynamics in bilayer MoS2." small 11, no. 48 (2015): 6384-6390.
- Jiong Yang, Renjing Xu, Jiajie Pei, Ye Win Myint, Fan Wang, Zhu Wang, **Shuang Zhang**, Zongfu Yu, and Yuerui Lu. "Optical tuning of exciton and trion emissions in monolayer phosphorene." Light: Science & Applications 4, no. 7 (2015): e312.
- Jiong Yang, Renjing Xu, Jiajie Pei, Ye Win Myint, Fan Wang, Zhu Wang, **Shuang Zhang**, Zongfu Yu, and Yuerui Lu. "Unambiguous identification of monolayer phosphorene by phase-shifting interferometry." *arXiv preprint arXiv:1412.6701*(2014).
- Si, Kae Jye, Debabrata Sikdar, Yi Chen, Fatima Eftekhari, Zaiquan Xu, Yue Tang, Wei Xiong, Pengzhen Guo, **Shuang Zhang**, Yuerui Lu, Qiaoliang Bao, Weiren Zhu, Malin Premaratne, and Wenlong Chenget al. "Giant plasmene nanosheets, nanoribbons, and origami." ACS nano 8, no. 11 (2014): 11086-11093.